Karl-Franzens-Universität Graz

Institut für Physik

The size of the W-boson

Sebastian Raubitzek

Masterarbeit

zur Erlangung des akademischen Grades

Master of Science

an der Naturwissenschaftlichen Fakultät

Betreut von

Univ.-Prof. Dipl.-Phys. Dr.rer.nat. Axel Maas

October 2018

Abstract

In gauge theories gauge-variant states are non-physical observable states, because of this, different approaches than perturbation theory have to be considered.

We look at gauge-invariant composite operators and calculate n-point functions using lattice methods for a SU(2) gauge theory with a fundamental scalar. The considered operator consists of a W-boson-field dressed by two Higgs-boson-fields to obtain a gauge-invariant vector operator. The results of the two- and three-point functions are compared to results from a gauge-fixed setup in order to check the validity of the Fröhlich-Morchio-Strocchi-mechanism. The three-point function can then be used to calculate the ***radius*** of the W-boson.

The results show that there is a significant difference in the radius obtained from the three-point function of gauge-fixed elementary fields to the radius obtained from gauge-invariant composite operators. The radius of the gauge-invariant composite operator is positive and the radius for the gauge-fixed elementary fields is negative and smaller. This shows that despite of a very similar mass spectrum of the two approaches, there is a difference in the radius.

Kurzfassung

In Eichtheorien sind eichabhängige Zustände keine physikalisch beobachtbaren Zustände. Aus diesem Grund muss man andere Heransgehensweisen als Störungstheorie wählen, um physikalisch beobachtbare Zustände zu berechnen.

Wir betrachten eichinvariante, aus mehreren Felder zusammengesetzte Operatoren und berechnen die zugehörigen Zwei- und Drei-Punktfunktionen mit Gittermethoden. Der betrachtete Operator besteht dabei aus einem W-Boson-Feld, gebunden mit zwei Higgs-Boson-Feldern, um einen eichinvarianten Vektoroperator zu erhalten. Die Ergebnisse des erwähnten gebundenen Operators werden dabei mit Ergebnissen von eichfixierten Elementarfeldern verglichen, um die Vorhersagen des Fröhlich-Morchio-Strocchi Mechanismus zu bestätigen.

Die zugehörige Drei-Punktfunktion kann dann verwendet werden, um einen Radius für das W-Boson zu berechnen. Die Ergebnisse zeigen, dass es bei den beiden genannten Zugängen, den Radius betreffend, signifikante Unterschiede gibt. Der Radius des eichinvarianten Operators is dabei größer als der der eichfixierten Elementarfelder. Zusätzlich ist der Radius der Elementarfelder noch negativ und daher unphysikalisch. Dies zeigt, dass trotzdem, dass beide Ansätze das selbe Massenspektrum liefern, sie sich in anderen Größen deutlich unterscheiden können.

Acknowledgements

My special thanks go to Pascal Törek for supporting this project, proofreading this thesis and helping me with many problems that occurred while working on this project.

I would also like to thank Axel Maas for being very patient and supportive throughout the whole process of this work.

Contents

Chapter 1

Introduction

The Standard Model of particle physics is todays must sucesseful theory of elementary particles and its validity has been verified in various experiments [1]. The weak gauge bosons W and Z are part of the Standard Model and are important building blocks of the electroweak sector of this model. The determination of the decay width and mass of those particles is of great importance in testing the internal consistency of the Standard Model. In contrast to QCD and QED, the gauge bosons of the weak interaction are massive. Their mass is about 86 times the mass of a hydrogen atom, i.e. approximately 80.4 GeV [2]. The masses of these bosons originate from the Higgs-mechanism. Due to their huge masses, the weak interaction is, as the name suggests, weak, in contrast to e.g. QCD. Therefore, standard perturbation theory works very well for this sector of the Standard Model, and the comparison to experiments is remarkable [3]. The drawback of this approach is, that, e.g., the computated masses are gauge-dependent, since gauge-variant elementary fields enter the computations. Thus, such quantities are in principle not physical. Then one immediately asks the question, why do those calculations work despite of this inconsistency? An explanation is given by the mechanism described by Fröhlich, Morchio, and Strocchi [4, 5]. The basic idea followed in this thesis is to consider the W-boson not as an elementary field but as an composite state. This composite state is gauge-invariant and thus a phyiscal observable. In experiments the W-boson is observed as a vector triplet, so we may construct a vector triplet gauge-invariant composite operator.

As we see in Chapter 2, under certain conditions, met by the Standard Model, the properties of these physical states can be mapped to the gauge-dependent states which appear in the Lagrangian [6].

The calculations presented in this thesis give an estimate on how results for a gauge-invariant composite operator differ from results of perturbation theory, i.e., gauge-fixed elementary fields.

The aim of this work is to calculate two- and three-point functions for a gauge-invariant composite operator and compare these results to the standard approach using gauge-fixed elementary fields. It is known that the mass spectrum for both approaches is the same [7]. Since in the standard perturbative approach the elementary fields are treated as point-like particles, we expect differences in the radii of these objects and the ones computed from gauge-invariant composite and thus extended states.

The thesis is organized in the following way: Chapter 2 recaptures the foundations of quantum field theory, outlines the used notions and discusses the examined theory. In Chapter 3 form factors are discussed in detail and how to compute the radii of particles from these objects. Chapter 4 summarizes the used lattice technology. In Chapter 5 the results are presented and in Chapter 6 we discuss the results, giving a short summary and an outlook.

Chapter 2

Quantum field theory

In this chapter the basic aspects of quantum field theory, which are necessary for the calculations presented in the next chapters, are discussed. We follow closely [6–8].

2.1 Theory of the weak interaction

The theory of the weak interaction is a non-Abelian gauge theory with a fundamental scalar, or also called a fundamental Higgs. The theory has a local SU(2) gauge symmetry of and a global SU(2) custodial symmetry acting only on the Higgs-field. For simplicity we neglect fermions as well as the local U(1) hypercharge symmetry as considered in the full electroweak sector of the standard model. The Lagrangian density consists of the complex scalar ϕ coupled to a non-Abelian gauge-field W:

$$\mathcal{L} \,=\, -\frac{1}{4} W^a_{\mu\nu} W^{\mu\nu}_a \,+\, (D_\mu \phi)^\dagger \, (D^\mu \phi) \,-\, V\left(\phi^\dagger \phi\right) \tag{2.1}$$

$$W^a_{\mu\nu} \,=\, \partial_\mu W^a_\nu - \partial_\nu W^a_\mu - g\epsilon^{abc} W^b_\mu W^a_\nu \qquad D_\mu \,=\, \partial_\mu - igW^a_\mu \tau^a$$

Here τ^a are the generators of the gauge group, g is the gauge coupling and ϵ^{abc} is the structure constant of the Lie-algebra of SU(2). The generators τ^a are related to the Pauli-matrices σ^a by $\tau^a = \frac{\sigma^a}{2}$. The fields of the Lagrangian transform under gauge transformations $G(x) \in \mathrm{SU}(2)$ as

$$\phi(x) \,\to\, G(x)\phi(x) \quad , \quad W_\mu(x) \,\to\, G(x) W_\mu(x) G(x)^\dagger + \frac{i}{g} \left(\partial_\mu G(x)\right) G(x)^\dagger \quad , \tag{2.2}$$

where $W_\mu(x) = W^a_\mu(x)\tau^a$.

The potential of the Lagrangian $V\left(\phi^\dagger\phi\right)$ is a function of $\phi^\dagger\phi$ and therefore is gauge-invariant. We consider a potential of the form

$$V\left(\phi^\dagger\phi\right) = \lambda\left(\phi^\dagger\phi - f^2\right)^2 \quad . \tag{2.3}$$

Thus the full Lagrangian is gauge invariant. The gauge-invariant condition for the potential to be minimal is $\phi^\dagger\phi = f^2$. These minima are invariant under custodial and gauge transformations. The potential (2.3) cannot break gauge-invariance nor custodial invariance, but the minima can make custodial invariance metastable against external perturbations [7].

2.1.1 The custodial symmetry

The complex doublet ϕ contains four real degrees of freedom and the custodial symmetry acts as a SU(2) flavor symmetry. This global symmetry can be made explicit using a matrix-representation of the scalar field, i.e.

$$X(x) = \begin{pmatrix} \phi_1(x) & -\phi_2(x)^* \\ \phi_2(x) & \phi_1(x)^* \end{pmatrix} \quad , \tag{2.4}$$

where $\phi_1(x)$ and $\phi_2(x)$ are the components of the complex doublet $\phi(x)$. This matrix is later used for the construction of composite operators and is refered to as Higgs-matrix. Gauge transformations act on this matrix as a left multiplication and flavor transformations act as a right multiplication. The custodial symmetry is from now on referred to as $\mathrm{SU(2)_c}$ to differ between the local gauge symmetry and the global custodial symmetry. The symmetry transformation for the custodial symmetry is

$$X(x) \to G(x)X(x)M^\dagger \quad , \tag{2.5}$$

where $M \in \mathrm{SU(2)_c}$ and $G(x) \in \mathrm{SU(2)}$. Note that $W_\mu(x)$ does not transform under custodial transformations.

Using $X(x)$ instead of $\phi(x)$ the Lagrangian (2.1) reads

$$\mathcal{L} = -\frac{1}{4}W^a_{\mu\nu}(x)W^{\mu\nu}_a(x) + \frac{1}{2}\mathrm{tr}\left[\left(D_\mu X(x)\right)^\dagger D^\mu X(x)\right] - \lambda\left[\frac{1}{2}\mathrm{tr}\left(X(x)X(x)^\dagger\right) + f^2\right]^2 \quad . \tag{2.6}$$

2.2 Gauge invariance and perturbation theory

All physical observables have to be gauge-invariant. The reason is that given a Lagrangian invariant under local symmetry transformations, e.g., SU(2) all expectation values with an open gauge index vanish, since the minimization of the potential fixes only the length $(\phi^\dagger\phi)$, which is gauge-invariant. An average over all possible directions in the path integral thus yields a zero expectation value. This is discussed in detail in [7]. In standard perturbation theory gauge-fixing is required to obtain a non-vanishing expectation value for gauge-dependent observables. Here we consider a gauge-invariant composite operator, thus no gauge fixing is required.

2.3 Composite Operators

In a non-Abelian theory physical observables are gauge-invariant composite operators consisting of more than one elementary field, such that the resulting operator is gauge-invariant. In terms of the theory discussed above these composite operators can be viewed as bound states of the Higgs- and the W-bosons. Composite operators are labelled by J^P_f quantum numbers, where J is the total angular momentum, P the parity and f indicates the flavor structure, being either a singlet or a triplet with respect to $\mathrm{SU}(2)_\mathrm{c}$. Here we discuss the 1^-_3 channel since we further use this channel for the computation of the radius of the physical W-boson.

The reason for choosing a vector triplet operator is that only the vector triplet state is observed in experiments. The simplest possible vector triplet operator is given as

$$O^{\bar{a}}_{1^-_3\,\mu}(x) \;=\; \mathrm{tr}\left[\tau^{\bar{a}}\frac{X(x)^\dagger}{\sqrt{\det\left(X(x)\right)}}D_\mu(x)\frac{X(x)}{\sqrt{\det\left(X(x)\right)}}\right] \quad , \tag{2.7}$$

where $\tau^{\bar{a}}$ are the generators of the global $\mathrm{SU}(2)_\mathrm{c}$ symmetry and $\bar{a} = 1, 2, 3$, labels the index of the custodial symmetry group.

2.4 Gauge-invariant perturbation theory

2.4.1 Gauge-invariant perturbation theory for the 1^-_3-channel operator

The basic idea of gauge-invariant perturbation theory is to use gauge-invariant composite operators and expand them in Higgs-fluctuations as described by Fröhlich, et al.[4, 5]. This procedure shows why perturbation theory works well in the standard model and, if

we calculate a full gauge-invariant quantity, there have to be some corrections compared to the gauge-dependent treatment.

Now the 1_3^- channel operator (2.7) is expanded in gauge-invariant perturbation theory. First, we consider the correlator (two-point function) and second the three-W-vertex (three-point function). Using $X(x) = v\alpha + \chi(x)$ with $\alpha \in \mathrm{SU}(2)_\mathrm{c}$ and the fluctuation field $\chi(x)$, the correlator in leading order gauge-invariant perturbation theory is

$$\left\langle O^{\bar{a}}_{\mu\, 1_3^-}(x)\, O^{\bar{b}\,\dagger}_{1_3^-\, \nu}(y) \right\rangle = g^2 c^{\bar{a}a} c^{\bar{b}b} \left\langle W^{\bar{a}}_\mu(x)\, W^{\bar{b}}_\nu(y) \right\rangle + \mathcal{O}(\chi) \quad , \tag{2.8}$$

and the vertex is

$$\left\langle O^{\bar{a}}_{\mu\, 1_3^-}(x)\, O^{\bar{b}}_{\nu\, 1_3^-}(y)\, O^{\bar{c}}_{\rho\, 1_3^-}(z) \right\rangle = -ig^3 c^{\bar{a}a} c^{\bar{b}b} c^{\bar{c}c} \left\langle W^{\bar{a}}_\mu(x)\, W^{\bar{b}}_\nu(y)\, W^{\bar{c}}_\rho(z) \right\rangle + \mathcal{O}(\chi) \quad , \tag{2.9}$$

where $c^{\bar{a}a} \in \mathbb{R}$. The full calculation for the correlator and the vertex can be found in Appendix A. E.g. (2.8) and (2.9) show why the standard perturbative approach works in case of the standard model: Using a gauge-invariant operator, the behaviour in leading order in the correlator and the vertex are exactly the corresponding expectation values of the elementary W-fields.

However the remaining question is:
How big is the difference between the full gauge-invariant treatment and the standard perturbative approach?

An answer to this question is given in Chapter 5.

2.5 The propagator and the vertex in momentum space

Here, everything is discussed in the continuum. In Chapter 4 the theory is discussed on the lattice. The discussion follows closely [9].

2.5.1 Momentum space

In this section all the operators are momentum space operators and are obtained from operators in spacetime as

$$O(p) = \frac{1}{\sqrt{(2\pi)^4}} \int d^4p\, e^{-ipx} O(x) \quad , \tag{2.10}$$

where $O(p)$ is an arbitrary momentum space operator and $O(x)$ is the corresponding position space operator.

2.5.2 Projectors and the propagator

The propagagator in momentum space is given by

$$D^{\bar{a}\bar{b}}_{\mu\nu}(p) \;=\; \left\langle O^{\bar{a}}_{\mu\,1^-_3}(p) O^{\bar{b}}_{\nu\,1^-_3}(p)^\dagger \right\rangle \quad . \tag{2.11}$$

The transverse and longitudinal projectors are

$$T_{\mu\nu}(p) \;=\; \delta_{\mu\nu} - \frac{p_\mu p_\nu}{p^2} \quad , \quad L_{\mu\nu}(p) \;=\; \frac{p_\mu p_\nu}{p^2} \quad . \tag{2.12}$$

Now, we can use them to obtain the transverse and longitudinal parts of the operator:

$$O^{\bar{a}}_{\nu\,\mathrm{T}}(p) \;=\; T_{\mu\nu}(p)\, O^{\bar{a}}_{\mu\,1^-_3}(p) \quad , \quad O^{\bar{a}}_{\nu\,\mathrm{L}}(p) \;=\; L_{\mu\nu}(p)\, O^{\bar{a}}_{\mu\,1^-_3}(p) \quad . \tag{2.13}$$

The transverse and longitudinal propagators are given by

$$D^{\bar{a}\bar{b}}_{\mathrm{T}}(p) \;=\; T_{\mu\nu}(p)\, D^{\bar{a}\bar{b}}_{\mu\nu}(p) \quad , \quad D^{\bar{a}\bar{b}}_{\mathrm{L}}(p) \;=\; L_{\mu\nu}(p)\, D^{\bar{a}\bar{b}}_{\mu\nu}(p) \quad . \tag{2.14}$$

Combinig both yields

$$D^{\bar{a}\bar{b}}_{\mu\nu}(p) \;=\; T_{\mu\nu}(p)\, D^{\bar{a}\bar{b}}_{\mathrm{T}}(p) \;+\; L_{\mu\nu}(p)\, D^{\bar{a}\bar{b}}_{\mathrm{L}}(p) \quad . \tag{2.15}$$

2.5.3 The vertex

We use the tensor object

$$\Gamma^{\bar{a}\bar{b}\bar{c}}_{\mu\nu\rho}(p,q,k) \;=\; -ig\epsilon^{\bar{a}\bar{b}\bar{c}} \left[(q-k)_\mu\, \delta_{\nu\rho} + (k-p)_\nu\, \delta_{\rho\mu} + (p-q)_\rho\, \delta_{\mu\nu} \right] \quad , \tag{2.16}$$

to contract all indices of the Lorentz structure of e.g. 2.8. A detailed discussion concerning the tensor objects is given in Chapter 3. The different contracted vertices we want to compute are

$$C_3(p,q,k) \;=\; \left\langle \Gamma^{\bar{a}\bar{b}\bar{c}}_{\mu\nu\rho}(p,q,k)\, O^{\bar{a}}_{\mu\,1^-_3}(p)\, O^{\bar{b}}_{\nu\,1^-_3}(q)\, O^{\bar{c}}_{\rho\,1^-_3}(k) \right\rangle \quad , \tag{2.17}$$

$$C_{3T}(p,q,k) \;=\; \left\langle \Gamma^{\bar{a}\bar{b}\bar{c}}_{\mu\nu\rho}(p,q,k)\, O^{\bar{a}}_{\mu\,\mathrm{T}}(p)\, O^{\bar{b}}_{\nu\,\mathrm{T}}(q)\, O^{\bar{c}}_{\rho\,\mathrm{T}}(k) \right\rangle \quad , \tag{2.18}$$

$$C_{3Z}(p,-p,0) \;=\; \left\langle \Gamma^{\bar{a}\bar{b}\bar{c}}_{\mu\nu\rho}(p,-p,0)\, O^{\bar{a}}_{\mu\, 1^-_3}(p)\, O^{\bar{b}}_{\nu\, 1^-_3}(-p)\, O^{\bar{c}}_{\rho\, 1^-_3}(0) \right\rangle \quad . \tag{2.19}$$

Note that momentum conservation requires $p+q+k=0$ in (2.17) and (2.18). Amputating (3.8) these vertices yield three different ratios

$$R(p,q,k) \;=\; \frac{\Gamma^{\bar{a}\bar{b}\bar{c}}_{\mu\nu\rho}(p,q,k)\, \left\langle O^{\bar{a}}_{\mu\, 1^-_3}(p)\, O^{\bar{b}}_{\nu\, 1^-_3}(q)\, O^{\bar{c}}_{\rho\, 1^-_3}(k) \right\rangle}{\Gamma^{\bar{a}\bar{b}\bar{c}}_{\mu\nu\rho}(p,q,k)\, D^{\bar{a}\bar{d}}_{\mu\gamma}(p)\, D^{\bar{b}\bar{e}}_{\nu\eta}(q)\, D^{\bar{c}\bar{f}}_{\rho\zeta}(k)\, \Gamma^{\bar{d}\bar{e}\bar{f}}_{\gamma\eta\zeta}(p,q,k)} \quad , \tag{2.20}$$

$$R_T(p,q,k) \;=\; \frac{\Gamma^{\bar{a}\bar{b}\bar{c}}_{\mu\nu\rho}(p,q,k)\, \left\langle O^{\bar{a}}_{\mu\,\mathrm{T}}(p)\, O^{\bar{b}}_{\nu\,\mathrm{T}}(q)\, O^{\bar{c}}_{\rho\,\mathrm{T}}(k) \right\rangle}{\Gamma^{\bar{a}\bar{b}\bar{c}}_{\mu\nu\rho}(p,q,k)\, T_{\mu\gamma}(p)\, D^{\bar{a}\bar{d}}_{\mathrm{T}}(p)\, T_{\nu\eta}(q)\, D^{\bar{b}\bar{e}}_{\mathrm{T}}(q)\, T_{\rho\zeta}(k)\, D^{\bar{c}\bar{f}}_{\mathrm{T}}(k)\, \Gamma^{\bar{d}\bar{e}\bar{f}}_{\gamma\eta\zeta}(p,q,k)} \quad , \tag{2.21}$$

$$R_Z(p,q,k) \;=\; \frac{\Gamma^{\bar{a}\bar{b}\bar{c}}_{\mu\nu\rho}(p,-p,0)\, \left\langle O^{\bar{a}}_{\mu\, 1^-_3}(p)\, O^{\bar{b}}_{\nu\, 1^-_3}(-p)\, O^{\bar{c}}_{\rho\, 1^-_3}(0) \right\rangle}{\Gamma^{\bar{a}\bar{b}\bar{c}}_{\mu\nu\rho}(p,q,k)\, D^{\bar{a}\bar{d}}_{\mu\gamma}(p)\, D^{\bar{b}\bar{e}}_{\nu\eta}(q)\, D^{\bar{c}\bar{f}}_{\rho\zeta}(k)\, \Gamma^{\bar{d}\bar{e}\bar{f}}_{\gamma\eta\zeta}(p,q,k)} \quad . \tag{2.22}$$

It is necessary to amputate the contracted vertices, these are equal the connected Green's functions due to the non-vanishing vector condensates in Yang-Mills theory [9] .

Chapter 3

Form factors and dressing functions

3.1 Form factors

In this section ideas of nucleon-scattering from [10] are used and identified with elements from the tensor structure of the three-W-vertex.
The scattering of electrons on a nucleus to obtain it's inner structure can be viewed as a three-point interaction. That is exactly the main idea employed here to obtain the radius of the physical W-state.

3.2 Tensor structure of the vertex

The starting point is to investigate the Lorentz tensor structure of the three-W-vertex $G_{\mu\nu\rho}(p,q,k)$. For the tensor structure of the vertex we follow [9, 11]. The three-W-vertex can be decomposed into 14 Lorentz-tensor structures with Lorentz-invariant dressing functions F_i, i.e.,

$$G^{\bar{a}\bar{b}\bar{c}}_{\mu\nu\rho}(p,q,k) \;=\; -ig\, D^{\bar{a}\bar{d}}_{\mu\gamma}(p)\, D^{\bar{b}\bar{e}}_{\nu\eta}(q)\, D^{\bar{c}\bar{f}}_{\rho\zeta}(k)\, \epsilon^{\bar{d}\bar{e}\bar{f}} \sum_{i=1}^{14} F_i(p,q,k)\, \Gamma_{i\,\mu\nu\rho}(p,q,k) \quad , \tag{3.1}$$

where $\Gamma_{i\,\mu\nu\rho}(p,q,k)$ are the components of the tensor basis. The first contribution to the sum (3.1) is the tree-level contribution:

$$\Gamma_{1\,\mu\nu\rho}(p,q,k) \;=\; (q-k)_\mu\, \delta_{\nu\rho} + (k-p)_\nu\, \delta_{\rho\mu} + (p-q)_\rho\, \delta_{\mu\nu} \quad . \tag{3.2}$$

We use this vertex, as already outlined in Section 2.5.3, (2.16), since gauge-invariant perturbation theory predicts that the vertices in (2.17), (2.18) and (2.19) behave in leading order as the three-point function of the elementary fields. The three-point function of elementary fields is dominated by the tree-level contributions. The other 13 tensor structures can be found in [11].

The dressing functions $F_i(p,q,k)$ are the quantities to be calculated here. They are the so-called *form factors*. In fact, we are only interested in $F_1(p,q,k)$ due to the reasons described above. Now, the three-point function of the composite operator is identified with the three-W-vertex

$$G^{\bar{a}\bar{b}\bar{c}}_{\mu\nu\rho}(p,q,k) \;=\; \frac{1}{V}\left\langle O^{\bar{a}}_{\mu\,1^-_3}(p)\, O^{\bar{b}}_{\nu\,1^-_3}(q)\, O^{\bar{c}}_{\rho\,1^-_3}(k)\right\rangle \quad . \tag{3.3}$$

The factor V is the considered volume and is inherited from [9]. Though all results from Chapter 5 are calculated using the volume as in (3.3), we're hiding this factor as

$$\frac{1}{V}\left\langle O^{\bar{a}}_{\mu\,1^-_3}(p)\, O^{\bar{b}}_{\nu\,1^-_3}(q)\, O^{\bar{c}}_{\rho\,1^-_3}(k)\right\rangle \to \left\langle O^{\bar{a}}_{\mu\,1^-_3}(p)\, O^{\bar{b}}_{\nu\,1^-_3}(q)\, O^{\bar{c}}_{\rho\,1^-_3}(k)\right\rangle \quad . \tag{3.4}$$

This is done for convenience. The barred indices $\bar{a}\bar{b}\bar{c}$ are inherited from the open custodial indices from the composite operator. These open custodial indices are contracted by the Levi-Cita-symbol $\epsilon^{\bar{a}\bar{b}\bar{c}}$. The Levi-Cita-symbol is the only possibility to contract the indices for SU(2) since no other invariant tensor with three indices can be constructed.

The resulting tensor structure is

$$\left\langle O^{\bar{a}}_{\mu\,1^-_3}(p)\, O^{\bar{b}}_{\nu\,1^-_3}(q)\, O^{\bar{c}}_{\rho\,1^-_3}(k)\right\rangle \;=\; -ig\, D^{\bar{a}\bar{d}}_{\mu\gamma}(p)\, D^{\bar{b}\bar{e}}_{\nu\eta}(q)\, D^{\bar{c}\bar{f}}_{\rho\zeta}(k)\, \epsilon^{\bar{d}\bar{e}\bar{f}} \sum_{i=1}^{14} F_i(p,q,k)\, \Gamma_{i\,\mu\nu\rho}(p,q,k) \quad . \tag{3.5}$$

The next step is, as mentioned before, to assume that the tree-level contributions dominate the three-point function, yielding

$$\left\langle O^{\bar{a}}_{\mu\,1^-_3}(p)\, O^{\bar{b}}_{\nu\,1^-_3}(q)\, O^{\bar{c}}_{\rho\,1^-_3}(k)\right\rangle \;\approx\; -ig\, D^{\bar{a}\bar{d}}_{\mu\gamma}(p)\, D^{\bar{b}\bar{e}}_{\nu\eta}(q)\, D^{\bar{c}\bar{f}}_{\rho\zeta}(k)\, \epsilon^{\bar{d}\bar{e}\bar{f}}\, F_1(p,q,k)\, \Gamma_{1\,\mu\nu\rho}(p,q,k) \quad . \tag{3.6}$$

We identify $\Gamma^{\bar{a}\bar{b}\bar{c}}_{\mu\nu\rho}(p,q,k) = -ig\epsilon^{\bar{a}\bar{b}\bar{c}}\Gamma_{1\,\mu\nu\rho}(p,q,k)$, as in (2.16).

The last step is to obtain an expression for $F_1(p,q,k)$. First, all open indices in (3.6) have to be contracted. Using the orthogonality of the basis elements $\Gamma_{i\,\mu\nu\rho}(p,q,k)$, the only non-vanishing contribution is

$$\begin{aligned}\left\langle \Gamma^{\bar{a}\bar{b}\bar{c}}_{\mu\nu\rho}(p,q,k)\; O^{\bar{a}}_{\mu\,1^-_3}(p)\, O^{\bar{b}}_{\nu\,1^-_3}(q)\, O^{\bar{c}}_{\rho\,1^-_3}(k)\right\rangle \;&=\\ \Gamma^{\bar{a}\bar{b}\bar{c}}_{\mu\nu\rho}(p,q,k)\, F_1(p,q,k)\, D^{\bar{a}\bar{d}}_{\mu\gamma}(p)\, D^{\bar{b}\bar{e}}_{\nu\eta}(q)\, D^{\bar{c}\bar{f}}_{\rho\zeta}(k)\, \Gamma^{\bar{d}\bar{e}\bar{f}}_{\mu\nu\rho}(p,q,k) \quad .\end{aligned} \tag{3.7}$$

Solving for $F_1(p,q,k)$ yields

$$F_1(p,q,k) \;=\; \frac{\left\langle \Gamma^{\bar{a}\bar{b}\bar{c}}_{\mu\nu\rho}(p,q,k)\, O^{\bar{a}}_{1_3^-\,\mu}(p)\, O^{\bar{b}}_{1_3^-\,\nu}(q)\, O^{\bar{c}}_{1_3^-\,\rho}(k)\right\rangle}{\Gamma^{\bar{a}\bar{b}\bar{c}}_{\mu\nu\rho}(p,q,k)\, D^{\bar{a}\bar{d}}_{\mu\gamma}(p)\, D^{\bar{b}\bar{e}}_{\nu\eta}(q)\, D^{\bar{c}\bar{f}}_{\rho\zeta}(k)\, \Gamma^{\bar{d}\bar{e}\bar{f}}_{\gamma\eta\zeta}(p,q,k)} \quad . \tag{3.8}$$

This is exactly the expression assumed for the different ratios in section 2.5.3.

3.3 Taylor Expansion of the form factor

Using a Taylor expansion of the form factor the radius of a particle can be determined. The following construction follows [10].

Let $F(q^2)$ be a form factor, which can be

$$F(q^2) \;=\; \frac{1}{\int \mathrm{d}V\, \rho(\boldsymbol{r})} \int_\Omega \mathrm{d}V\, \rho(\boldsymbol{r}) e^{\frac{i\boldsymbol{q}\cdot\boldsymbol{r}}{\hbar}} \quad . \tag{3.9}$$

For a spherical particle we obtain

$$F(q^2) \;=\; \frac{\hbar}{q\int \mathrm{d}r\, r^2\rho(r)} \int_0^\infty \mathrm{d}r\, \rho(r) r \sin\left(\frac{qr}{\hbar}\right) \quad . \tag{3.10}$$

A series expansion of the sine in (3.10) yields

$$F(q^2) \;=\; \frac{\hbar}{\int \mathrm{d}r\, r^2\rho(r)} \int_0^\infty \mathrm{d}r\, \rho(r) r \left[\frac{qr}{\hbar} - \frac{1}{6}\left(\frac{qr}{\hbar}\right)^3 + \cdots\right] \quad , \tag{3.11}$$

where we neglect all higher order terms. The form factor then becomes

$$F(q^2) \;\approx\; 1 - \frac{q^2}{6\hbar} \underbrace{\frac{\int_0^\infty \mathrm{d}r\, r^2\rho(r) r^2}{\int_0^\infty \mathrm{d}r\, r^2\rho(r)}}_{1} \quad . \tag{3.12}$$

The expression 1 is the expectation value of the squared radius. This radius is exactly the quantiy we will later exploit to obtain the size of the physical W bound-state. We obtain

$$F(q^2) \;\approx\; 1 - \frac{q^2}{6\hbar}\left\langle r^2\right\rangle \quad . \tag{3.13}$$

On the other hand Taylor expansion of the form factor in q^2 gives

$$F(q^2) \;=\; F(0) \;+\; \left.\frac{\mathrm{d}F(q^2)}{\mathrm{d}q^2}\right|_{q^2=0} q^2 \;+\; \cdots \quad , \tag{3.14}$$

where $F(0) = 1$, see [10]. Using (3.13) yields

$$\left.\frac{\mathrm{d}F(q^2)}{\mathrm{d}q^2}\right|_{q^2=0} = -\frac{1}{6\hbar}\left\langle r^2\right\rangle \quad , \tag{3.15}$$

and therefore

$$F(q^2) \approx 1 - \frac{1}{6\hbar}\left\langle r^2\right\rangle q^2 \quad . \tag{3.16}$$

Thus the form factor is to leading order a linear function in q^2 with a slope proportional to $\left\langle r^2\right\rangle$.

3.4 The size of the W-boson

From (3.15) we take the expectation value of the radius and define the radius as

$$r := \mathrm{sign}\left(\left\langle r^2\right\rangle\right)\sqrt{\left|\left\langle r^2\right\rangle\right|} \tag{3.17}$$

Taking into account the result from gauge-invariant perturbation theory (2.9) and the arguments mentioned in section 3.2, only the tree-level[1] form factors (2.17), (2.18) and (2.19) are used to obtain a radius of the physical W-boson.

For clarity we shortly summarize the main ideas of the construction:

1. A scattering process is identified with a three-point interaction of a composite operator.
2. Gauge-invariant perturbation theory gives an estimate that the tree-level contributions dominate this process.
3. The tree-level tensor structure is employed to contract, amputate and therefore correctly project the three-point function onto tree-level.
4. A Taylor expansion of the form factor yields the radius of the physical W-boson.

[1]Note, that one can in fact calculate a radius for each of the 13 tensor elements, but gauge-invariant perturbation theory suggests to use the tree-level tensor element.

Chapter 4

Lattice technology

In this chapter the lattice methods used to perform calculations for the objects described in Chapter 2 are discussed. A brief introduction to the used techniques is given and the central objects of the calculation are discussed. We follow [6], [8], [12], [13] and [14] . Note that we only cover the very basics of the lattice formalism. For a detailed treatment of lattice field theory the reader is refered to [12] and [13].

4.1 Lattice gauge theory

The basic setup is a 4-dimensional isotropic hypercubic lattice with lattice constant a and a lattice volume $V = L^4$. The starting point here is the unimproved lattice version of the action (2.1)

$$\begin{aligned} S \;=\; \beta \sum_x \left(1 \,-\, \frac{1}{2} \sum_{\mu<\nu} \mathrm{Retr} U_{\mu\nu}(x) \right) + \phi(x)^\dagger \phi(x) + \lambda \left(\phi(x)^\dagger \phi(x) - 1 \right)^2 \\ - \kappa \sum_\mu \left(\phi(x)^\dagger U_\mu(x) \phi(x+e_\mu) + \phi(x+e_\mu)^\dagger U_\mu(x)^\dagger \phi(x) \right) \quad , \end{aligned} \tag{4.1}$$

$$U_{\mu\nu}(x) \;=\; U_\mu(x) U_\nu(x+e_\mu) U_\mu(x+e_\nu)^\dagger U_\nu(x)^\dagger \quad , \tag{4.2}$$

$$W_\mu \;=\; \frac{1}{2agi} \left(U_\mu(x) - U_\mu(x)^\dagger \right) + \mathcal{O}(a^2) \quad , \tag{4.3}$$

where the following abbreviations are used [8]

$$\begin{aligned} \beta \;&=\; \frac{4}{g^2} \quad , \\ a^2 m_0^2 \;&=\; \frac{(1-2\lambda)}{\kappa} - 8 \quad , \\ \lambda \;&=\; \kappa^2 \gamma \quad . \end{aligned} \tag{4.4}$$

Here $U_\mu = \exp(igaW_\mu)$ is the so-called link, ϕ is the Higgs-field, and e_μ is the unit vector in μ-direction. The parameters β, κ and λ are the couplings at the lattice cut-off $\frac{1}{a}$, m_0 is the bare mass of the Higgs. Both, the links and the scalar fields obey periodic boundary conditions, i.e.,

$$\phi(x + e_\mu L) = \phi(x) \quad \text{and} \quad U_\mu(x + e_\nu L) = U_\mu(x)\,, \quad \forall\, x, \mu \quad . \tag{4.5}$$

Under gauge transformations the links and the scalar fields transform as

$$\phi(x) \to G(x)\phi(x) \quad , \quad U_\mu(x) \to G(x)U_\mu(x)G(x+e_\nu)^\dagger\,, \quad \forall\, x, \mu, \nu; \quad G(x) \in \mathrm{SU}(2) \quad . \tag{4.6}$$

The partition function is

$$Z = \int \mathcal{D}\,[U,\phi]\,\mathrm{e}^{-S[U,\phi]} \quad \text{with} \quad \mathcal{D}\,[U,\phi] = \left(\prod_x \prod_{\mu=1}^{4} \mathrm{d}U_\mu(x)\right)\left(\prod_x \mathrm{d}\phi(x)\right) \quad , \tag{4.7}$$

where the gauge-field measure is the Haar measure [13], and the integration over the scalar field is an integration over $\mathbb{C}^2$ at every lattice site x. It is important to note that both measures are invariant under gauge transformations (4.6).

4.2 Creation of configurations

We follow here [8], [14] and [15]. A combination of one heat bath and 5 overrelaxtion sweeps are employed for the gauge-fields. One Metropolis sweep has been performed between every 6 gauge-field updates to update the Higgs-field. For the Higgs-field a gaussian proposal was used. The width of the Gaussian proposal is tuned to achieve a 50% acceptance probability. These 12 sweeps constitute a single update for the field configuration. The auto-correlation time of the plaquette is of the order of 1 or less such updates. L such updates seperate a measurement of gauge invariant observables to reduce the auto-correlation time. For thermalization $2(10L + 300)$ such updates have been performed before the measurement starts. Errors of measured observables were calculated using bootstrap. All errors not accessible by bootstrap were calculated using error propagation. The code was back-checked with the results of [8] and [14]. Several sanity checks involving the effective mass, the behaviour of the propagators and the analytic results for the tensor structure have been performed through the whole process of programming. The analytic results for the tensor structure are shown in Appendix B.

4.3 The operator, the projectors and the vertex on the lattice

All objects of interest from section 2 have to be put on the lattice. First, the 1_3^- channel composite oberator (2.7) has to be reformulated using variables accessible on the lattice. We obtain

$$O^{\bar{a}}_{1_3^-\,\mu}(x) \;=\; \mathrm{tr}\left[\tau^{\bar{a}}\frac{X(x)^\dagger}{\sqrt{\det\left(X(x)\right)}}U_\mu(x)\frac{X(x+e_\mu)}{\sqrt{\det\left(X(x+e_\mu)\right)}}\right] \quad . \tag{4.8}$$

where $X(x)$ is the Higgs-matrix from (2.4).

The next step is to improve the projectors and the vertex for the lattice. The lattice transverse and longitudinal projectors are given by

$$T_{\mu\nu}(p) \;=\; \delta_{\mu\nu} - \frac{\sin\left(\frac{p_\mu}{2}\right)\sin\left(\frac{p_\nu}{2}\right)}{\sum_{\rho=1}^4 \sin^2\left(\frac{p_\rho}{2}\right)} \quad , \quad L_{\mu\nu}(p) \;=\; \frac{\sin\left(\frac{p_\mu}{2}\right)\sin\left(\frac{p_\nu}{2}\right)}{\sum_{\rho=1}^4 \sin^2\left(\frac{p_\rho}{2}\right)} \quad . \tag{4.9}$$

The lattice improved version of (2.16) is [12]

$$\begin{aligned}\Gamma^{\bar{a}\bar{b}\bar{c}}_{\mu\nu\rho}(p,q,k) \;=\; -ig\epsilon^{\bar{a}\bar{b}\bar{c}}\mathrm{e}^{\frac{i}{2}(p_\mu+q_\nu+k_\rho)}\Bigg[&2\sin\left(\frac{q_\mu-k_\mu}{2}\right)\delta_{\nu\rho}\cos\left(\frac{p_\nu}{2}\right)\\ &+2\sin\left(\frac{k_\nu-p_\nu}{2}\right)\delta_{\mu\rho}\cos\left(\frac{q_\rho}{2}\right)+2\sin\left(\frac{p_\rho-q_\rho}{2}\right)\delta_{\mu\nu}\cos\left(\frac{k_\mu}{2}\right)\Bigg] \quad ,\end{aligned} \tag{4.10}$$

where $p_\mu = \frac{2\pi}{L}n_\mu$, with $n_\mu = 0, 1, \cdots, \frac{L}{2}$.

The lattice versions of the nominator and the denominator in (2.20), (2.21) and (2.22) can be decomposed into different constituents. One can calculate the values of some of these constituents analytically and show that some of these vanish, see Appendix A. The decomposition can be exploited to accelerate the code for calculating the lattice expressions of (2.20), (2.21) and (2.22).

Chapter 5

Results

In this chapter we show and discuss the results obtained from lattice simulations. All lattice calculations are done by a lattice-program provided by Axel Maas. The implementation of the bound-state operator (4.8) and all analytics are programmed and done by the author. All results for the gauge-fixed elementary fields are calculated and analyzed using programs provided by Axel Maas [8, 9, 14].

5.1 The Setup

We calculated all results on lattices with sizes $L = 8, 12, 16, 20$ with 5 different sets of parameters denoted with the letters A,B,C,D and E. These are shown in Table 5.1.

Here, α_{W} is the weak coupling at a minimal momentum of 200 GeV, $\frac{1}{a}$ is the inverse lattice spacing obtained from the effective masses of the 1_3^- operator [7, 8, 16] and β, κ, λ are the parameters of the theory.

It is important to note that these data do not follow a line of constant physics. Therefore, thus exists the possibility for all the different parameter sets to describe different physics.

Table 5.1: Table containing all 5 sets of parameters.

Parameter set	$\frac{1}{a}$[GeV]	β	κ	λ	α_{W}
A	453	2.7984	0.2927	1.317	0.605
B	438	4.2	0.2736	1	0.106
C	335	2.7987	0.2953	1.267	0.506
D	255	4	0.3	1	0.211
E	151	2.3634	0.3223	1.066	0.558

TABLE 5.2: Table containing the number of configurations/measurements for each size and each set of parameters.

Lattice Size	A, # of configurations	B, # of configurations	C, # of configurations	D, # of configurations	E, # of configurations
8	1032200	1032200	1032200	1032200	1032200
12	680625	687500	687500	687500	687500
16	254700	254700	254700	254700	254700
20	198400	197408	198400	198400	198400

For the mass of the W-boson we use the experimentally determined value of $m_{WE} = 80.375$ GeV. The amount of satistics, i.e., the number of configurations, for all sets of parameters and lattice sizes is shown in Table 5.2.

5.2 The propagator

The first object to be discussed is the propagator in momentum space. We calculated the propagator using (2.11) and (2.14) with the lattice improved projectors (4.9). The propagator is plotted together with the analytic groundstate propagator

$$D(p) = \frac{1}{p^2 + m_{WE}^2} \quad , \tag{5.1}$$

and the propagator of the gauge fixed elementary fields [9] in Figure 5.1. Note, that we use physical momenta, i.e., $p_{\mu\,\mathrm{phys}} = \frac{2}{a}\sin\left(\frac{p_\mu}{2}\right)$. For the lattice momenta see Appendix B and [17].

The propagators are renormalized using the value of (5.1) at $p = 0$.

In Figure 5.1 one can observe there are several problems:

- The transverse part of the propagator of the physical composite state is not a monotonously increasing function of the momentum. This is due to lattice artifacts as we show in the next section.
- The longitudinal part of the propagator of the physcial composite state is not constant, as we would expect from standard perturbation theory [18]. Again, this can be understood by studying the lattice artifacts.
- The propagator of the elementary W-field is below the groundstate propagator. This is unphysical, since the physical groundstate propagator (5.1) gives already a lower bound on all other propagators. This behaviour is caused by negative norm contributions of the elementary W-fields due to gauge dependence.

The next step is to reduce the lattice artifacts present in the propagator. An in-detail discussion of lattice artifacts can be found in [12].

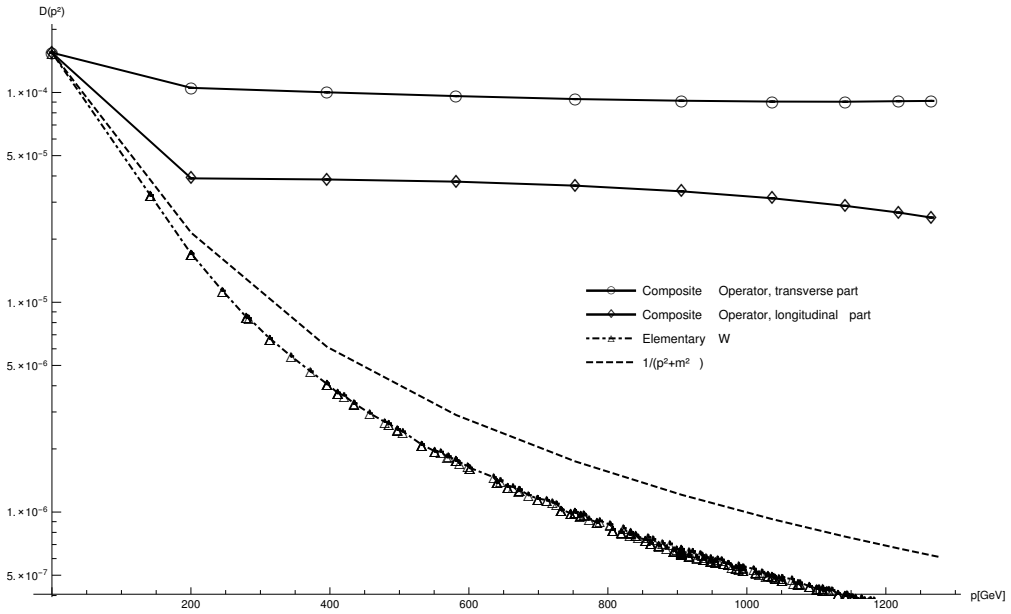

FIGURE 5.1: Plot for the propagator in momentum space for parameter set A and lattice size $L = 20$

5.2.1 Treatment of lattice artifacts for the transverse part

The transverse part of the propagator for the composite state was plotted as

$$D_{\mathrm{T}}(p)\, p^2 - b \sin\left(\frac{p}{2}\right)^{\frac{3}{2}} \quad . \tag{5.2}$$

This ansatz was used because of

$$D(p^2)_{\mathrm{T}} = \sum \frac{Z_i}{p^2 + m_i^2} \overset{p^2 >> m_i^2}{\rightarrow} \frac{\sum Z_i}{p^2} \tag{5.3}$$

and therefore $D(p^2)_{\mathrm{T}}\, p^2$ becomes constant for large momenta [18]. Here p is the lattice momentum (B.11).

The parameter b was then tuned such so that (5.2) shows a constant behaviour for the largest momenta. This is shown in Figure 5.2. This improvement is purely phenomenological and proper improvements can be obtained using lattice perturbation theory [12]. The transverse improved propagator for the composite state, is shown in Figure 5.3.

5.2.2 Treatment of lattice artifacts for the longitudinal part

The lattice artifacts in the longitudinal part were reduced using

$$a + b \cos\left(\frac{p}{2}\right)^{-\frac{5}{4}} \tag{5.4}$$

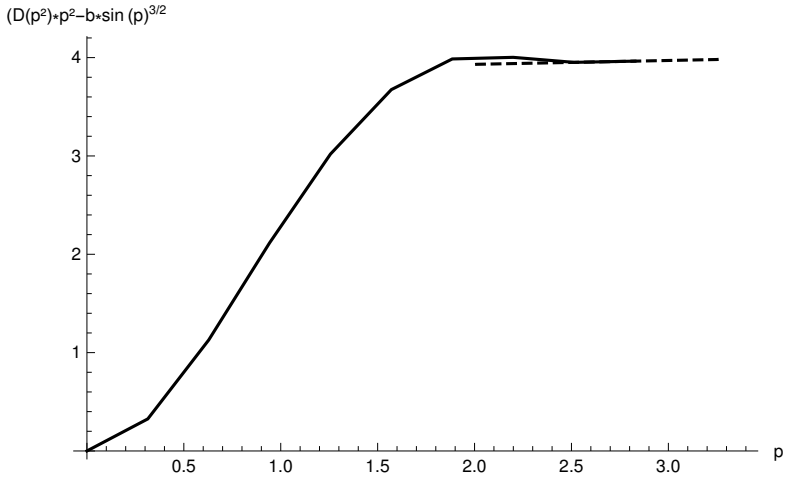

FIGURE 5.2: Plot for (5.2) for parameter set A and lattice size $L = 20$. The dashed line shows the wanted constant behaviour for large momenta. Here $b = 2.55$.

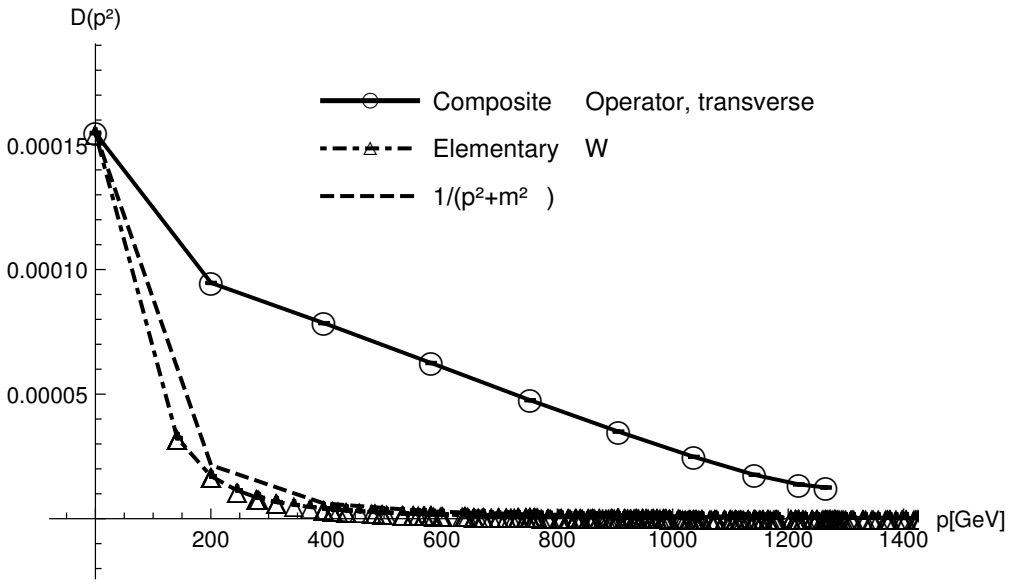

FIGURE 5.3: Plot for the propagator in momentum space for parameter set A and lattice size $L = 20$. Here the lattice artifacts were reduced using the discussed procedure.

to fit the longitudinal part of the composite state. Then $b \cos\left(\frac{p}{2}\right)^{-\frac{5}{4}}$ is subtracted of the longitudinal part and we set $D_{\mathrm{L}}(0) = a$. This improvement is again purely phenomenological. The improved longitudinal part is shown in Figure 5.4.

5.2.3 Propagator with reduced lattice artifacts

As can be seen in Figure 5.4 the propagator of the transverse part is monotonously decreasing and that the one of longitudinal part has an almost constant behaviour. The

last points of the parameter sets D and E are deviations from the constraint for the transverse part to be monotonously decreasing, this is shown in Figure 5.5 and can be attributed to lattice artifacts as well. All plots for all sets of parameters and for all lattice sizes not shown here can be found in Appendix C.

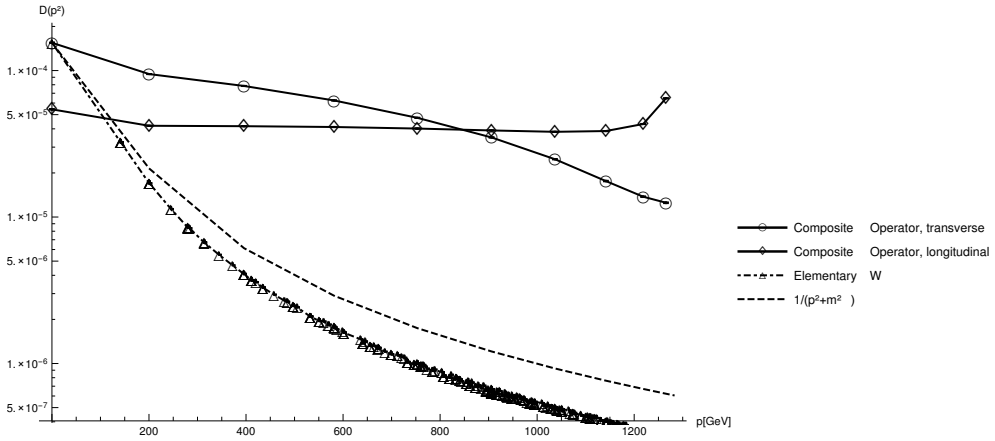

FIGURE 5.4: Plot for the propagator in momentum space for parameter set A and lattice size $L = 20$. Here the lattice artifacts were reduced using the discussed procedure.

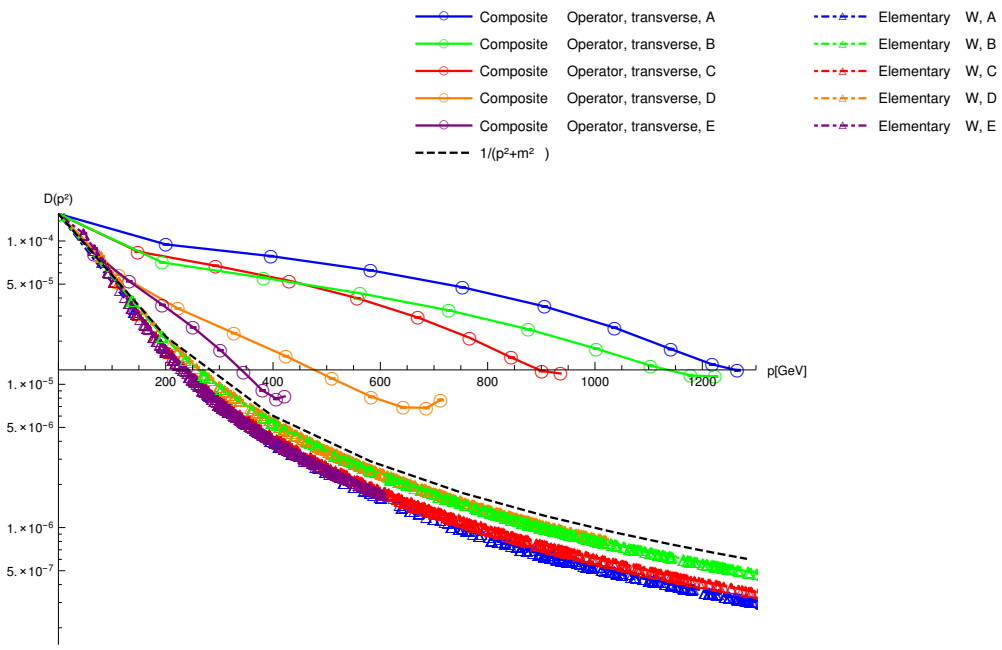

FIGURE 5.5: Plot for the transverse parts for all sets of parameters for lattice size $L = 20$. Here the lattice artifacts were reduced using the discussed procedure.

5.2.4 Summary of the propagator results

The results for the gauge-invariant composite operator showed relatively large lattice artifacts which have to be reduced to get convincing results. After reducing these artifacts we see that the transverse part of the propagator for the composite state is far above the tree level groundstate, this is due to the fact that excited states still contribute to the operator we used. Those excited states add additional poles to the propagator, shifting the result higher than the ground-state propagator. Using an operator with perfect overlap with the ground-state would shift the result ontop of the physical propagator. The propagator for the gauge-fixed W-field is always below the analytic ground-state. This is a non-physical behaviour and shows that, due to the gauge dependence of these fields, these observables do not show the behaviour predicted by gauge theory.

5.3 The ratio

In this Section we discuss the results for the ratios defined in (2.20),(2.21) and (2.22). All ratios were normalized setting $R(0,0,0) = 1$ This can be seen in the Figures 5.26 and 5.27. For the ratios we used a linear fit at small momenta to expand the ratio to $p^2 = 0$.

Figure 5.6 shows the result for (2.20) for parameter set A and $L = 20$. The plots for all other parameter sets and lattice sizes can be found in Appendix D.

In Figure 5.6 one can see that the ratio is decreasing for low momenta.

Figure 5.7 shows the results for the same setup but now for the ratio of the elementary W-field. Here one can see that this function is increasing for low momenta. This is the first hint for the elementary ratio to be unphysical, since a positive slope yields a negative radius (3.15), (3.17). All results concerning the radius are discussed in detail in Section 5.4.

In the Figures 5.8 and 5.9 the results of the other ratios, (2.21) and (2.22), are plotted. The qualitative behaviour is the same as for the ratio shown in Figure 5.6.

Figure 5.10 shows a comparison between the ratio of the elementary field and the one from the composite state. Again plots for all other configurations can be found in Appendix D.

Next we want to compare the results for all different sets of parameters with each other. This is shown in Figure 5.11. There, one can see that the ratio is always close to zero for large momenta for each set of parameters. In fact the the point for the second largest

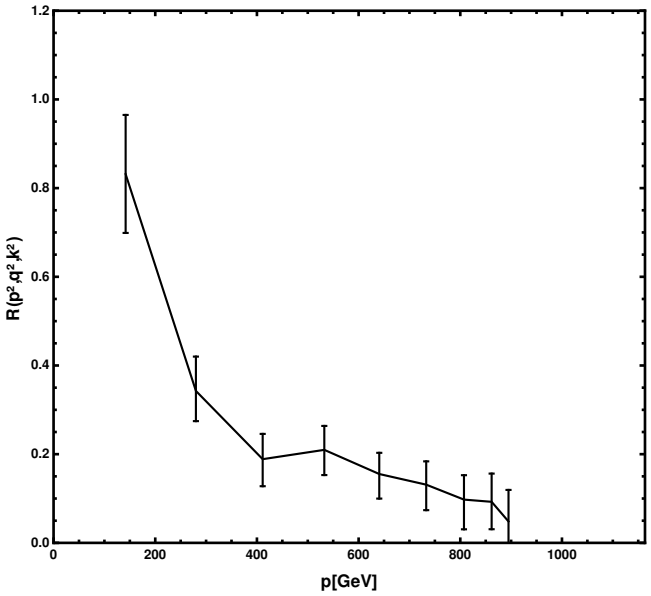

FIGURE 5.6: Plot of the ratio (2.20) of the gauge-invariant composite operator for parameter set A and lattice size $L = 20$.

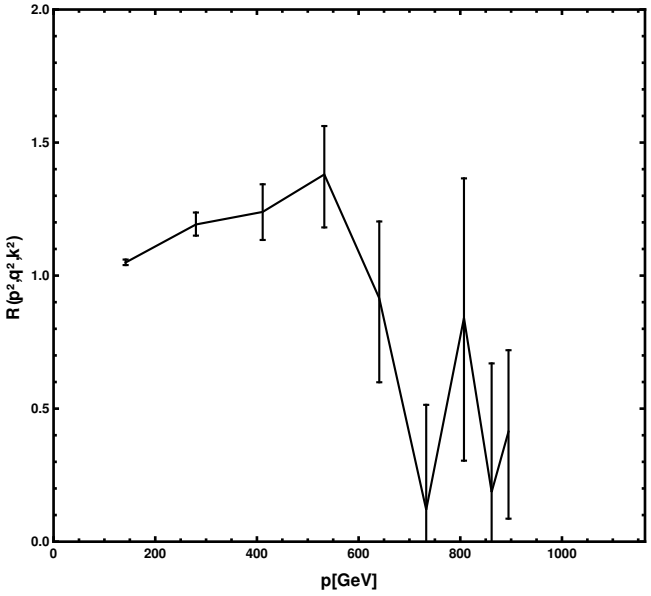

FIGURE 5.7: Plot of the ratio of the elementary fields for parameter set A and lattice size $L = 20$.

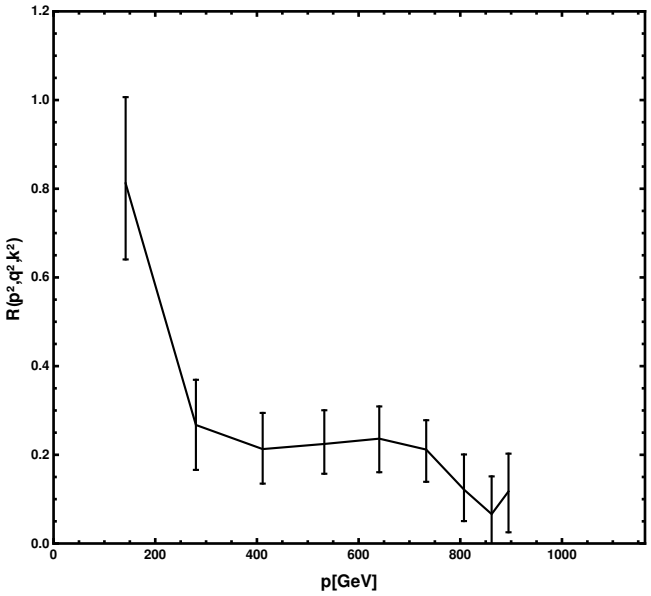

FIGURE 5.8: Plot of the ratio of the gauge-invariant composite operator for parameter set A and lattice size $L = 20$ for the transverse-only ratio (2.21).

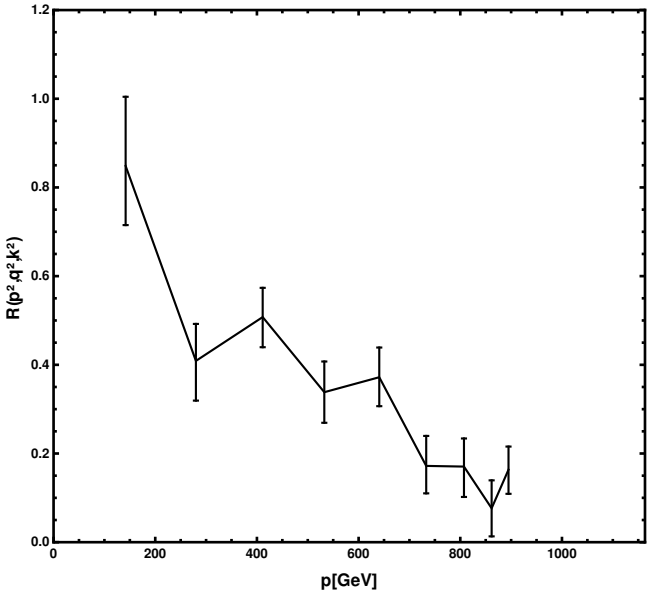

FIGURE 5.9: Plot of the ratio of the gauge-invariant composite operator for parameter set A and lattice size $L = 20$ for the ratio with one momentum vanishing.(2.22).

momentum is in most cases the closest to zero, this is due to lattice artifacts, and in the next section we try to compensate this.

5.3.1 Treatment of lattice artifacts for the ratio

In Figure 5.11 the ratio is contaminated by lattice artifacts for large momenta. To resolve this we use again some phenomenological improvements for the ratios. This resulted in

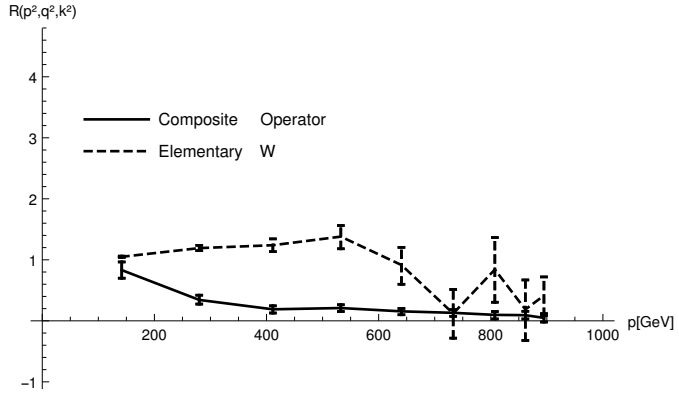

FIGURE 5.10: Plot of the ratio of the elementary fields and the composite state for parameter set A and lattice size $L = 20$. Equal momentum configuration (2.20).

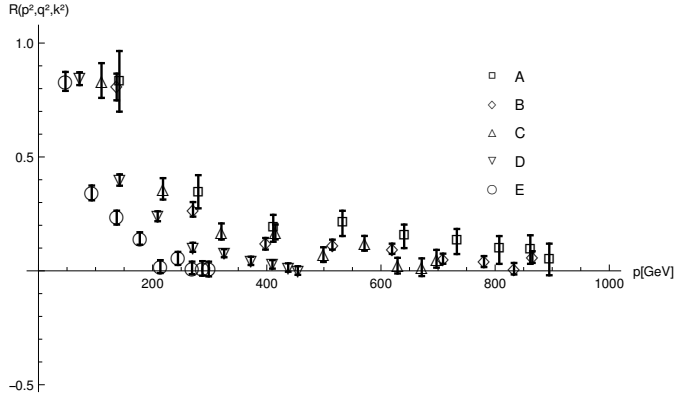

FIGURE 5.11: Plot of the ratio of the gauge-invariant composite operator for all sets of parameters and lattice size $L = 20$. Equal momentum configuration (2.20).

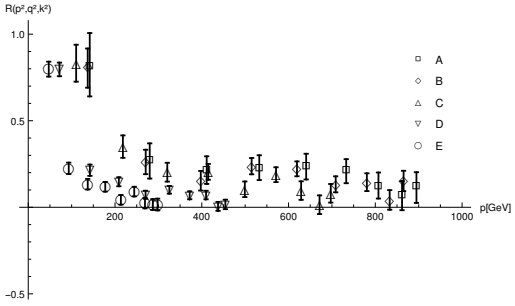

FIGURE 5.12: Plot of the ratio of the gauge-invariant composite operator for all sets of parameters and lattice size $L = 20$. Transverse-only (2.21).

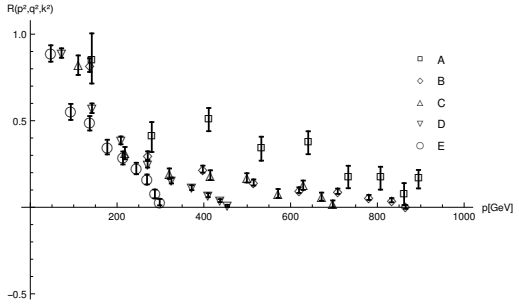

FIGURE 5.13: Plot of the ratio of the gauge-invariant composite operator for all sets of parameters and lattice size $L = 20$. One momentum vanishing (2.22).

multiplying the values of the ratios with cosine-functions with different exponents. The applied improvements are

$$R(p^2, q^2, k^2) \;\rightarrow\; R(p^2, q^2, k^2) \cos\left(\frac{p}{2}\right)^{-1} \quad , \tag{5.5}$$

$$R(p^2,q^2,k^2) \;\to\; R(p^2,q^2,k^2)\cos\left(\frac{p}{2}\right)^{-4/3} \quad , \tag{5.6}$$

$$R(p^2,q^2,k^2) \;\to\; R(p^2,q^2,k^2)\cos\left(\frac{p}{2}\right)^{-3/2} \quad , \tag{5.7}$$

$$R(p^2,q^2,k^2) \;\to\; R(p^2,q^2,k^2)\cos\left(\frac{p}{2}\right)^{-2} \quad , \tag{5.8}$$

where p, q, k are the lattice momenta (B.11). The results for the improvements are shown in the Figures 5.14, 5.15, 5.16, 5.17, 5.18 and 5.19.

One can see the value and the error for the largest momentum sometimes becomes very large because of the division of the original ratio. Therefore, the last point is not very reliable. The improvements (5.7) and (5.8) were applied to the equal momentum configuration and to the transverse-only ratio. From these (5.7) works best to obtain a behaviour that shows less influence by lattice artifacts. For the configuration with one momentum vanishing this has to be reconsidered. Since one momentum is set to zero, we apply (5.5) and (5.6) for this configuration. Here, (5.5) works best. The plots for all configurations, all sets of parameters and all improvements can be found in Appendix D.

In the plots for all sets of parameters with the improved ratio 5.20, 5.21, 5.22, D.84,

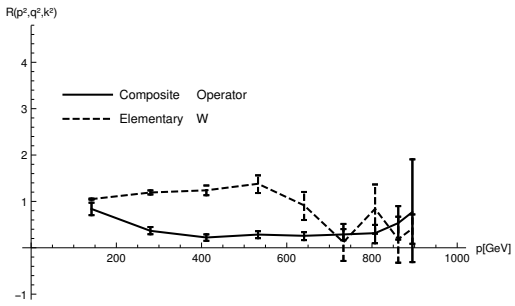

FIGURE 5.14: Plot of the ratio for the improvement (5.7) for parameter set A and lattice size $L = 20$. Equal momentum configuration (2.21)

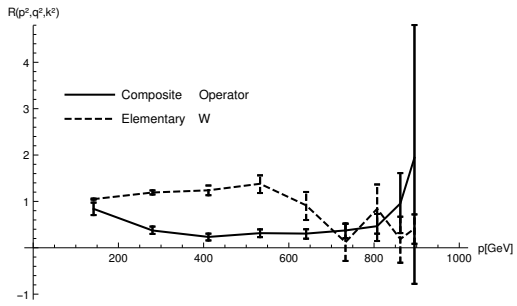

FIGURE 5.15: Plot of the ratio for the improvement (5.8) for parameter set A and lattice size $L = 20$. Equal momentum configuration (2.21)

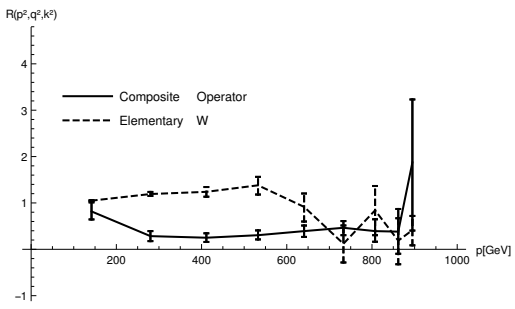

FIGURE 5.16: Plot of the ratio for the improvement (5.7) for parameter set A and lattice size $L = 20$. Transverse-only ratio (2.22)

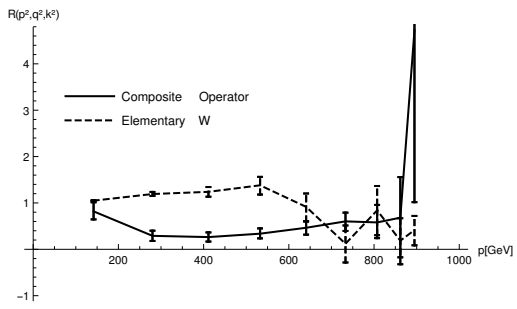

FIGURE 5.17: Plot of the ratio for the improvement (5.8) for parameter set A and lattice size $L = 20$. Transverse-only ratio (2.22)

5.24 and 5.25, one can clearly see that the influence of the lattice artifacts is decreased. For small momenta the improvements have allmost no effect on the ratios as expected from the cosine improvements. The plots for all other lattice sizes and plots with a fixed parameter set for all sizes can be found in Appendix D.

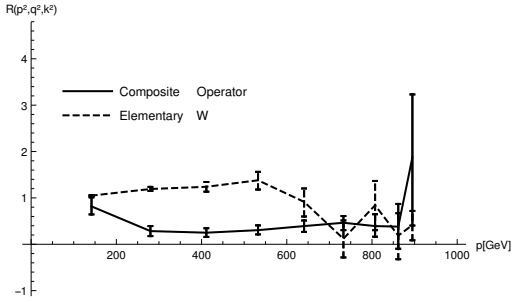

FIGURE 5.18: Plot of the ratio for the improvement (5.5) for parameter set A and lattice size $L = 20$. One momentum vanishing (2.22)

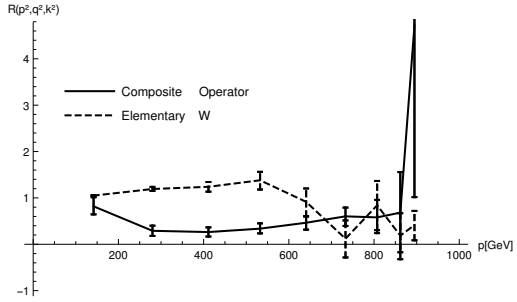

FIGURE 5.19: Plot of the ratio for the improvement (5.6) for parameter set A and lattice size $L = 20$. One momentum vanishing (2.22)

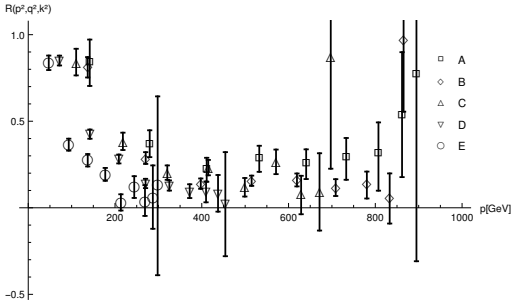

FIGURE 5.20: Plot of the ratio for the improvement (5.7) for all sets of parameters and lattice size $L = 20$. Equal momentum configuration (2.20)

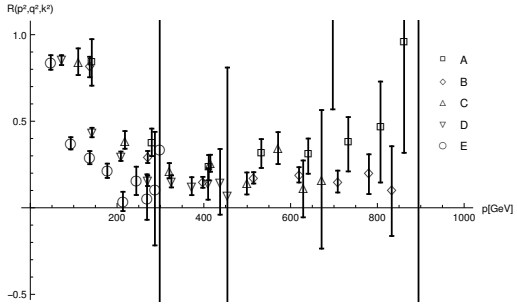

FIGURE 5.21: Plot of the ratio for the improvement (5.8) for all sets of parameters and lattice size $L = 20$. Equal momentum configuration (2.20)

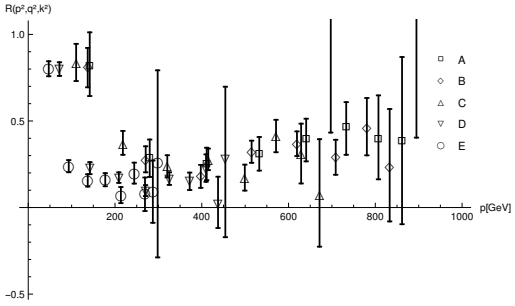

FIGURE 5.22: Plot of the ratio for the improvement (5.7) for all sets of parameters and lattice size $L = 20$. Transverse-only ratio (2.21)

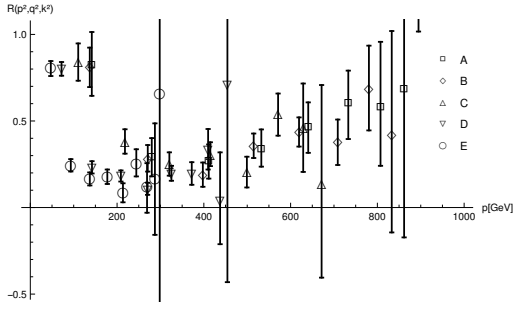

FIGURE 5.23: Plot of the ratio for the improvement (5.8) for all sets of parameters and lattice size $L = 20$. Transverse-only ratio (2.21)

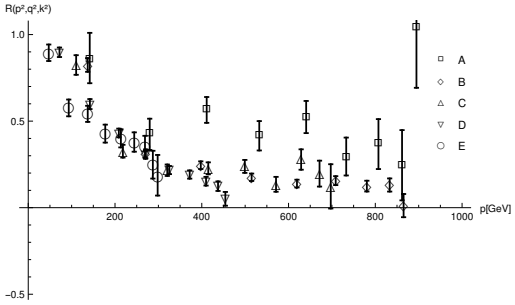

FIGURE 5.24: Plot of the ratio for the improvement (5.5) for all sets of parameters and lattice size $L = 20$. One momentum vanishing (2.22)

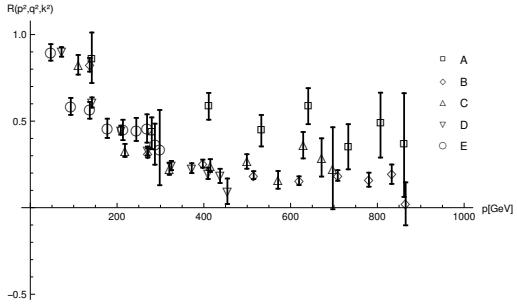

FIGURE 5.25: Plot of the ratio for the improvement (5.6) for all sets of parameters and lattice size $L = 20$. One momentum vanishing (2.22)

5.4 Determination of the radii

In this section we show results for the radii as discussed in Section 3.4.
Starting with (3.15) we need to determine the slopes of the ratios (2.20),(2.21) and (2.22) at zero momenta. Because these cannot be computed, due to a division by zero, we fit the lowest two momenta linear and extrapolate to zero momentum. The slope of the linear fit is used to determine the size. In Figures 5.26 and 5.27 the linear fits are depictured. The errors are determined taking upper and lower estimates for the slope as shown in Figures 5.26 and 5.27. Using this and formula (3.15) we obtain radii for all

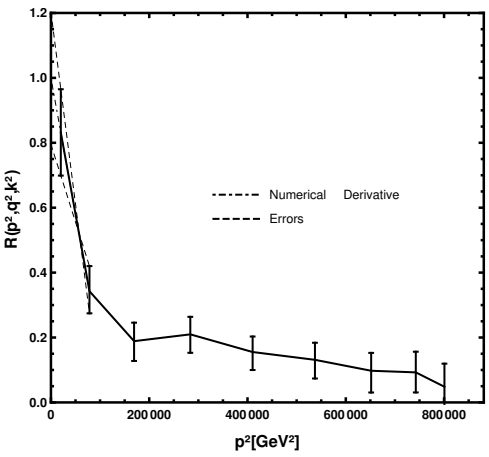

FIGURE 5.26: Plot of the ratio for parameter set A and lattice size $L = 20$ with the corresponding linear fit for small momenta. Equal momentum configuration (2.22)

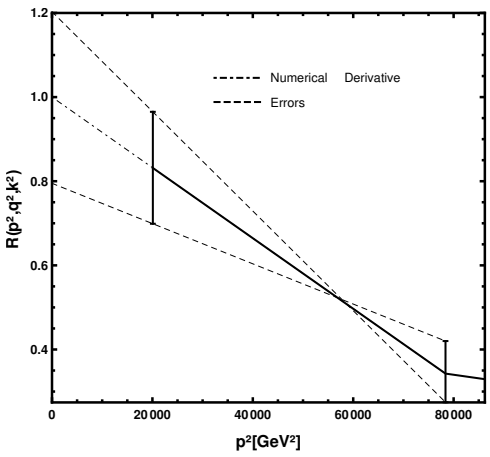

FIGURE 5.27: Plot of the ratio for parameter set A and lattice size $L = 20$ with the corresponding linear fit for small momenta. Equal momentum configuration (2.22)

sets of parameters, lattices sizes, different improvements and momentum configurations. Data for the composite state is collected in the Tables 5.3, 5.5 and 5.6 and in Appenidx E.

The data for the elementary field is collected in the Tables 5.4 and 5.7 and in Appenidx E.

For the composite states one obtains negative slopes yielding real radii, but for the elementary fields we obtain in some cases positive slopes yielding negative radii. The reason why the radii are negative is given by (3.15) and by redefining the imaginary radii using (3.17). The results for the ratio therefore show the same pattern as the results for the propagators in Section 5.2: The gauge fixed elementary fields behave in an unphysical way.

The next step then is to use this data to obtain the infinite volume values of the radii. Therefore we plot the inverse radii against the inverse lattice size in physical units using a linear fit. This is shown in the Figures 5.28, 5.29 and 5.30. In these Figures one can

TABLE 5.3: Table containing the radii for all lattice sizes and all sets of parameters for the equal momentum configuration (2.20). Composite particle.

Lattice Size	A value [fm]	A Errors[fm]	B value[fm]	B Errors[fm]	C value[fm]	C Errors[fm]	D value[fm]	D Errors[fm]	E value[fm]	E Errors[fm]
8	0.00306	+0.00006/-0.00006	0.00343	+0.00004/-0.00004	0.00404	+0.00007/-0.00007	0.00694	+0.00004/-0.00004	0.0101	+0.0001/-0.0001
12	0.0038	+0.0002/-0.0002	0.0045	+0.0001/-0.0001	0.0055	-0.0002/-0.0002	0.009	+0.0001/-0.0001	0.0133	+0.0003/-0.0003
16	0.0051	+0.0008/-0.0007	0.006	+0.0004/-0.0004	0.007	+0.0007/-0.0007	0.0113	+0.0004/-0.0004	0.016	+0.001/-0.0009
20	0.007	+0.001/-0.002	0.0077	+0.0006/-0.0006	0.009	+0.001/-0.001	0.0133	+0.0008/-0.0008	0.021	+0.002/-0.002

TABLE 5.4: Table containing the radii for all lattice sizes and all sets of parameters for the equal momentum configuration (2.20). Elementary fields.

Lattice Size	A value [fm]	A Errors[fm]	B value[fm]	B Errors[fm]	C value[fm]	C Errors[fm]	D value[fm]	D Errors[fm]	E value[fm]	E Errors[fm]
8	0.0014	+0.0004/-0.0004	0.0017	+0.0003/-0.0003	0.0025	+0.0002/-0.0002	0.0039	+0.0005/-0.0005	0.0051	+0.0005/-0.0005
12	0.0011	+0.0006/-0.0004	0.0017	+0.0006/-0.0006	0	-0.0008/-0.0016	0.002	+0.002/-0.0004	-0.003	+0.002/-0.002
16	-0.0023	+0.0008/-0.0007	0.0018	+0.0015/-0.0004	-0.001	+0.0001/-0.001	0	+0.003/-0.006	-0.05	+0.004/-0.001
20	-0.0038	+0.0007/-0.007	0.004	+0.001/-0.006	-0.003	+0.001/-0.001	0	+0.02/-0.02	-0.007	+0.002/-0.005

TABLE 5.5: Table containing the radii for all lattice sizes and all sets of parameters for the transverse-only momentum configuration (2.21). Composite particle.

Lattice Size	A value [fm]	A Errors[fm]	B value[fm]	B Errors[fm]	C value[fm]	C Errors[fm]	D value[fm]	D Errors[fm]	E value[fm]	E Errors[fm]
8	0.00285	+0.00007/-0.00008	0.00294	+0.00008/-0.00008	0.0036	+0.0001/-0.0001	0.0057	+0.0001/-0.0002	0.009	+0.0002/-0.0002
12	0.0037	+0.0003/-0.0003	0.0038	+0.0003/-0.0003	0.0051	-0.0004/-0.0004	0.0087	+0.0003/-0.0003	0.0138	+0.0004/-0.0004
16	0.005	+0.001/-0.001	0.006	+0.001/-0.001	0.007	+0.001/-0.001	0.0124	+0.0007/-0.0007	0.018	+0.001/-0.001
20	0.007	+0.002/-0.002	0.007	+0.001/-0.001	0.009	+0.002/-0.002	0.0152	+0.0009/-0.001	0.023	+0.001/-0.002

TABLE 5.6: Table containing the radii for all lattice sizes and all sets of parameters for the configuration with one momentum vanishing (2.22). Composite particle.

Lattice Size	A value [fm]	A Errors[fm]	B value[fm]	B Errors[fm]	C value[fm]	C Errors[fm]	D value[fm]	D Errors[fm]	E value[fm]	E Errors[fm]
8	0.0024	+0.0001/-0.0001	0.00305	+0.00004/-0.00004	0.00351	+0.00008/-0.00009	0.00645	+0.00003/-0.00004	0.00898	+0.00009/-0.00009
12	0.0034	+0.0003/-0.0004	0.00454	+0.00009/-0.0001	0.0053	-0.0002/-0.0002	0.0084	+0.0001/-0.0001	0.0112	+0.0003/-0.0003
16	0.0051	+0.0009/-0.0009	0.0059	+0.0003/-0.0003	0.0072	+0.0005/-0.0005	0.01	+0.0004/-0.0004	0.014	+0.001/-0.001
20	0.007	+0.002/-0.002	0.0076	+0.0005/-0.0005	0.0093	+0.0008/-0.0009	0.011	+0.001/-0.001	0.017	+0.003/-0.002

TABLE 5.7: Table containing the radii for all lattice sizes and all sets of parameters for the configuration with one momentum vanishing (2.22). Elementary fields.

Lattice Size	A value [fm]	A Errors[fm]	B value[fm]	B Errors[fm]	C value[fm]	C Errors[fm]	D value[fm]	D Errors[fm]	E value[fm]	E Errors[fm]
8	-0.0019	+0.0001/-0.0001	-0.0012	+0.0001/-0.0001	-0.00237	+0.00009/-0.00009	-0.0024	+0.0003/-0.0003	-0.0055	+0.0003/-0.0003
12	-0.0024	+0.0001/-0.0001	-0.0017	+0.0002/-0.0002	-0.003	+0.0001/-0.0001	-0.003	+0.0006/-0.0006	-0.0053	+0.009/-0.009
16	-0.0031	+0.0002/-0.0002	-0.0017	+0.0005/-0.0005	-0.0034	+0.0003/-0.0004	-0.004	+0.001/-0.001	-0.0046	+0.0009/-0.003
20	-0.0035	+0.0003/-0.0003	-0.0019	+0.0009/-0.005	-0.0041	+0.0006/-0.0005	0	+0.003/-0.006	-0.011	+0.005/-0.005

see the unphysical behaviour of the gauge-fixed elementary fields, since the radius is negative.

All results for the naive infinite volume limits are collected in the Table 5.8. One can see that the infite volume radius for the composite state and the elementary fields differ at least by a factor of 10 and those for the elementary fields are negative.

The data was fit only naively and one would need more data, to give a better estimate and a more solid statement about the infinite volume limit. However, one can see that despite of these admissions, there is a significant difference in the obtained radius for the different cases.

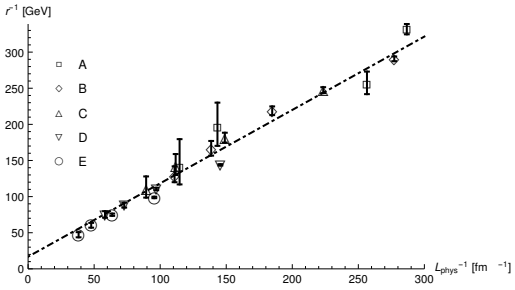

FIGURE 5.28: Plot of the radii and a naive fit for all sets of parameters at different lattice sizes L_{phys} for the composite state. Equal momentum configuration (2.21)

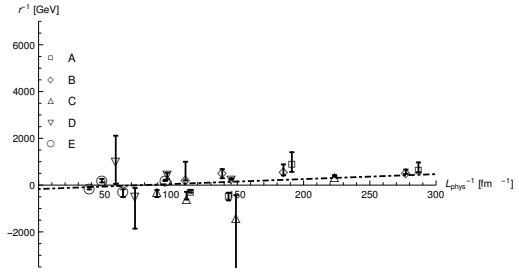

FIGURE 5.29: Plot of the radii and a naive fit for all sets of parameters at different lattice sizes L_{phys} for the elementary fields. Equal momentum configuration (2.21)

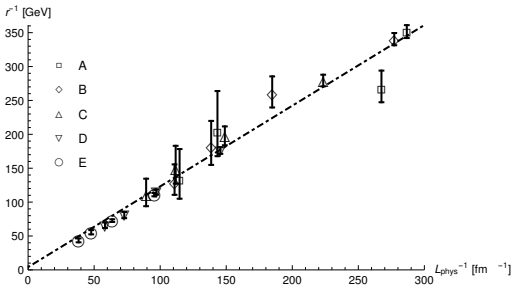

FIGURE 5.30: Plot of the radii and a naive fit for all sets of parameters at different lattice sizes L_{phys} for the composite state. Transverse-only (2.22)

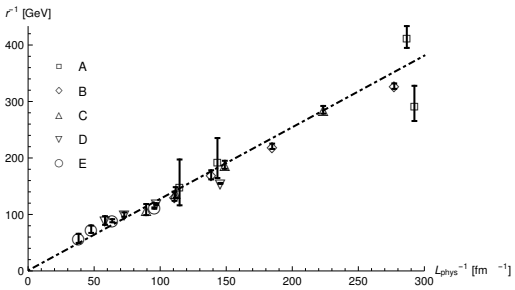

FIGURE 5.31: Plot of the radii and a naive fit for all sets of parameters at different lattice sizes L_{phys} for the composite state. One momentum vanishing (2.22)

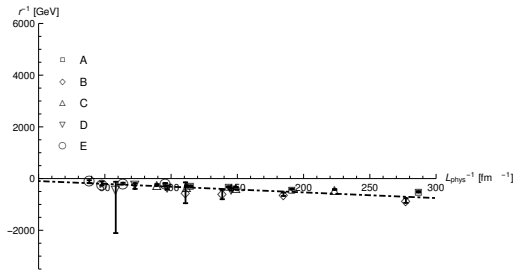

FIGURE 5.32: Plot of the radii and a naive fit for all sets of parameters at different lattice sizes L_{phys} for the elementary fields. One momentum vanishing (2.22)

TABLE 5.8: Table containing the naive infinite volume limits,using the procedure described in Section 5.4 for all momentum configurations.

Improvement	equal momentum configuration(2.20), [fm]	transverse-only configuration(2.21), [fm]	One momentum vanishing (2.22), [fm]
composite unimproved	0.059	0.244	1.26
composite using Improvement (5.7) or $(5.5)^1$	0.515	0.286	0.285
composite using Improvement (5.8) or $(5.5)^2$	0.436	0.193	0.202
elementary	-0.006		-0.01

Chapter 6

Conclusion

We have shown that propagators and vertices obtained from elementary fields and from gauge-invariant composite operators show very different behaviour. The gauge-invariant composite operator we used has been conctructed considering, that in experiment one observes a vector triplet and thus is a W-field dressed by two Higgs-fields, inheriting the triplet structure from the custodial SU(2) symmetry. Thus the gauge-invariant composite operator is a bound-state between an elementary W-field and two Higgs-fields.

The conventional way to perform computations is to use standard perturbation theory, using the elementary fields of the Lagrangian as if they are physical states. Since these fields are not gauge-invariant, gauge-fixing has to be employed to get non-vanishing expectation values. Those gauge-fixed elementary fields yield the same mass spectrum as the employed composite operator [7], but we observed drastically different results when we calculated the radius. This is shwon in Section 5.4. These results do not only differ in order of magnitude, they also show that radii calculated from gauge-dependent observables behave in a non-phyiscal way, i.e. they are negative.

An answer to the question why perturbation theory is in agreement with the experimental results, is given by gauge-invariant perturbation theory. Gauge-invariant perturbation theory tells us (as seen in Section 2.4) that in leading order, the propagator and the vertex of the gauge-invariant composite operator behave just like the propagator and the vertex of the elementary fields. This is the reason why in the case of the propagator (Section 5.2), we see that the gauge fixed results show a non-physical behaviour, they are below the analytic ground state and are therefore unphysical. In contrast to this behaviour, the results for the propagator of the gauge-invariant composite operator show a much more reasonable behaviour being above the analytic ground state propagator and therefore carrying information from heavier excited states.

The calculated radius is of course not the actual radius of the W-boson, but it gives first estimates and maybe motivates experiments to look into this direction. It is important to note that there are so far no experimental results or theoretical predictions on the radius of the W-boson. Our guess for the radius of the W-boson is of order 10^{-1}fm. Another feature our calculations showed is that the radius of the elementary field is smaller by factor 10^{-1} compared to the radius of the composite state.

Additionaly we could also examine the remaining 13 tensor elements, where one could calculate a radius from. The whole construction is not restricted to tree-level, but gauge invariant perturbation theory suggests to use the tree-level tensor objects in a leading order approximation.

In future computations one should look for lines of constant physics and weakly coupled systems to give more reliable estimates of the radius. Also operators with better overlap with the ground state should be used. From these results one can go further and calculate the triple anomalous gauge coupling. This could in future lead to results showing the difference between perturbation theory and the approach followed in this thesis. However, we expect these differences to be very small since gauge-invariant perturbation theory predicts a leading order behaviour.

Appendix A

Gauge invariant perturbation theory for the 1_3^- channel operator

Given the Operator

$$O^{\bar{a}}_{1_3^-\,\mu}(x) \;=\; \mathrm{tr}\left[\tau_c^{\bar{a}}\frac{X(x)^\dagger}{\sqrt{\det\left(X(x)\right)}}D_\mu(x)\frac{X(x)}{\sqrt{\det\left(X(x)\right)}}\right] \tag{A.1}$$

the first step is to expand the Higgs as $X(x) = v\alpha + \chi(x)$. Here v is a vacuum expectation value, $\alpha \in \mathrm{SU}(2)$ and $\chi(x)$ is the fluctuation field with $\langle\chi(x)\rangle = 0$. Next the determinant $\det\left(X(x)\right) \;=\; \det\left(v\alpha + \chi(x)\right)$ has to be fixed. This is done by

$$\det\left(v\alpha + \chi(x)\right) \;=\; \det\left(v\alpha(\mathbb{1} + \underbrace{\frac{1}{v}\alpha^{-1}\chi(x)}_{\text{small}})\right) \;\approx\; \det\left(v\alpha\right) = \; v^2 \quad . \tag{A.2}$$

Then the operator becomes

$$O^{\bar{a}}_{1_3^-\,\mu}(x) \;\approx\; \mathrm{tr}\left[\tau_c^{\bar{a}}\frac{\left(v\alpha + \chi(x)\right)^\dagger}{v}D_\mu(x)\frac{\left(v\alpha + \chi(x)\right)}{v}\right] \quad . \tag{A.3}$$

The next step is to write the covariant derivative as $D_\mu \;=\; \partial_\mu + igW^a_\mu(x)\tau^a$. Note that generators with barred indices $\tau^{\bar{a}}$ belong to the custodial symmetry and generators with plain indices τ^a belong to the local gauge symmetry. This yields

$$O^{\bar{a}}_{1_3^-\,\mu}(x) \;\approx\; \mathrm{tr}\left[\tau^{\bar{a}}\frac{\left(v\alpha + \chi(x)\right)^\dagger}{v}\left(\partial_\mu + igW^a_\mu(x)\tau^a\right)\frac{\left(v\alpha + \chi(x)\right)}{v}\right] \quad . \tag{A.4}$$

Inserting this into the correlator $\left\langle O^{\bar{a}\,\mu}_{1_3^-}(x)\, O^{\bar{b}\,\nu\,\dagger}_{1_3^-}(y)\right\rangle$ yields

$$\left\langle O^{\bar{a}\,\mu}_{1_3^-}(x)\, O^{\bar{b}\,\nu\,\dagger}_{1_3^-}(y)\right\rangle \;=\; g^2 \mathrm{tr}\left[\tau^{\bar{a}}\alpha^\dagger\tau^a\alpha\right] \mathrm{tr}\left[\tau^{\bar{b}}\alpha^\dagger\tau^b\alpha\right] \left\langle W^a_\mu(x) W^b_\nu(y)\right\rangle + \mathcal{O}(\chi) \quad . \tag{A.5}$$

For the vertex this yields

$$\left\langle O^{\bar{a}\,\mu}_{1_3^-}(x)\, O^{\bar{b}\,\nu}_{1_3^-}(y)\, O^{\bar{c}\,\rho}_{1_3^-}(z)\right\rangle \;=\; -ig^3 \mathrm{tr}\left[\tau^{\bar{a}}\alpha^\dagger\tau^a\alpha\right] \mathrm{tr}\left[\tau^{\bar{b}}\alpha^\dagger\tau^b\alpha\right] \mathrm{tr}\left[\tau^{\bar{c}}\alpha^\dagger\tau^c\alpha\right] \left\langle W^a_\mu(x) W^b_\nu(y) W^b_\nu(z)\right\rangle + \mathcal{O}(\chi) \quad . \tag{A.6}$$

The next step is use an abbreviation from [6]:

$$c^{\bar{a}a} \;=\; \mathrm{tr}\left[\tau^{\bar{a}}\alpha^\dagger\tau^a\alpha\right] \;\in \mathbb{R} \quad , \tag{A.7}$$

to get

$$\left\langle O^{\bar{a}\,\mu}_{1_3^-}(x)\, O^{\bar{b}\,\nu\,\dagger}_{1_3^-}(y)\right\rangle \;=\; g^2 c^{\bar{a}a} c^{\bar{b}b} \left\langle W^a_\mu(x) W^b_\nu(y)\right\rangle + \mathcal{O}(\chi) \quad , \tag{A.8}$$

and

$$\left\langle O^{\bar{a}\,\mu}_{1_3^-}(x)\, O^{\bar{b}\,\nu}_{1_3^-}(y)\, O^{\bar{c}\,\rho}_{1_3^-}(z)\right\rangle \;=\; -ig^3 c^{\bar{a}a} c^{\bar{b}b} c^{\bar{c}c} \left\langle W^a_\mu(x) W^b_\nu(y) W^b_\nu(z)\right\rangle + \mathcal{O}(\chi) \quad . \tag{A.9}$$

Now one can make the gauge choice $\alpha = \mathbb{1}$, then $c^{\bar{a}a} = \frac{1}{2}\delta^{\bar{a}a}$.

Appendix B

Analytic results for the vertex tensor components

B.1 Definitions

Here the decomposition of the propagators and the denominator is shown in detail, therefore his whole section is linked to the sections 2.5.2 and 4.3. The propagator $D^{\bar{a}\bar{b}}_{\mu\nu}$ can be decomposed into its transverse D_{T} and longitudinal D_{L} components as follows

$$D^{\bar{a}\bar{b}}_{\mu\nu}(p) = \delta^{\bar{a}\bar{b}}\Big(T_{\mu\nu}(p)D_{\mathrm{T}}(p) + L_{\mu\nu}(p)D_{\mathrm{L}}(p)\Big) \ , \tag{B.1}$$

where we have used that the propagator is diagonal in the adjoint indices, and

$$T_{\mu\nu}(p) = \delta_{\mu\nu} - \frac{p_\mu p_\nu}{p^2} \ , \ L_{\mu\nu}(p) = \frac{p_\mu p_\nu}{p^2} \ , \tag{B.2}$$

are the transverse and longitudinal projectors, respectively.

The tree-level (non-lattice-improved) three-gluon vertex for SU(2) is given by

$$\Gamma^{\bar{a}\bar{b}\bar{c}}_{\mu\nu\rho}(p,q,k) = -\mathrm{i}g\epsilon^{\bar{a}\bar{b}\bar{c}}\Big[\big(q-k\big)_\mu\delta_{\nu\rho} + \big(k-p\big)_\nu\delta_{\mu\rho} + \big(p-q\big)_\rho\delta_{\mu\nu}\Big] \ , \tag{B.3}$$

where $k = -p - q$ due to momentum conservation. Further, it can bee shown that

$$\Gamma^2(p,q,k) = \Gamma^{\bar{a}\bar{b}\bar{c}}_{\mu\nu\rho}(p,q,k)\Gamma^{\bar{a}\bar{b}\bar{c}}_{\mu\nu\rho}(p,q,k) = -108g^2\big(p\cdot q + p^2 + q^2\big) \ . \tag{B.4}$$

It's necessary to calculate the denominator of a certain ratio ((2.17), (2.18) and (2.19)), which is the form factor from which the radius of the vector triplet bound state is

obtained. This denominator is given by

$$\mathcal{D}(p,q,k) = \Gamma^{\bar{a}\bar{b}\bar{c}}_{\mu\nu\rho}(p,q,k)\, D^{\bar{a}\bar{d}}_{\mu\lambda}(p)\, D^{\bar{b}\bar{e}}_{\nu\sigma}(q)\, D^{\bar{c}\bar{f}}_{\rho\omega}(k)\, \Gamma^{\bar{d}\bar{e}\bar{f}}_{\lambda\sigma\omega}(p,q,k)\ . \tag{B.5}$$

Using the previous definitions, one finds

$$\begin{aligned}
\mathcal{D}(p,q,k) =& \Gamma^{\bar{a}\bar{b}\bar{c}}_{\mu\nu\rho}(p,q,k)\delta^{\bar{a}\bar{d}}\delta^{\bar{b}\bar{e}}\delta^{\bar{c}\bar{f}}\Gamma^{\bar{d}\bar{e}\bar{f}}_{\lambda\sigma\omega}(p,q,k)\\
&\times\big[\ T_{\mu\lambda}(p)\, T_{\nu\sigma}(q)\, T_{\rho\omega}(k)\, D_{\mathrm{T}}(p)\, D_{\mathrm{T}}(q)\, D_{\mathrm{T}}(k)\\
&+T_{\mu\lambda}(p)\, T_{\nu\sigma}(q)\, L_{\rho\omega}(k)\, D_{\mathrm{T}}(p)\, D_{\mathrm{T}}(q)\, D_{\mathrm{L}}(k)\\
&+T_{\mu\lambda}(p)\, L_{\nu\sigma}(q)\, T_{\rho\omega}(k)\, D_{\mathrm{T}}(p)\, D_{\mathrm{L}}(q)\, D_{\mathrm{T}}(k)\\
&+T_{\mu\lambda}(p)\, L_{\nu\sigma}(q)\, L_{\rho\omega}(k)\, D_{\mathrm{T}}(p)\, D_{\mathrm{L}}(q)\, D_{\mathrm{L}}(k)\\
&+L_{\mu\lambda}(p)\, T_{\nu\sigma}(q)\, T_{\rho\omega}(k)\, D_{\mathrm{L}}(p)\, D_{\mathrm{T}}(q)\, D_{\mathrm{T}}(k)\\
&+L_{\mu\lambda}(p)\, T_{\nu\sigma}(q)\, L_{\rho\omega}(k)\, D_{\mathrm{L}}(p)\, D_{\mathrm{T}}(q)\, D_{\mathrm{L}}(k)\\
&+L_{\mu\lambda}(p)\, L_{\nu\sigma}(q)\, T_{\rho\omega}(k)\, D_{\mathrm{L}}(p)\, D_{\mathrm{L}}(q)\, D_{\mathrm{T}}(k)\\
&+L_{\mu\lambda}(p)\, L_{\nu\sigma}(q)\, L_{\rho\omega}(k)\, D_{\mathrm{L}}(p)\, D_{\mathrm{L}}(q)\, D_{\mathrm{L}}(k)\big]\ .
\end{aligned} \tag{B.6}$$

B.2 Contractions of the denominator

The contractions of the color and Lorentz indices can be done analytically. One obtains the following results for the different classes $\Gamma T^n L^m \Gamma$, $n+m=3$ (the indices of the following functions refer to the lines of Equation (B.6)):

- $\Gamma T^3 \Gamma$:

$$\begin{aligned}
\left(\Gamma T^3 \Gamma\right)_1(p,q,k) =& \frac{24g^2}{p^2q^2k^2}\left((p\cdot q)^2 - p^2q^2\right)\\
&\times\left((p\cdot q)^2 + 6(p\cdot q)(p^2+q^2) + 8p^2q^2 + 3p^4 + 3q^4\right)
\end{aligned} \tag{B.7}$$

- $\Gamma T^2 L \Gamma$:

$$\begin{aligned}
\left(\Gamma T^2 L \Gamma\right)_2(p,q,k) &= -\frac{6g^2}{p^2q^2k^2}\left(p^2-q^2\right)^2\left((p\cdot q)^2 + 2p^2q^2\right)\\
\left(\Gamma T^2 L \Gamma\right)_3(p,q,k) &= -\frac{6g^2}{p^2q^2k^2}\left(p^2-k^2\right)^2\left((p\cdot k)^2 + 2p^2k^2\right)\\
\left(\Gamma T^2 L \Gamma\right)_4(p,q,k) &= -\frac{6g^2}{p^2q^2k^2}\left(k^2-q^2\right)^2\left((k\cdot q)^2 + 2k^2q^2\right)
\end{aligned} \tag{B.8}$$

- $\Gamma T L^2 \Gamma$:

$$\begin{aligned}
\left(\Gamma T L^2 \Gamma\right)_5(p,q,k) =& \frac{6g^2}{q^2k^2}\, p^2 \left((p\cdot q)^2 - p^2q^2\right) \\
\left(\Gamma T L^2 \Gamma\right)_6(p,q,k) =& \frac{6g^2}{p^2k^2}\, q^2 \left((p\cdot q)^2 - p^2q^2\right) \\
\left(\Gamma T L^2 \Gamma\right)_7(p,q,k) =& \frac{6g^2}{p^2q^2}\, k^2 \left((p\cdot q)^2 - p^2q^2\right)
\end{aligned} \tag{B.9}$$

- $\Gamma L^3 \Gamma$:

$$\left(\Gamma L^3 \Gamma\right)_8(p,q,k) = 0 \tag{B.10}$$

B.3 Explicit values

Given the following momentum configurations for a lattice with extent L:

$$p = \frac{2\pi}{L}\big(n,-n,0,0\big)\ ,\ q = \frac{2\pi}{L}\big(-n,0,n,0\big)\ ,\ k = \frac{2\pi}{L}\big(0,n,-n,0\big)\ , \tag{B.11}$$

where $n = 0,\ldots,\frac{L}{2}$. Therefore, one obtains the following results ($g^2 = 4/\beta$):

$$\begin{aligned}
\left(\Gamma T^3 \Gamma\right)_1(p,q,k) &= -\frac{4752\pi^2}{L^2\beta} n^2 \\
\left(\Gamma T^2 L \Gamma\right)_{2,3,4}(p,q,k) &= 0 \\
\left(\Gamma T L^2 \Gamma\right)_{5,6,7}(p,q,k) &= -\frac{144\pi^2}{L^2\beta} n^2 \\
\left(\Gamma L^3 \Gamma\right)_8(p,q,k) &= 0 \\
\Gamma^2(p,q,k) &= -\frac{5184\pi^2}{L^2\beta} n^2
\end{aligned} \tag{B.12}$$

In Table B.1 the corresponding numerical values for the case $L = 8$ and $\beta = 2.7984$ are listed for all non-vanishing combinations.

Table B.1: Numerical values of the non-vanishing elements of Equation (B.12), where $L = 8$ and $\beta = 2.7984$.

Contraction	$n=1$	$n=2$	$n=3$	$n=4$
$\left(\Gamma T^3 \Gamma\right)_1$	−261.870	−1047.48	−2356.83	−4189.93
$\left(\Gamma T L^2 \Gamma\right)_{5,6,7}$	−7.93547	−31.7419	−71.4192	−126.967
Γ^2	−285.677	−1142.71	−2570.63	−4570.83

B.4 Lattice improved versions

The lattice improved versions of the projectors in Equation (B.2) are

$$T_{\mu\nu}(p) = \delta_{\mu\nu} - \frac{\sin\left(\frac{p_\mu}{2}\right)\sin\left(\frac{p_\nu}{2}\right)}{\sum\limits_{\rho=1}^{4}\sin^2\left(\frac{p_\rho}{2}\right)}\ ,\ L_{\mu\nu}(p) = \frac{\sin\left(\frac{p_\mu}{2}\right)\sin\left(\frac{p_\nu}{2}\right)}{\sum\limits_{\rho=1}^{4}\sin^2\left(\frac{p_\rho}{2}\right)} \tag{B.13}$$

where $p_\mu = \frac{2\pi}{L}n_\mu$, with $n_\mu = 0, 1, \ldots, L/2$. The vertex (B.3) becomes

$$\begin{aligned}\Gamma^{\bar{a}\bar{b}\bar{c}}_{\mu\nu\rho}(p,q,k) = -\mathrm{i}g\epsilon^{\bar{a}\bar{b}\bar{c}}\,\mathrm{e}^{\frac{\mathrm{i}}{2}(p_\mu+q_\nu+k_\rho)}\Bigg[&2\,\sin\left(\frac{q_\mu-k_\mu}{2}\right)\delta_{\nu\rho}\,\cos\left(\frac{p_\nu}{2}\right)\\ &+2\,\sin\left(\frac{k_\nu-p_\nu}{2}\right)\delta_{\mu\rho}\,\cos\left(\frac{q_\rho}{2}\right)+2\,\sin\left(\frac{p_\rho-q_\rho}{2}\right)\delta_{\mu\nu}\,\cos\left(\frac{k_\mu}{2}\right)\Bigg]\,.\end{aligned} \tag{B.14}$$

Using the momenta defined in Equation (B.11) yields for the lattice improved versions of Equation (B.12):

$$\begin{aligned}
\left(\Gamma T^3\Gamma\right)_1(p,q,k) &= -\frac{144}{\beta}\left[18+13\,\cos\left(\frac{2\pi}{L}n\right)+2\,\cos\left(\frac{4\pi}{L}n\right)\right]\sin^2\left(\frac{\pi}{L}n\right)\\
\left(\Gamma T^2L\Gamma\right)_{2,3,4}(p,q,k) &= 0\\
\left(\Gamma TL^2\Gamma\right)_{5,6,7}(p,q,k) &= -\frac{48}{\beta}\left[2+\cos\left(\frac{2\pi}{L}n\right)\right]\sin^2\left(\frac{\pi}{L}n\right)\\
\left(\Gamma L^3\Gamma\right)_8(p,q,k) &= 0\\
\Gamma^2(p,q,k) &= -\frac{288}{\beta}\left[10+7\,\cos\left(\frac{2\pi}{L}n\right)+\cos\left(\frac{4\pi}{L}n\right)\right]\sin^2\left(\frac{\pi}{L}n\right)
\end{aligned} \tag{B.15}$$

In Table B.2 again the corresponding numerical values for the case $L = 8$ and $\beta = 2.7984$ are listed for all non-vanishing combinations.

TABLE B.2: Numerical values of the non-vanishing elements of Equation (B.15), where $L = 8$ and $\beta = 2.7984$.

Contraction	$n=1$	$n=2$	$n=3$	$n=4$
$\left(\Gamma T^3\Gamma\right)_1$	−204.918	−411.664	−386.849	−360.206
$\left(\Gamma TL^2\Gamma\right)_{5,6,7}$	−6.80011	−17.1527	−18.9289	−17.1527
Γ^2	−225.318	−463.122	−443.636	−411.664

B.5 Lattice improved tensor components of the numerator

One can also get analytic results for the numerator of the ratio mentioned above, which is given by

$$C_3(p,q,k) \;=\; \Gamma^{\bar{a}\bar{b}\bar{c}}_{\mu\nu\rho}(p,q,k)\,\left\langle O^{\bar{a}}_{\mu\,1_3^-}(p)\,O^{\bar{b}}_{\nu\,1_3^-}(q)\,O^{\bar{c}}_{\rho\,1_3^-}(k)\right\rangle \quad . \tag{B.16}$$

Again, the operator $O^{\bar{a}}_{\mu\,1_3^-}(p)$ has transverse and longitudinal parts, i.e.,

$$O^{\bar{a}}_{\mu\,1_3^-}(p) = T_{\mu\nu}(p)\,O^{\bar{a}}_{\nu\,T}(p) + L_{\mu\nu}(p)\,O^{\bar{a}}_{\nu\,L}(p)\;. \tag{B.17}$$

Therefore, similar terms appear in Equation (B.16) as in Equation (B.6). The only non-vanishing tensor structures have the form

$$\Gamma^{\bar{a}\bar{b}\bar{c}}_{\mu'\nu'\rho'}(p,q,k)\,T_{\mu'\mu}(p)\,T_{\nu'\nu}(q)\,T_{\rho'\rho}(k) \quad \text{and} \quad \Gamma^{\bar{a}\bar{b}\bar{c}}_{\mu'\nu'\rho'}(p,q,k)\,T_{\mu'\mu}(p)\,L_{\nu'\nu}(q)\,L_{\rho'\rho}(k)\;, \tag{B.18}$$

including permutations of the momenta. The remaining combinations are identically zero. Here the lattice improved versions of the vertex and the projectors as defined in the last section and the lattice momenta (B.11) are considered. One defines the following objects:

$$\begin{aligned} P^{\Gamma T^3}_{\mu\nu\rho}(n) &= \epsilon^{\bar{a}\bar{b}\bar{c}}\,\Gamma^{\bar{a}\bar{b}\bar{c}}_{\mu'\nu'\rho'}(p,q,k)\,T_{\mu'\mu}(p)\,T_{\nu'\nu}(q)\,T_{\rho'\rho}(k)\;,\\ P^{\Gamma TL^2}_{\mu\nu\rho}(n) &= \epsilon^{\bar{a}\bar{b}\bar{c}}\,\Gamma^{\bar{a}\bar{b}\bar{c}}_{\mu'\nu'\rho'}(p,q,k)\,T_{\mu'\mu}(p)\,L_{\nu'\nu}(q)\,L_{\rho'\rho}(k)\;. \end{aligned} \tag{B.19}$$

In Table B.3 we list the non-vanishing components of these tensors.

Table B.3: Non-vanishing components of the tensors defined in Equation (B.19) for the lattice improved vertex and projectors, where $n = 0, 1, \ldots, L/2$.

$P^{\Gamma\,T^3}_{\mu\nu\rho}(n)$	(μ,ν,ρ)	$P^{\Gamma\,TL^3}_{\mu\nu\rho}(n)$	(μ,ν,ρ)
$\mathrm{i}\,\frac{6}{\sqrt{\beta}}\,\sin\left(\frac{2\pi}{L}n\right)$	$(1,1,1)$, $(1,2,2)$, $(1,2,3)$, $(1,3,1)$		
	$(2,1,1)$, $(2,2,2)$, $(2,2,3)$, $(2,3,1)$	$\mathrm{i}\,\frac{6}{\sqrt{\beta}}\,\sin\left(\frac{2\pi}{L}n\right)$	$(3,1,3)$, $(3,3,2)$
	$(3,1,2)$, $(3,1,3)$, $(3,3,2)$, $(3,3,3)$		
$\mathrm{i}\,\frac{18}{\sqrt{\beta}}\,\sin\left(\frac{\pi}{L}n\right)$	$(1,1,2)$, $(1,1,3)$, $(1,3,2)$, $(1,3,3)$	$-\mathrm{i}\,\frac{6}{\sqrt{\beta}}\,\sin\left(\frac{2\pi}{L}n\right)$	$(3,1,2)$, $(3,3,3)$
	$(2,1,2)$, $(2,1,3)$, $(2,3,2)$, $(2,3,3)$		
$-\mathrm{i}\,\frac{24}{\sqrt{\beta}}\,\sin\left(\frac{2\pi}{L}n\right)\,\cos\left(\frac{\pi}{L}n\right)$	$(1,2,1)$, $(2,2,1)$, $(3,1,1)$, $(3,2,2)$	$\mathrm{i}\,\frac{6}{\sqrt{\beta}}\,\sin\left(\frac{\pi}{L}n\right)$	$(1,1,2)$, $(1,3,3)$, $(2,1,2)$, $(2,3,3)$
	$(3,2,3)$, $(3,3,1)$		
$\mathrm{i}\,\frac{24}{\sqrt{\beta}}\,\sin\left(\frac{\pi}{L}n\right)$	$(1,4,4)$, $(2,4,4)$, $(4,1,4)$, $(4,3,4)$	$-\mathrm{i}\,\frac{6}{\sqrt{\beta}}\,\sin\left(\frac{\pi}{L}n\right)$	$(1,1,3)$, $(1,3,2)$, $(2,1,3)$, $(2,3,2)$
	$(4,4,2)$, $(4,4,3)$		
$-\mathrm{i}\,\frac{24}{\sqrt{\beta}}\,\sin\left(\frac{2\pi}{L}n\right)$	$(3,4,4)$, $(4,2,4)$, $(4,4,1)$		

Appendix C

Plots for the propagator

C.1 Plots for each set of parameters seperately

In all plots the lattice artifacts were reduced using the procedure discussed in Chapter 5. In Chapter 5 we showed plots with a logarithmic scale. Here we show plots with a linear scale, this is due to a better depiction for this amount of plots.

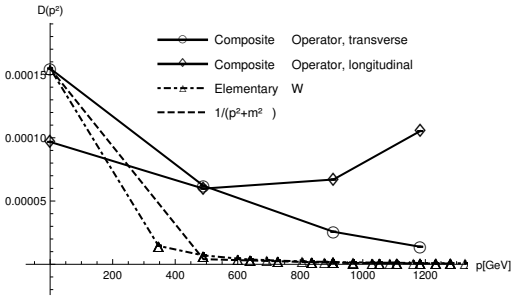

FIGURE C.1: Plot for the propagator for parameter set A for lattice size $L = 8$

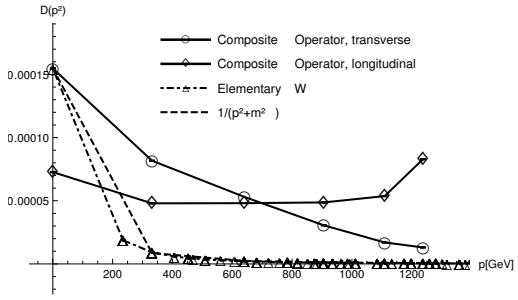

FIGURE C.2: Plot for the propagator for parameter set A for lattice size $L = 12$

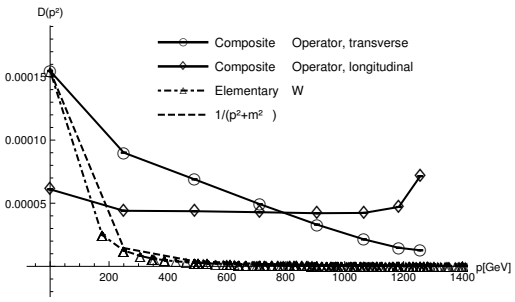

FIGURE C.3: Plot for the propagator for parameter set A for lattice size $L = 16$

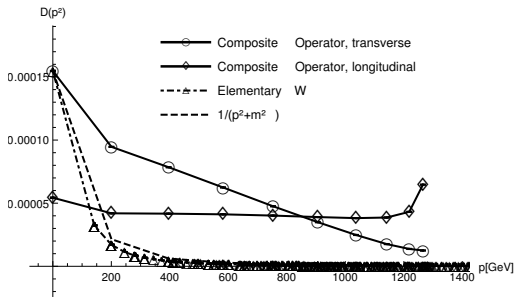

FIGURE C.4: Plot for the propagator for parameter set A for lattice size $L = 20$

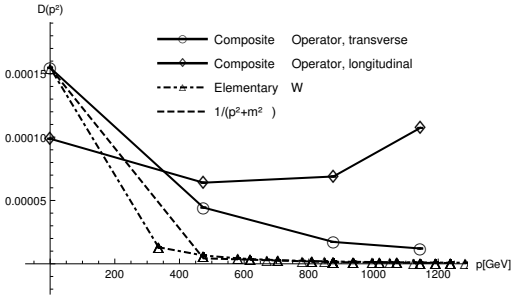

FIGURE C.5: Plot for the propagator for parameter set B for lattice size $L = 8$

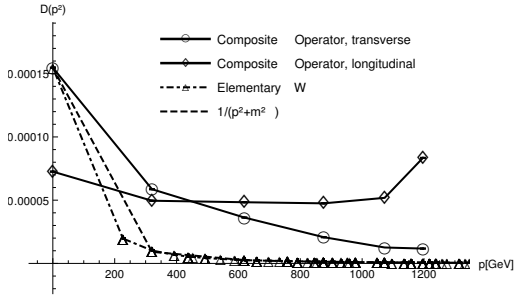

FIGURE C.6: Plot for the propagator for parameter set B for lattice size $L = 12$

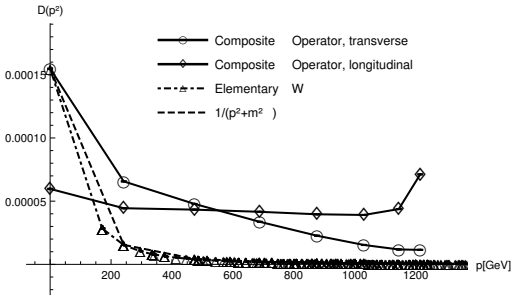

FIGURE C.7: Plot for the propagator for parameter set B for lattice size $L = 16$

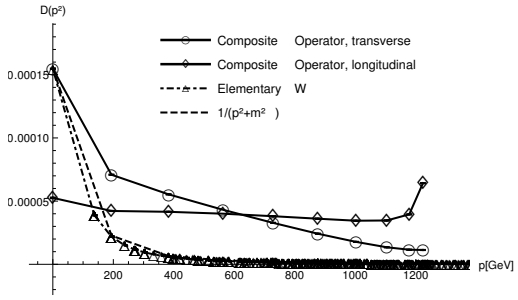

FIGURE C.8: Plot for the propagator for parameter set B for lattice size $L = 20$

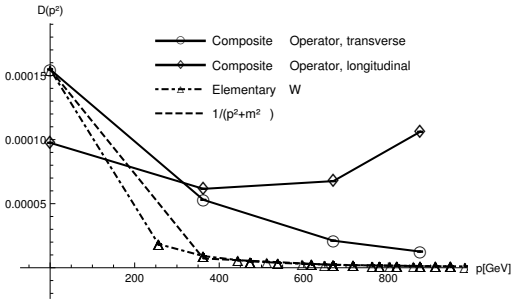

FIGURE C.9: Plot for the propagator for parameter set C for lattice size $L = 8$

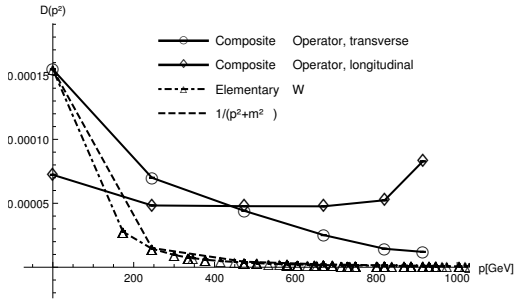

FIGURE C.10: Plot for the propagator for parameter set C for lattice size $L = 12$

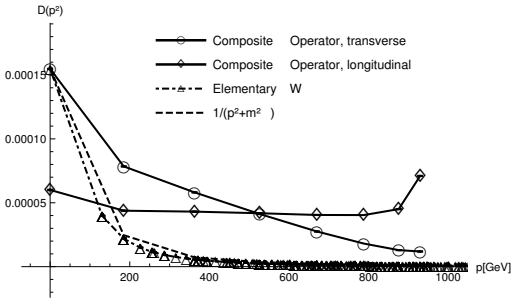

FIGURE C.11: Plot for the propagator for parameter set C for lattice size $L = 16$

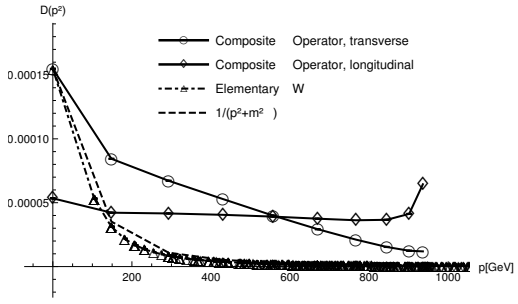

FIGURE C.12: Plot for the propagator for parameter set C for lattice size $L = 20$

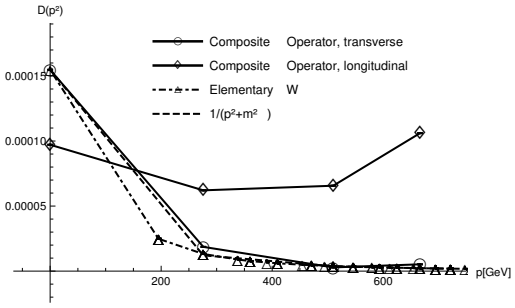

FIGURE C.13: Plot for the propagator for parameter set D for lattice size $L = 8$

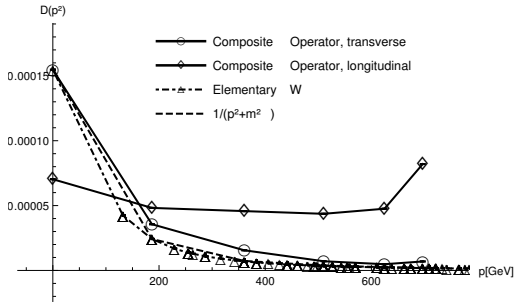

FIGURE C.14: Plot for the propagator for parameter set D for lattice size $L = 12$

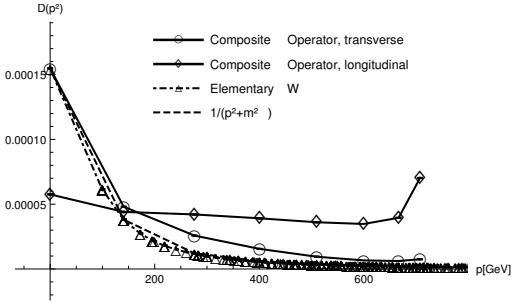

FIGURE C.15: Plot for the propagator for parameter set D for lattice size $L = 16$

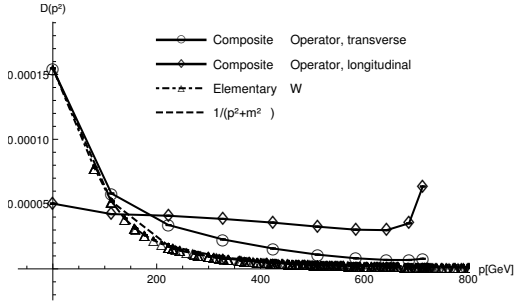

FIGURE C.16: Plot for the propagator for parameter set D for lattice size $L = 20$

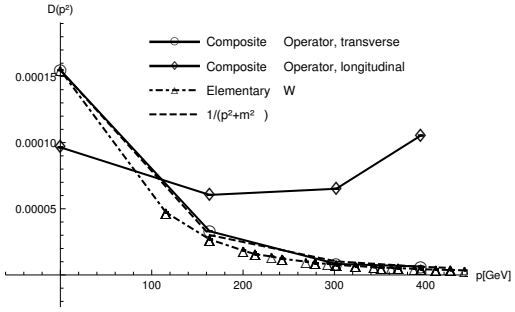

FIGURE C.17: Plot for the propagator for parameter set E for lattice size $L = 8$

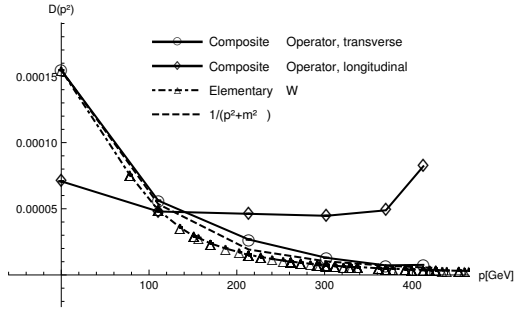

FIGURE C.18: Plot for the propagator for parameter set E for lattice size $L = 12$

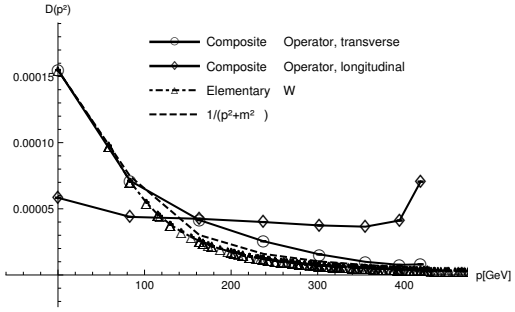

FIGURE C.19: Plot for the propagator for parameter set E for lattice size $L = 16$

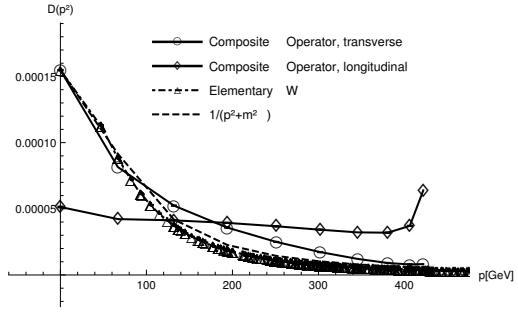

FIGURE C.20: Plot for the propagator for parameter set E for lattice size $L = 20$

C.2 Plots for all sets of parameters for fixed lattice sizes

In all plots the lattice artifacts were reduced using the procedure discussed in Chapter 5. In Chapter 5 we showed plots with a logarithmic scale. Here we show plots with a linear scale, this is due to a better depiction for this amount of plots.

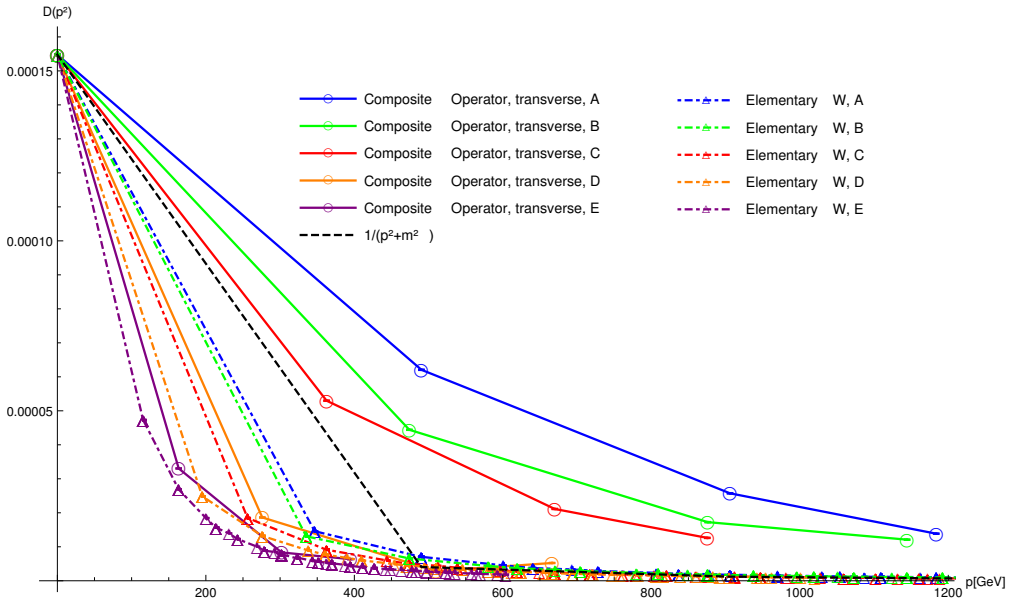

FIGURE C.21: Plot for the transverse parts for all sets of parameters for lattice size $L = 8$. Here the lattice artifacts were removed using the discussed procedure.

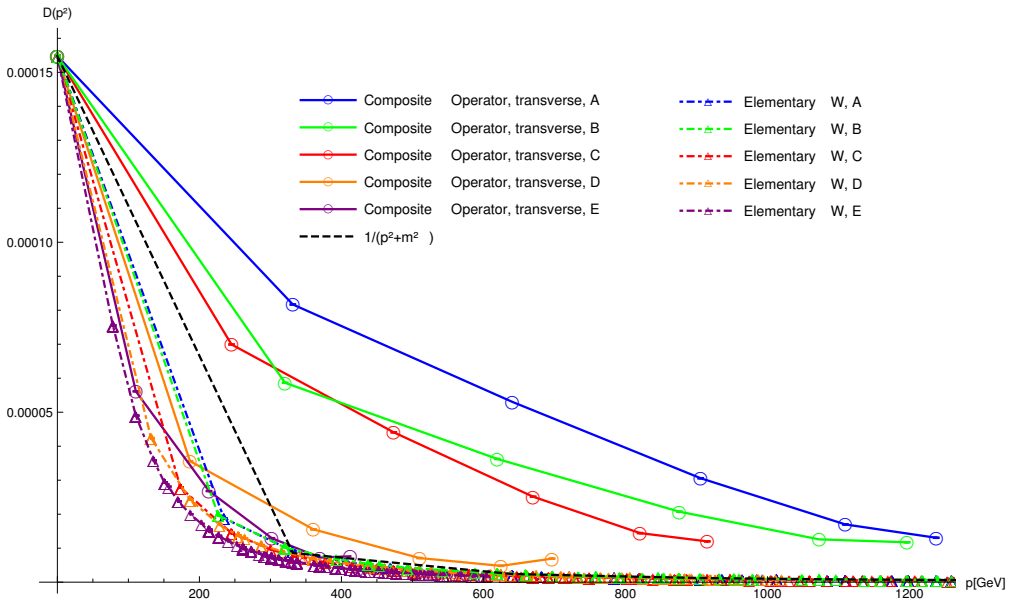

FIGURE C.22: Plot for the transverse parts for all sets of parameters for lattice size $L = 12$. Here the lattice artifacts were removed using the discussed procedure.

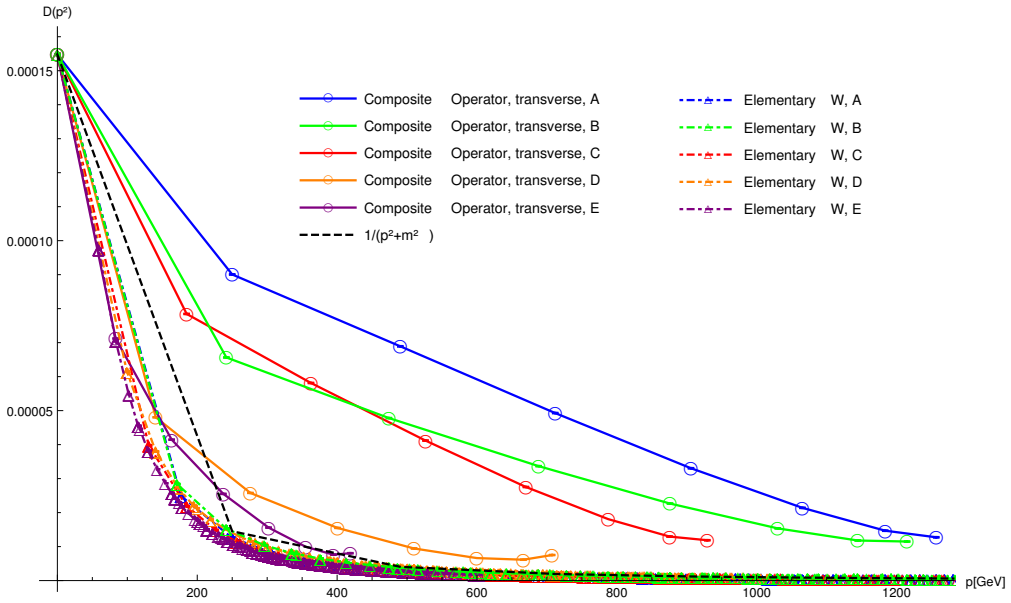

FIGURE C.23: Plot for the transverse parts for all sets of parameters for lattice size $L = 16$. Here the lattice artifacts were removed using the discussed procedure.

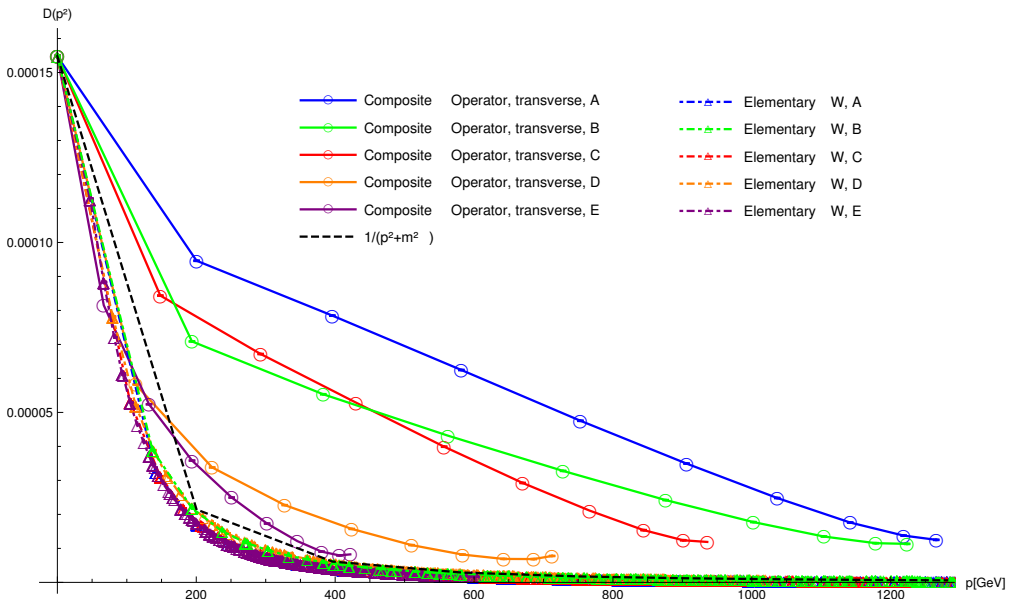

FIGURE C.24: Plot for the transverse parts for all sets of parameters for lattice size $L = 20$. Here the lattice artifacts were removed using the discussed procedure.

Appendix D

Plots for the ratio

D.1 Plots for the different ratios

The following plots are the results for the composite particle for the different ratios (2.20), (2.21) and (2.22), compared with the elementary ratio. The comparison for the transverse-only ratio (2.21) and for the ratio with equal momenta configuration (2.20) was done with the same elementary ratio, the one for a configuration of equal momenta. For the configuration with one momentum vanishing we calculated the corresponding elementary ratio with one momentum vanishing [9].

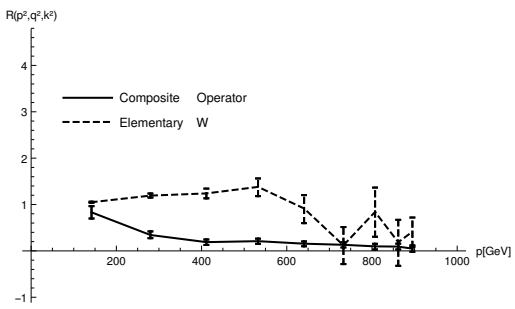

FIGURE D.1: Plot of the ratio for equal momenta for parameter set A for lattice size $L = 20$. (2.20)

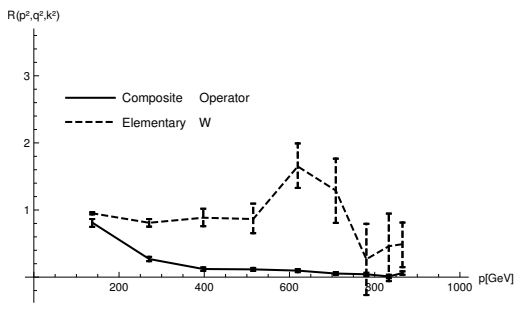

FIGURE D.2: Plot of the ratio for equal momenta for parameter set B for lattice size $L = 20$. (2.20)

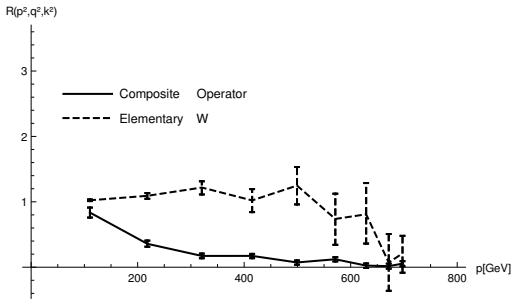

FIGURE D.3: Plot of the ratio for equal momenta for parameter set C for lattice size $L = 20$. (2.20)

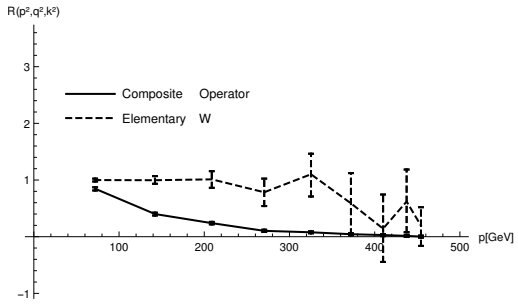

FIGURE D.4: Plot of the ratio for equal momenta for parameter set D for lattice size $L = 20$. (2.20)

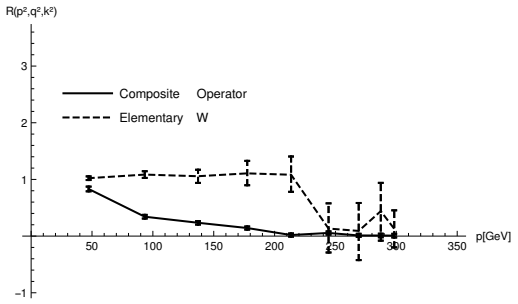

FIGURE D.5: Plot of the ratio for equal momenta for parameter set E for lattice size $L = 20$. (2.20)

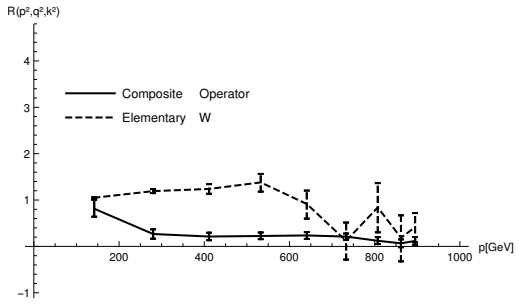

FIGURE D.6: Plot of the ratio for the transverse-only ratio for parameter set A for lattice size $L = 20$. (2.21)

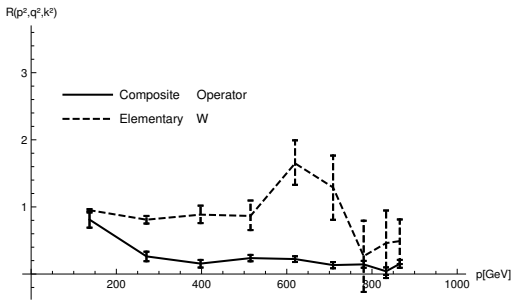

FIGURE D.7: Plot of the ratio for the transverse-only ratio for parameter set B for lattice size $L = 20$. (2.21)

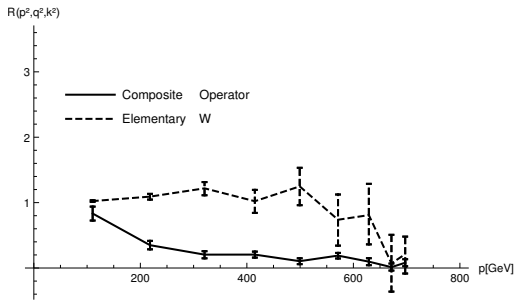

FIGURE D.8: Plot of the ratio for the transverse-only ratio for parameter set C for lattice size $L = 20$. (2.21)

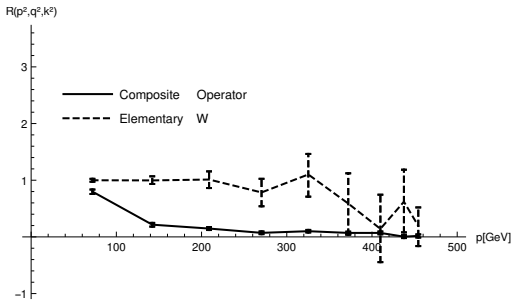

FIGURE D.9: Plot of the ratio for the transverse-only ratio for parameter set D for lattice size $L = 20$. (2.21)

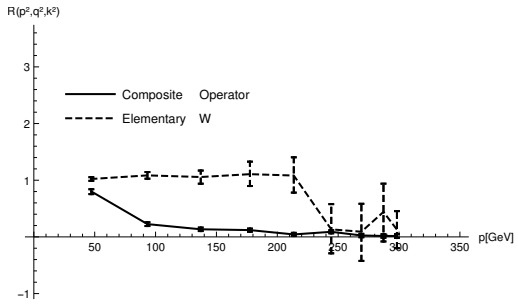

FIGURE D.10: Plot of the ratio for the transverse-only ratio for parameter set E for lattice size $L = 20$. (2.21)

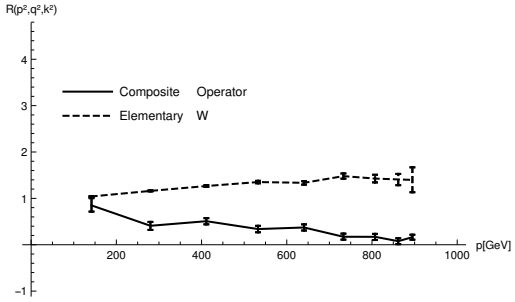

FIGURE D.11: Plot of the ratio for the transverse-only ratio for parameter set A for lattice size $L = 20$. (2.22)

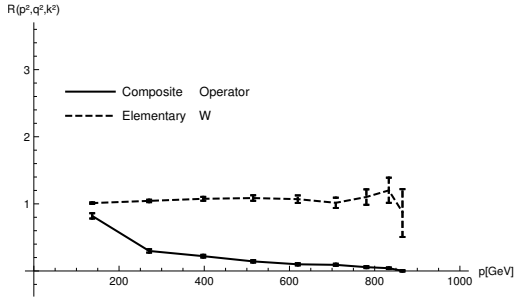

FIGURE D.12: Plot of the ratio for the transverse-only ratio for parameter set C for lattice size $L = 20$. (2.22)

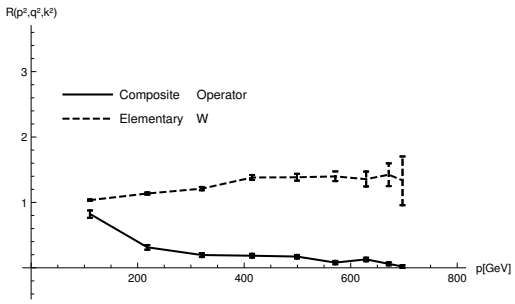

FIGURE D.13: Plot of the ratio for the transverse-only ratio for parameter set D for lattice size $L = 20$. (2.22)

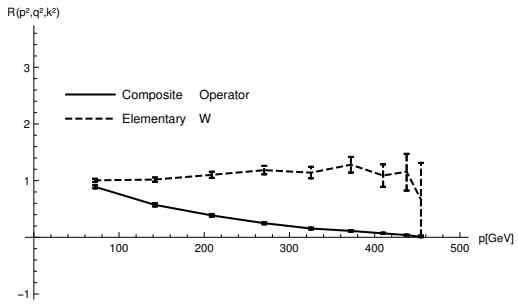

FIGURE D.14: Plot of the ratio for the transverse-only ratio for parameter set E for lattice size $L = 20$. (2.22)

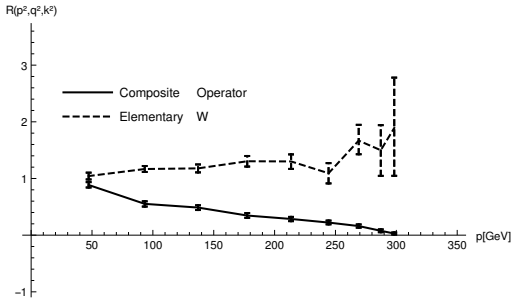

FIGURE D.15: Plot of the ratio for the transverse-only ratio for parameter set E for lattice size $L = 20$. (2.22)

D.2 Lattice-improved ratios

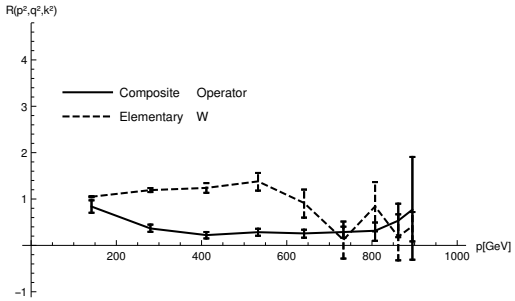

FIGURE D.16: Plot of the ratio for the improvement (5.7) for parameter set A and lattice size $L = 20$. Equal momentum configuration (2.21)

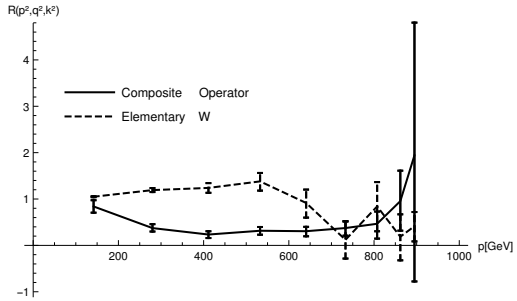

FIGURE D.17: Plot of the ratio for the improvement (5.8) for parameter set A and lattice size $L = 20$. Equal momentum configuration (2.21)

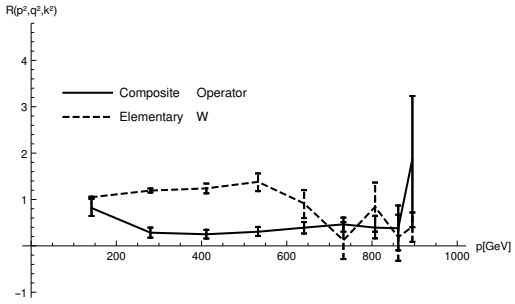

FIGURE D.18: Plot of the ratio for the improvement (5.7) for parameter set A and lattice size $L = 20$. Transverse-only ratio (2.22)

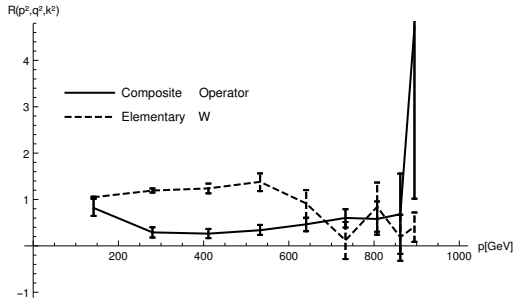

FIGURE D.19: Plot of the ratio for the improvement (5.8) for parameter set A and lattice size $L = 20$. Transverse-only ratio (2.22)

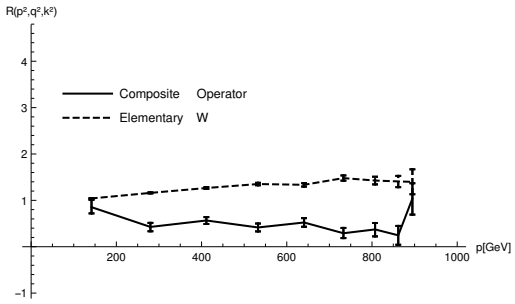

FIGURE D.20: Plot of the ratio for the improvement (5.5) for parameter set A and lattice size $L = 20$. One momentum vanishing (2.22)

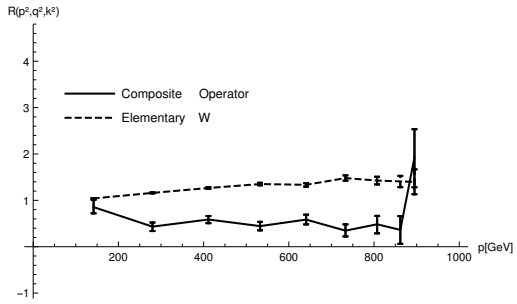

FIGURE D.21: Plot of the ratio for the improvement (5.6) for parameter set A and lattice size $L = 20$. One momentum vanishing (2.22)

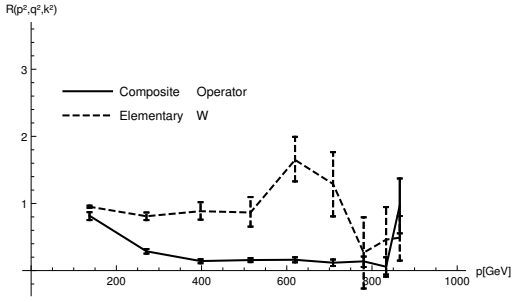

FIGURE D.22: Plot of the ratio for the improvement (5.7) for parameter set B and lattice size $L = 20$. Equal momentum configuration (2.21)

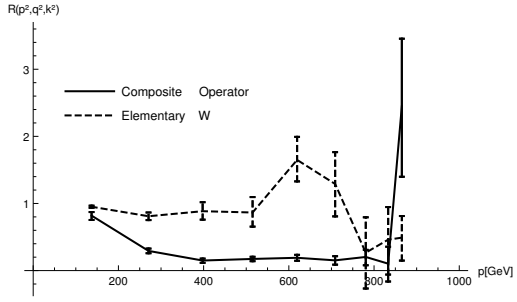

FIGURE D.23: Plot of the ratio for the improvement (5.8) for parameter set B and lattice size $L = 20$. Equal momentum configuration (2.21)

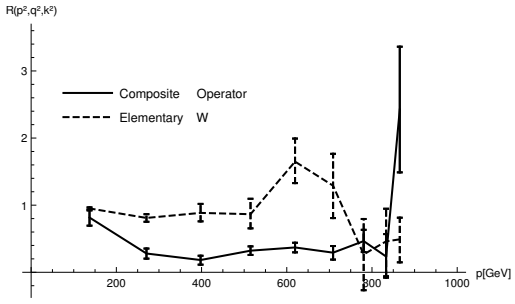

FIGURE D.24: Plot of the ratio for the improvement (5.7) for parameter set B and lattice size $L = 20$. Transverse-only ratio (2.22)

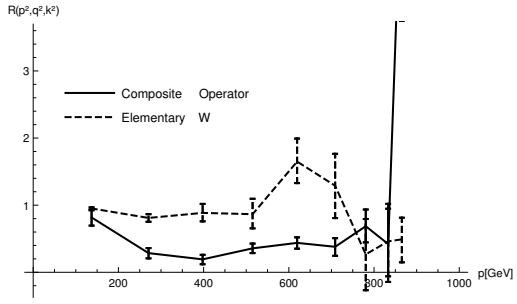

FIGURE D.25: Plot of the ratio for the improvement (5.8) for parameter set B and lattice size $L = 20$. Transverse-only ratio (2.22)

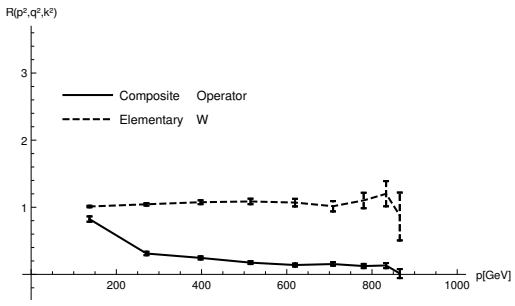

FIGURE D.26: Plot of the ratio for the improvement (5.5) for parameter set B and lattice size $L = 20$. One momentum vanishing (2.22)

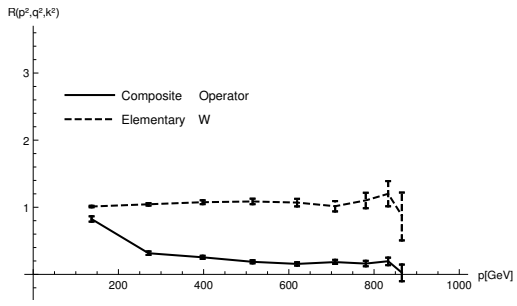

FIGURE D.27: Plot of the ratio for the improvement (5.6) for parameter set B and lattice size $L = 20$. One momentum vanishing (2.22)

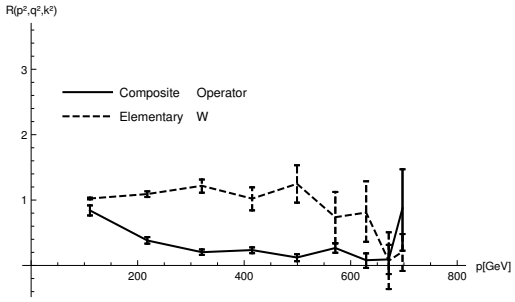

FIGURE D.28: Plot of the ratio for the improvement (5.7) for parameter set C and lattice size $L = 20$. Equal momentum configuration (2.21)

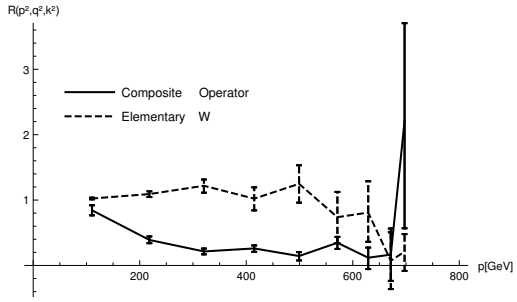

FIGURE D.29: Plot of the ratio for the improvement (5.8) for parameter set C and lattice size $L = 20$. Equal momentum configuration (2.21)

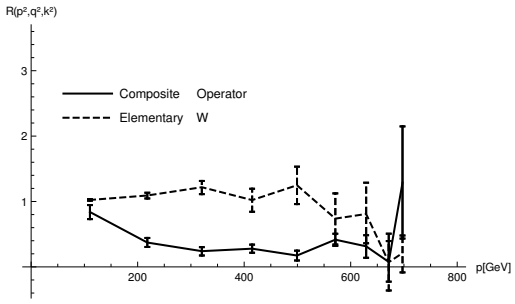

FIGURE D.30: Plot of the ratio for the improvement (5.7) for parameter set C and lattice size $L = 20$. Transverse-only ratio (2.22)

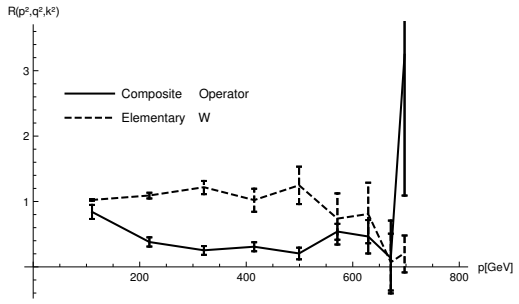

FIGURE D.31: Plot of the ratio for the improvement (5.8) for parameter set C and lattice size $L = 20$. Transverse-only ratio (2.22)

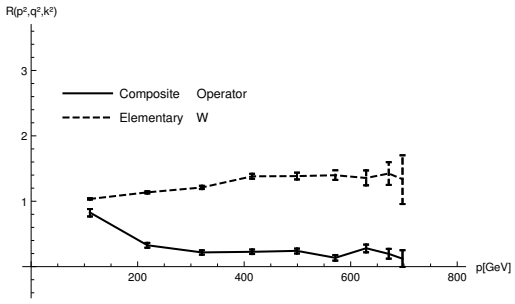

FIGURE D.32: Plot of the ratio for the improvement (5.5) for parameter set C and lattice size $L = 20$. One momentum vanishing (2.22)

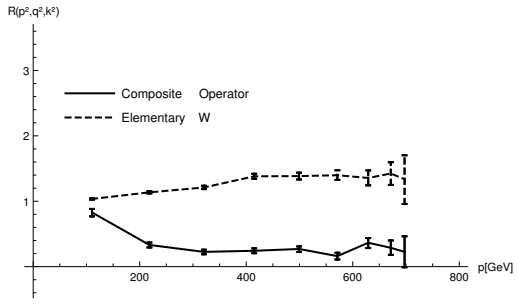

FIGURE D.33: Plot of the ratio for the improvement (5.6) for parameter set C and lattice size $L = 20$. One momentum vanishing (2.22)

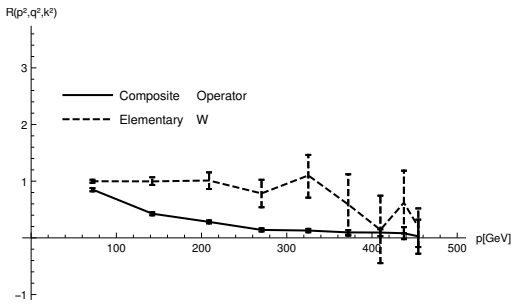

FIGURE D.34: Plot of the ratio for the improvement (5.7) for parameter set D and lattice size $L = 20$. Equal momentum configuration (2.21)

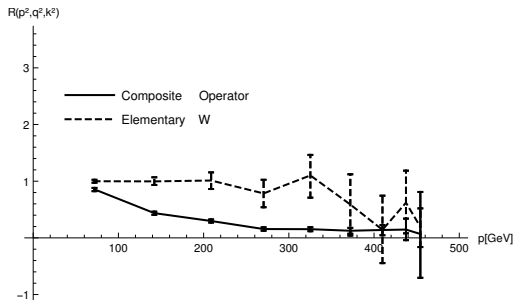

FIGURE D.35: Plot of the ratio for the improvement (5.8) for parameter set D and lattice size $L = 20$. Equal momentum configuration (2.21)

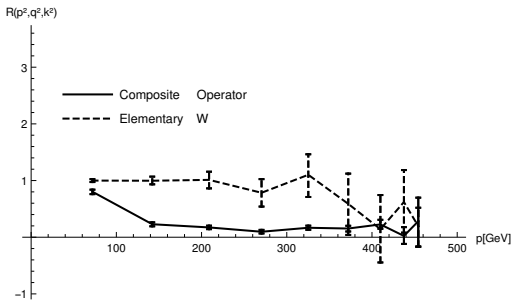

FIGURE D.36: Plot of the ratio for the improvement (5.7) for parameter set D and lattice size $L = 20$. Transverse-only ratio (2.22)

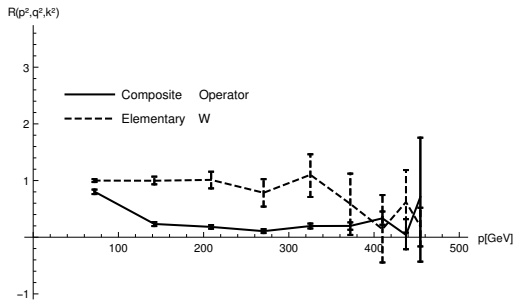

FIGURE D.37: Plot of the ratio for the improvement (5.8) for parameter set D and lattice size $L = 20$. Transverse-only ratio (2.22)

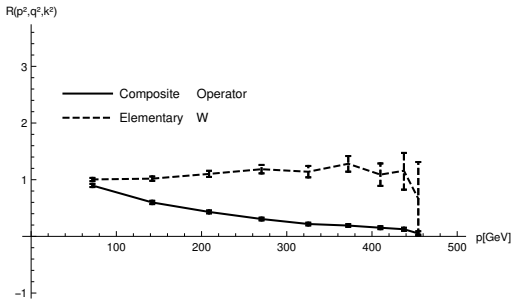

FIGURE D.38: Plot of the ratio for the improvement (5.5) for parameter set D and lattice size $L = 20$. One momentum vanishing (2.22)

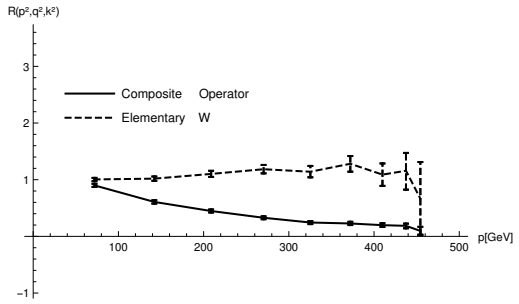

FIGURE D.39: Plot of the ratio for the improvement (5.6) for parameter set D and lattice size $L = 20$. One momentum vanishing (2.22)

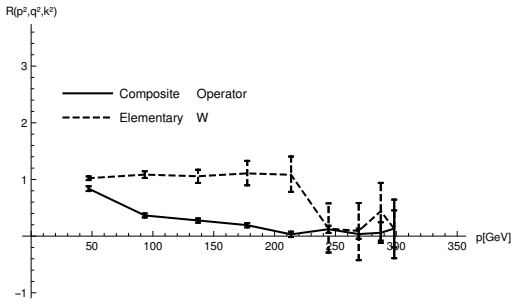

FIGURE D.40: Plot of the ratio for the improvement (5.7) for parameter set E and lattice size $L = 20$. Equal momentum configuration (2.21)

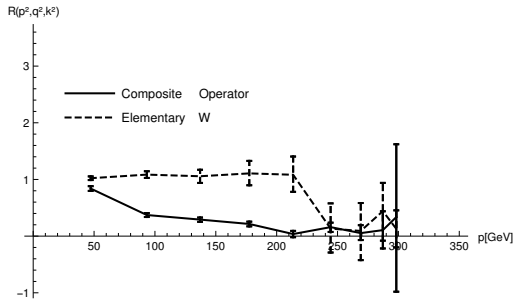

FIGURE D.41: Plot of the ratio for the improvement (5.8) for parameter set E and lattice size $L = 20$. Equal momentum configuration (2.21)

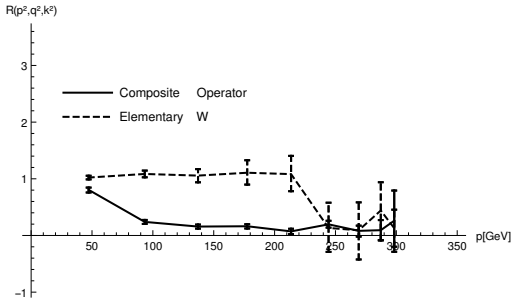

FIGURE D.42: Plot of the ratio for the improvement (5.7) for parameter set E and lattice size $L = 20$. Transverse-only ratio (2.22)

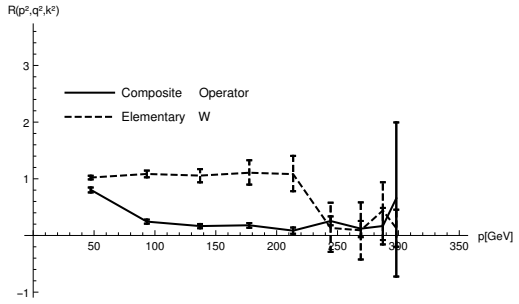

FIGURE D.43: Plot of the ratio for the improvement (5.8) for parameter set E and lattice size $L = 20$. Transverse-only ratio (2.22)

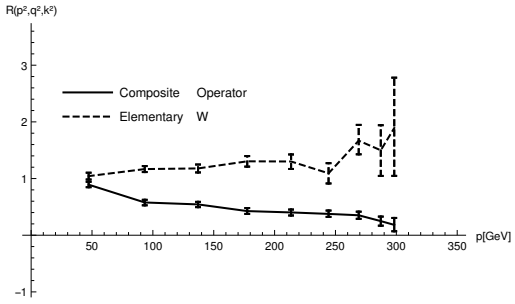

FIGURE D.44: Plot of the ratio for the improvement (5.5) for parameter set E and lattice size $L = 20$. One momentum vanishing (2.22)

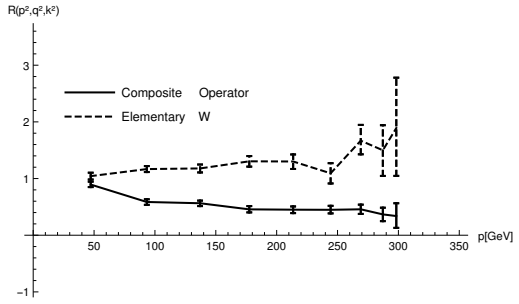

FIGURE D.45: Plot of the ratio for the improvement (5.6) for parameter set E and lattice size $L = 20$. One momentum vanishing (2.22)

D.3 Plots for a fixed lattice size

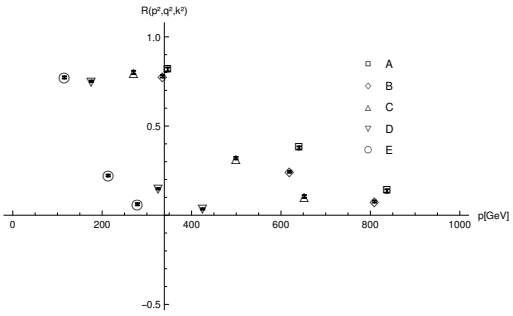

FIGURE D.46: Plot of the ratio for all sets of parameters and lattice size $L = 8$. Equal momentum configuration (2.20). Composite particle.

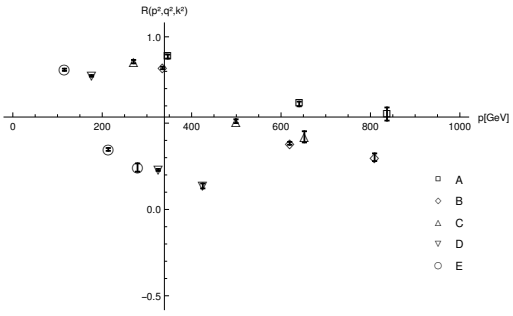

FIGURE D.47: Plot of the ratio for the improvement (5.7) for all sets of parameters and lattice size $L = 8$. Equal momentum configuration (2.20). Composite particle.

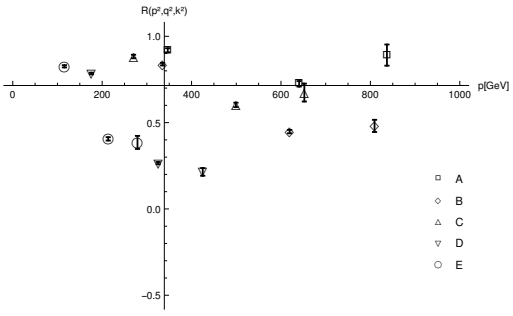

FIGURE D.48: Plot of the ratio for the improvement (5.8) for all sets of parameters and lattice size $L = 8$. Equal momentum configuration (2.20). Composite particle.

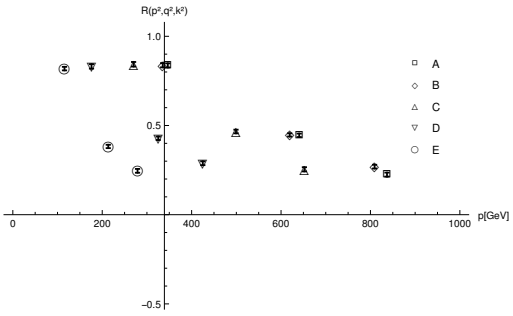

FIGURE D.49: Plot of the ratio for all sets of parameters and lattice size $L = 8$. Transverse-only configuration (2.21). Composite particle.

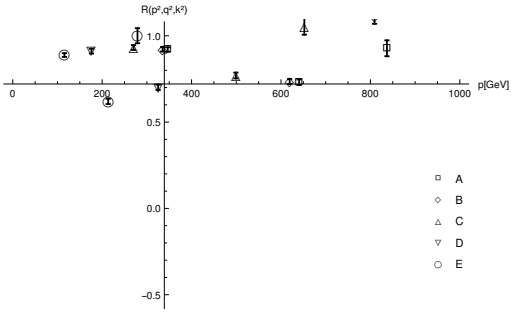

FIGURE D.50: Plot of the ratio for the improvement (5.7) for all sets of parameters and lattice size $L = 8$. Transverse-only configuration (2.21). Composite particle.

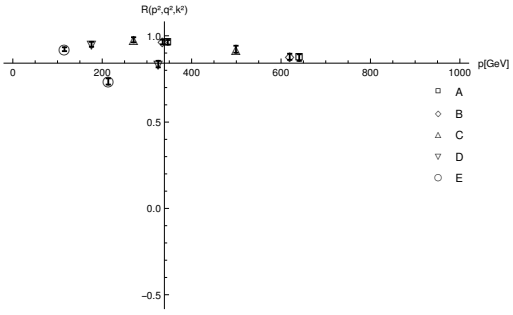

FIGURE D.51: Plot of the ratio for the improvement (5.8) for all sets of parameters and lattice size $L = 8$. Transverse-only configuration (2.21). Composite particle.

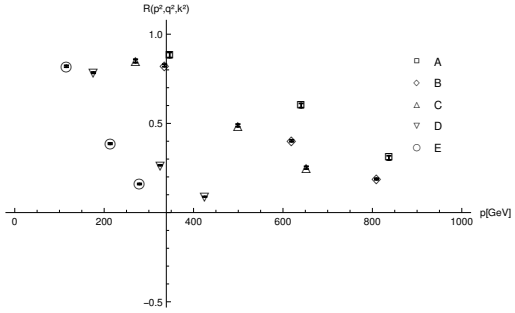

FIGURE D.52: Plot of the ratiofor all sets of parameters and lattice size $L = 8$. One momentum vanishing (2.22). Composite particle.

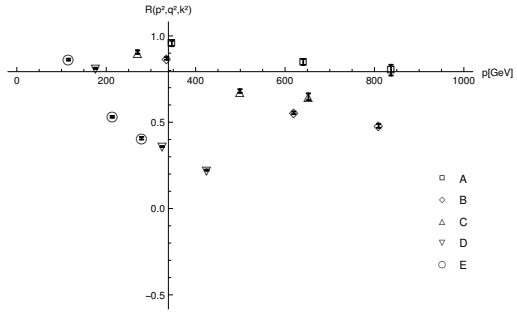

FIGURE D.53: Plot of the ratio for the improvement (5.5) for all sets of parameters and lattice size $L = 8$. One momentum vanishing (2.22). Composite particle.

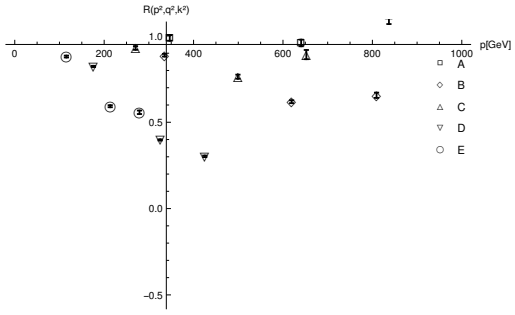

FIGURE D.54: Plot of the ratio for the improvement (5.6) for all sets of parameters and lattice size $L = 8$. One momentum vanishing (2.22). Composite particle.

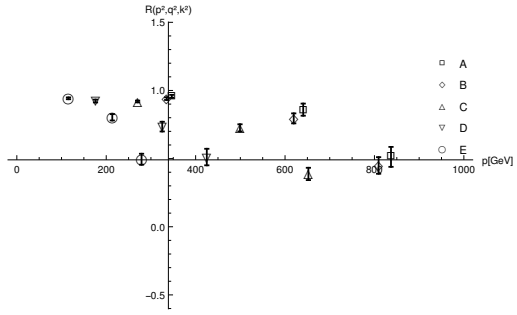

FIGURE D.55: Plot of the ratio for all sets of parameters and lattice size $L = 8$. Equal momentum configuration (2.20). Elementary particle.

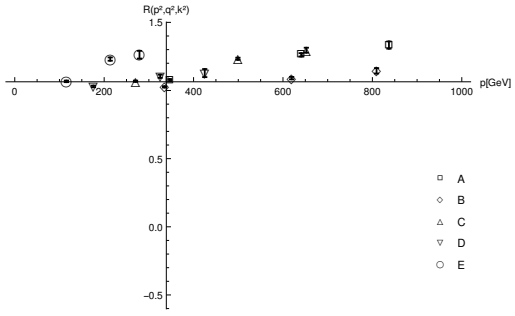

FIGURE D.56: Plot of the ratio for all sets of parameters and lattice size $L = 8$. One momentum vanishing (2.22). Elementary particle.

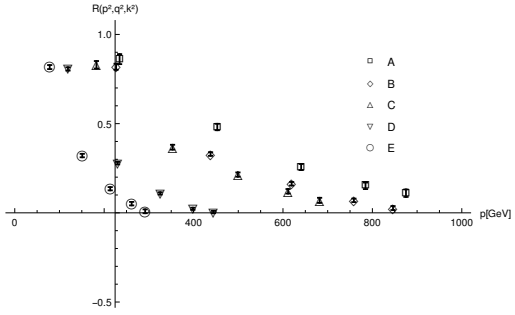

FIGURE D.57: Plot of the ratio for all sets of parameters and lattice size $L = 12$. Equal momentum configuration (2.20). Composite particle.

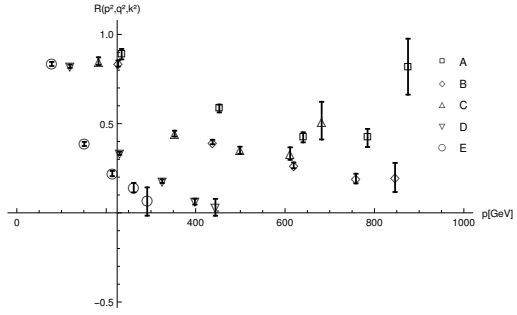

FIGURE D.58: Plot of the ratio for the improvement (5.7) for all sets of parameters and lattice size $L = 12$. Equal momentum configuration (2.20). Composite particle.

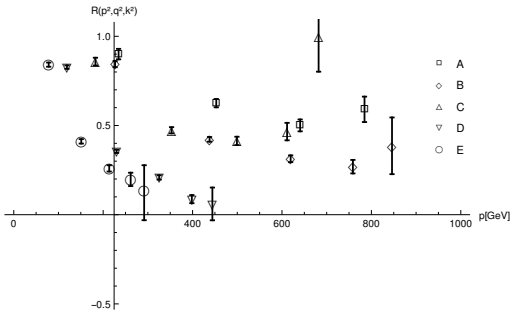

FIGURE D.59: Plot of the ratio for the improvement (5.8) for all sets of parameters and lattice size $L = 12$. Equal momentum configuration (2.20). Composite particle.

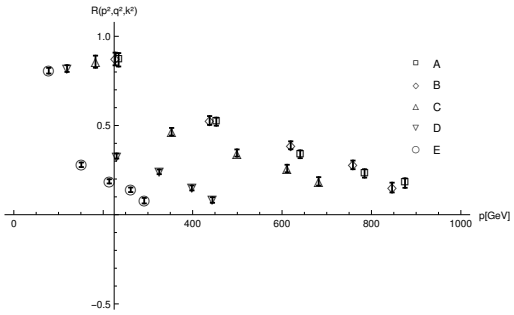

FIGURE D.60: Plot of the ratio for all sets of parameters and lattice size $L = 12$. Transverse-only configuration (2.21). Composite particle.

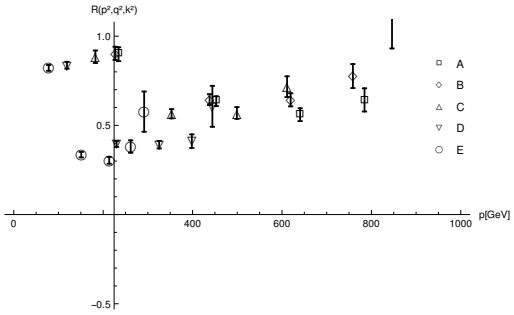

FIGURE D.61: Plot of the ratio for the improvement (5.7) for all sets of parameters and lattice size $L = 12$. Transverse-only configuration (2.21). Composite particle.

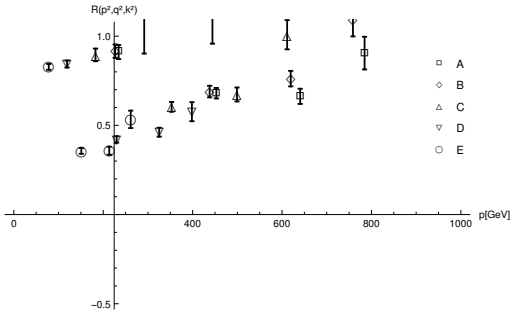

FIGURE D.62: Plot of the ratio for the improvement (5.8) for all sets of parameters and lattice size $L = 12$. Transverse-only configuration (2.21). Composite particle.

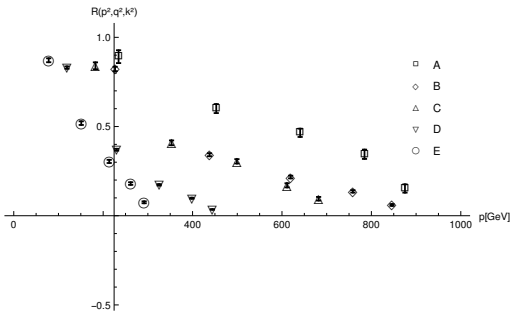

FIGURE D.63: Plot of the ratiofor all sets of parameters and lattice size $L = 12$. One momentum vanishing (2.22). Composite particle.

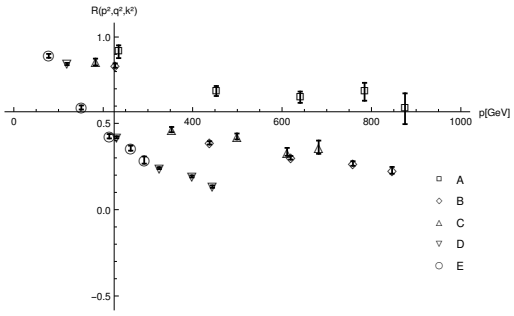

FIGURE D.64: Plot of the ratio for the improvement (5.5) for all sets of parameters and lattice size $L = 12$. One momentum vanishing (2.22). Composite particle.

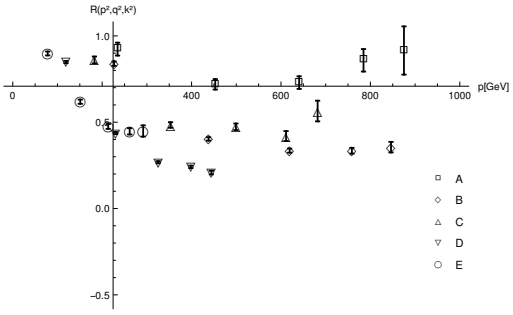

FIGURE D.65: Plot of the ratio for the improvement (5.6) for all sets of parameters and lattice size $L = 12$. One momentum vanishing (2.22). Composite particle.

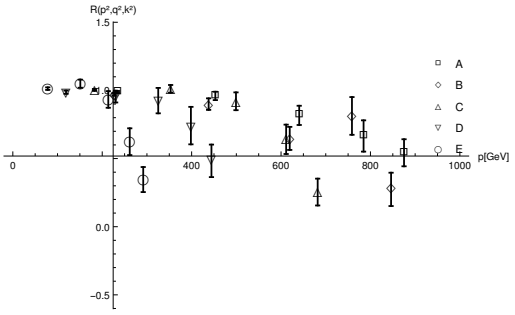

FIGURE D.66: Plot of the ratio for all sets of parameters and lattice size $L = 12$. Equal momentum configuration (2.20). Elementary particle.

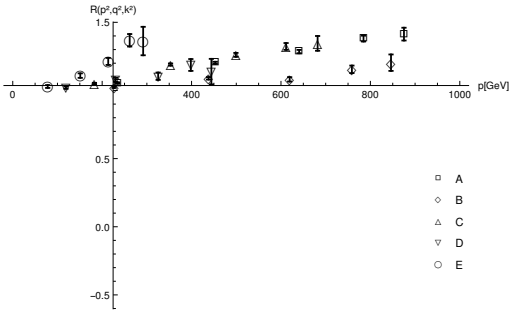

FIGURE D.67: Plot of the ratio for all sets of parameters and lattice size $L = 12$. One momentum vanishing (2.22). Elementary particle.

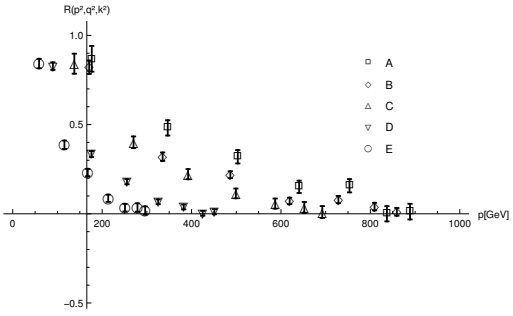

FIGURE D.68: Plot of the ratio for all sets of parameters and lattice size $L = 16$. Equal momentum configuration (2.20). Composite particle.

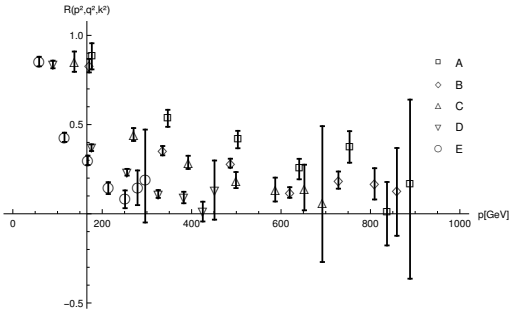

FIGURE D.69: Plot of the ratio for the improvement (5.7) for all sets of parameters and lattice size $L = 16$. Equal momentum configuration (2.20). Composite particle.

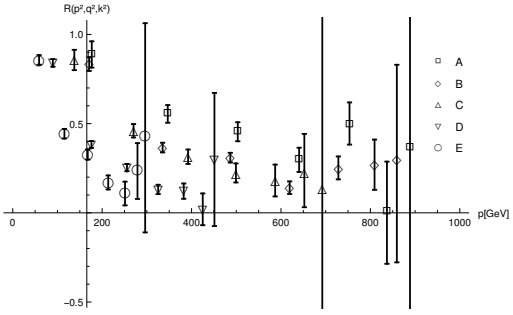

FIGURE D.70: Plot of the ratio for the improvement (5.8) for all sets of parameters and lattice size $L = 16$. Equal momentum configuration (2.20). Composite particle.

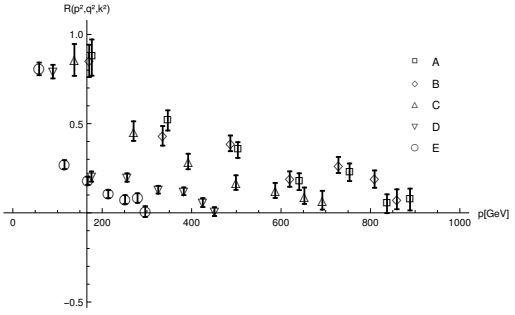

FIGURE D.71: Plot of the ratio for all sets of parameters and lattice size $L = 16$. Transverse-only configuration (2.21). Composite particle.

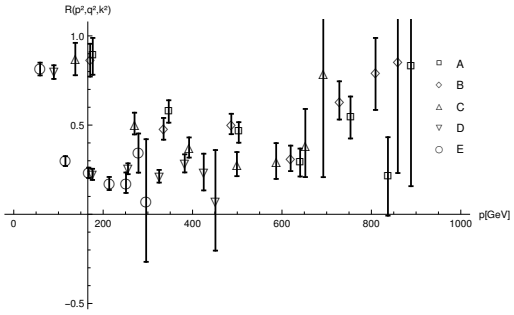

FIGURE D.72: Plot of the ratio for the improvement (5.7) for all sets of parameters and lattice size $L = 16$. Transverse-only configuration (2.21). Composite particle.

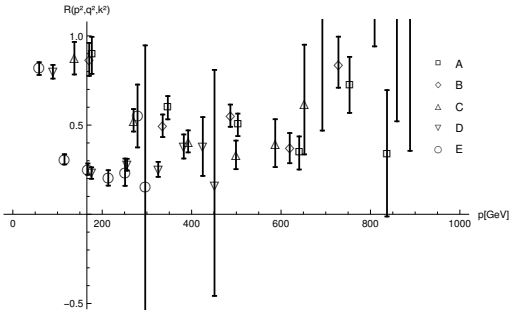

FIGURE D.73: Plot of the ratio for the improvement (5.8) for all sets of parameters and lattice size $L = 16$. Transverse-only configuration (2.21). Composite particle.

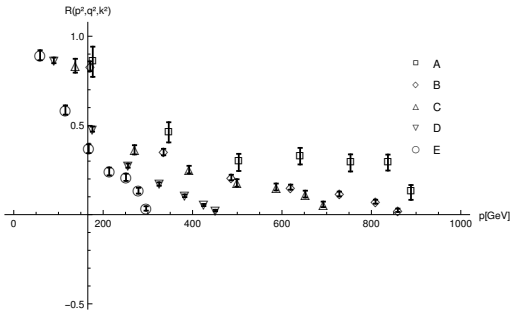

FIGURE D.74: Plot of the ratiofor all sets of parameters and lattice size $L = 16$. One momentum vanishing (2.22). Composite particle.

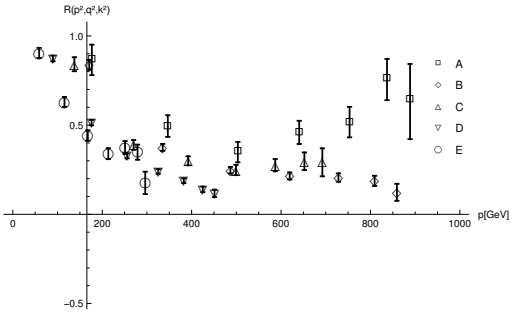

FIGURE D.75: Plot of the ratio for the improvement (5.5) for all sets of parameters and lattice size $L = 16$. One momentum vanishing (2.22). Composite particle.

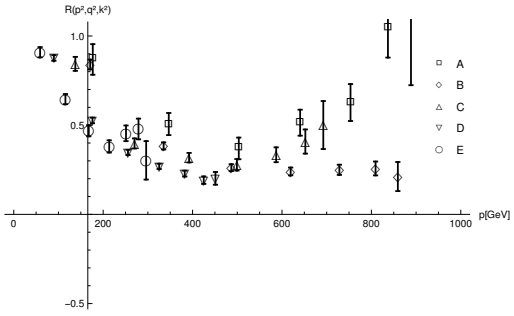

FIGURE D.76: Plot of the ratio for the improvement (5.6) for all sets of parameters and lattice size $L = 16$. One momentum vanishing (2.22). Composite particle.

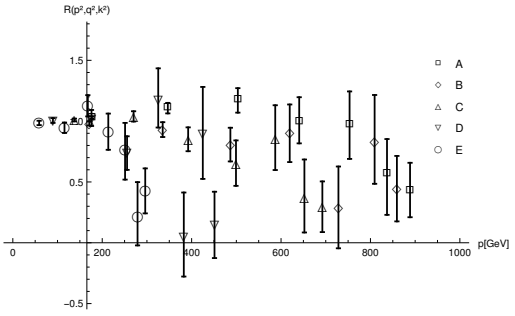

FIGURE D.77: Plot of the ratio for all sets of parameters and lattice size $L = 16$. Equal momentum configuration (2.20). Elementary particle.

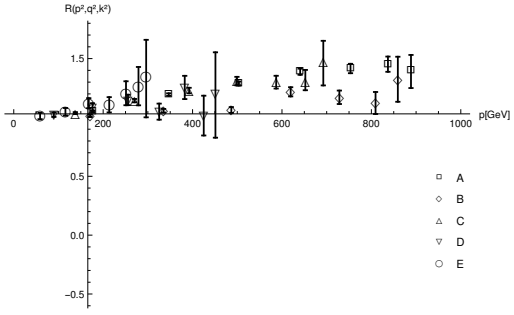

FIGURE D.78: Plot of the ratio for all sets of parameters and lattice size $L = 16$. One momentum vanishing (2.22). Elementary particle.

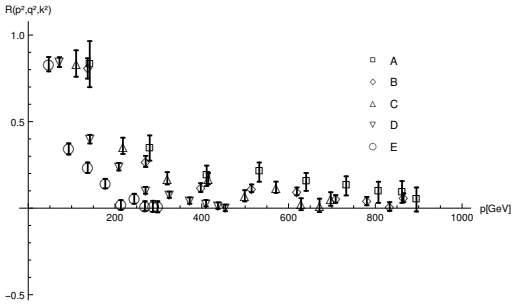

FIGURE D.79: Plot of the ratio for all sets of parameters and lattice size $L = 20$. Equal momentum configuration (2.20). Composite particle.

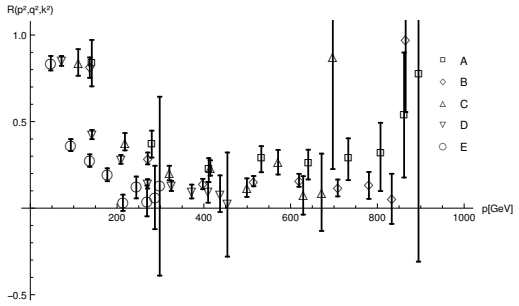

FIGURE D.80: Plot of the ratio for the improvement (5.7) for all sets of parameters and lattice size $L = 20$. Equal momentum configuration (2.20). Composite particle.

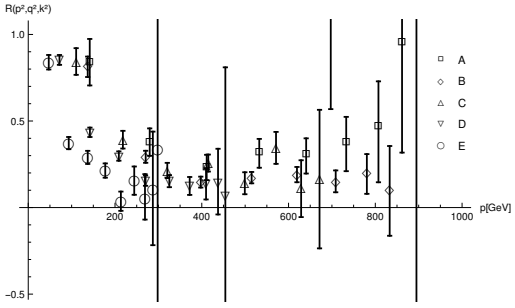

FIGURE D.81: Plot of the ratio for the improvement (5.8) for all sets of parameters and lattice size $L = 20$. Equal momentum configuration (2.20). Composite particle.

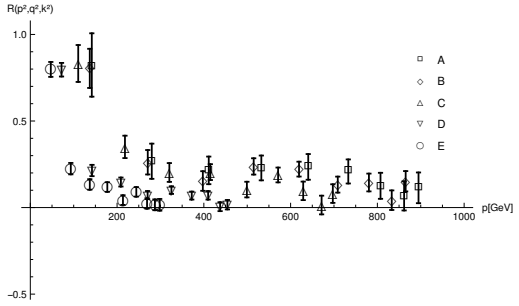

FIGURE D.82: Plot of the ratio for all sets of parameters and lattice size $L = 20$. Transverse-only configuration (2.21). Composite particle.

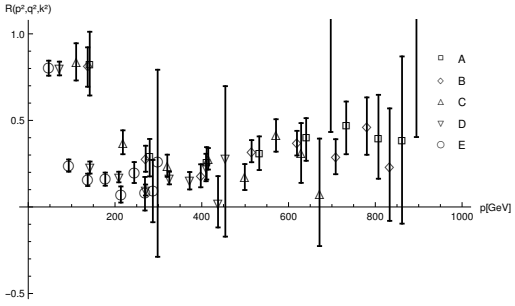

FIGURE D.83: Plot of the ratio for the improvement (5.7) for all sets of parameters and lattice size $L = 20$. Transverse-only configuration (2.21). Composite particle.

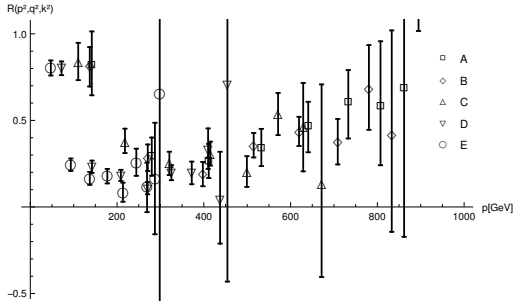

FIGURE D.84: Plot of the ratio for the improvement (5.8) for all sets of parameters and lattice size $L = 20$. Transverse-only configuration (2.21). Composite particle.

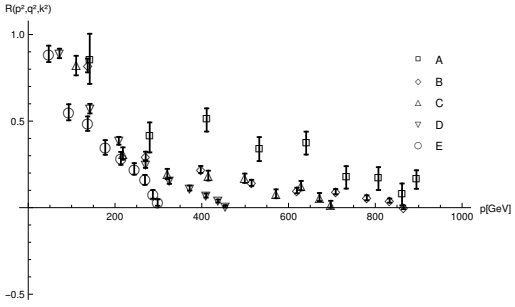

FIGURE D.85: Plot of the ratiofor all sets of parameters and lattice size $L = 20$. One momentum vanishing (2.22). Composite particle.

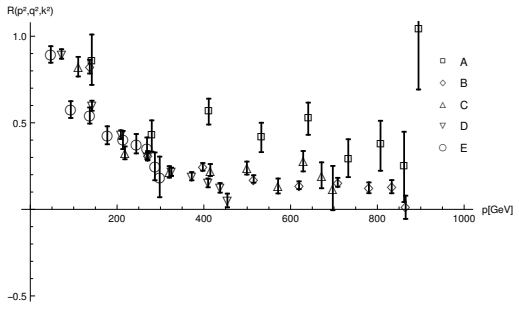

FIGURE D.86: Plot of the ratio for the improvement (5.5) for all sets of parameters and lattice size $L = 20$. One momentum vanishing (2.22). Composite particle.

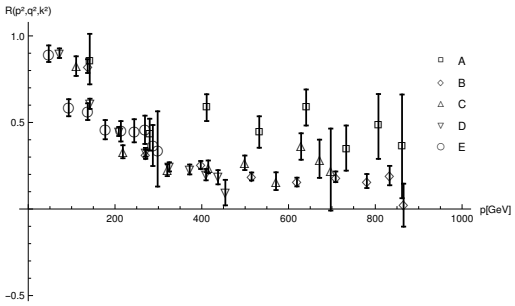

FIGURE D.87: Plot of the ratio for the improvement (5.6) for all sets of parameters and lattice size $L = 20$. One momentum vanishing (2.22). Composite particle.

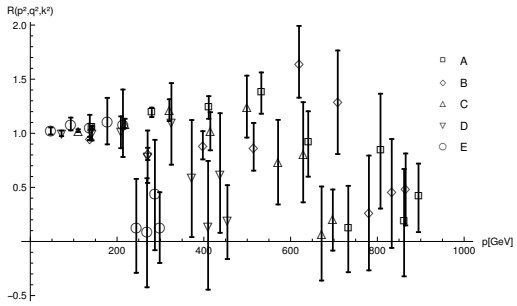

FIGURE D.88: Plot of the ratio for all sets of parameters and lattice size $L = 20$. Equal momentum configuration (2.20). Elementary particle.

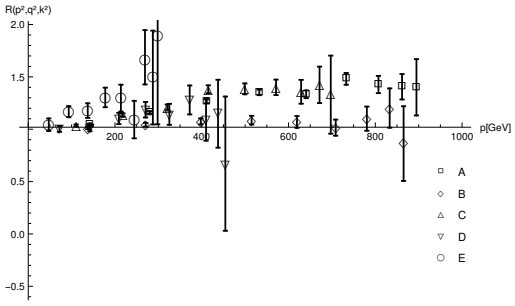

FIGURE D.89: Plot of the ratio for all sets of parameters and lattice size $L = 20$. One momentum vanishing (2.22). Elementary particle.

D.4 Plots for a fixed set of parameters

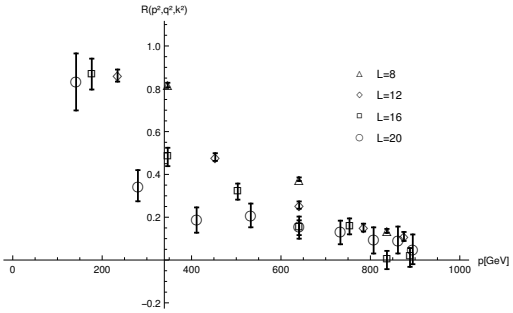

FIGURE D.90: Plot of the ratio for parameter set A and all lattice sizes. Equal momentum configuration (2.20). Composite particle.

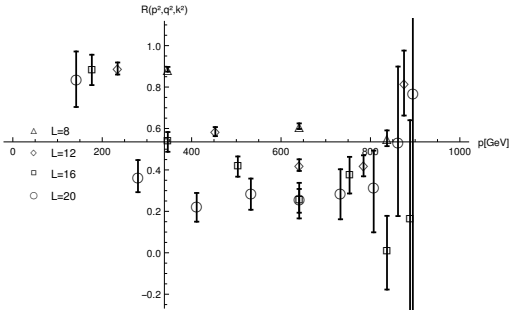

FIGURE D.91: Plot of the ratio for parameter set A and all lattice sizeswith improvement (5.7). Equal momentum configuration (2.20). Composite particle.

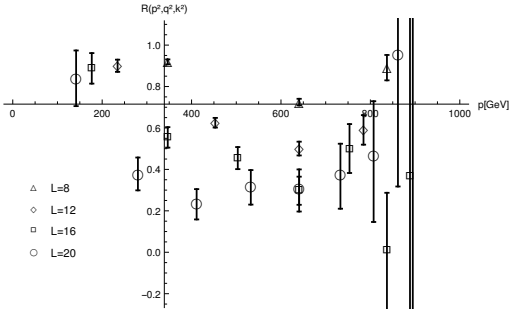

FIGURE D.92: Plot of the ratio for parameter set A and all lattice sizes with improvement (5.8). Equal momentum configuration (2.20). Composite particle.

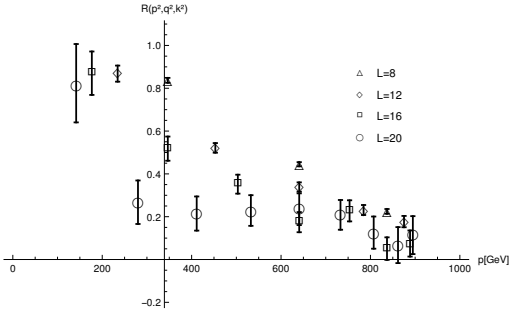

FIGURE D.93: Plot of the ratio for parameter set A and all lattice sizes. Transverse-only configuration (2.21). Composite particle.

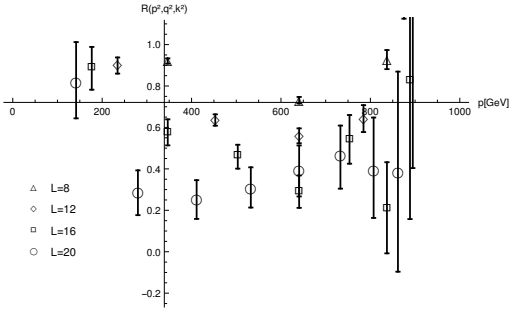

FIGURE D.94: Plot of the ratio for parameter set A and all lattice sizes with improvement (5.7). Transverse-only configuration (2.21). Composite particle.

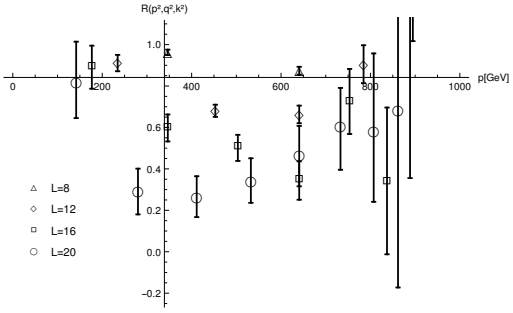

FIGURE D.95: Plot of the ratio for parameter set A and all lattice sizes with improvement (5.8). Transverse-only configuration (2.21). Composite particle.

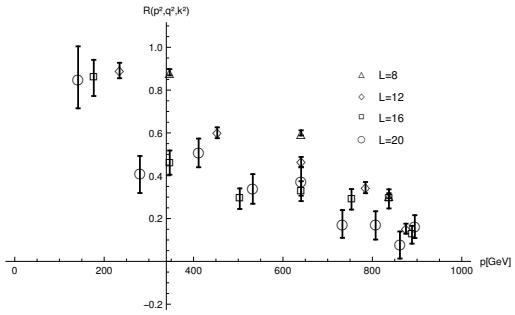

FIGURE D.96: Plot of the ratio for parameter set A and all lattice sizes. One momentum vanishing (2.22). Composite particle.

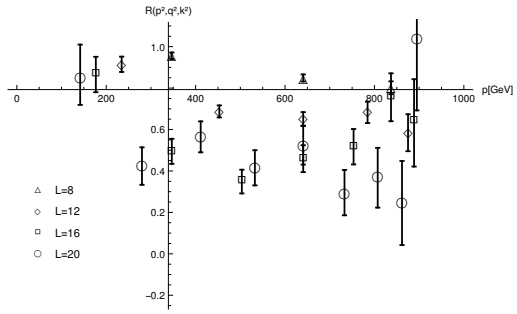

FIGURE D.97: Plot of the ratio for parameter set A and all lattice sizes with improvement (5.5). One momentum vanishing (2.22). Composite particle.

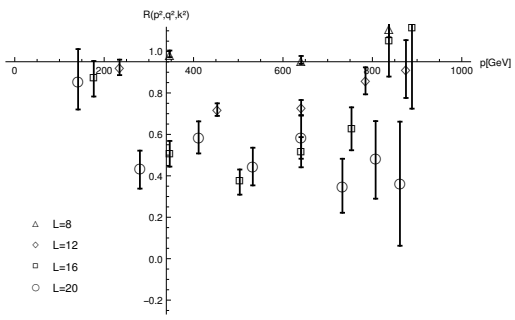

FIGURE D.98: Plot of the ratio for parameter set A and all lattice sizes with improvement (5.6). One momentum vanishing (2.22). Composite particle.

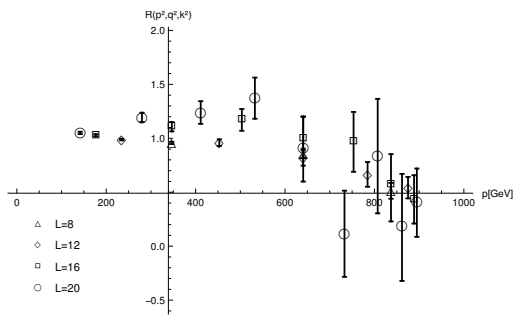

FIGURE D.99: Plot of the ratio for parameter set A and all lattice sizes. Equal momentum configuration (2.21). Elementary fields.

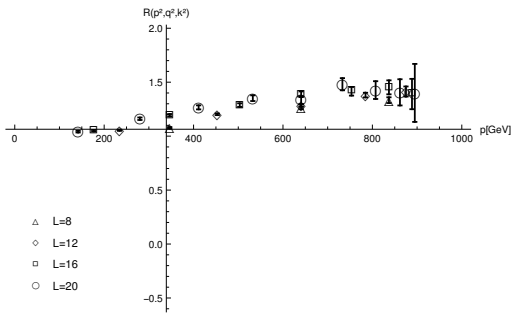

FIGURE D.100: Plot of the ratio for parameter set A and all lattice sizes with improvement. One momentum vanishing (2.22). Elementary fields.

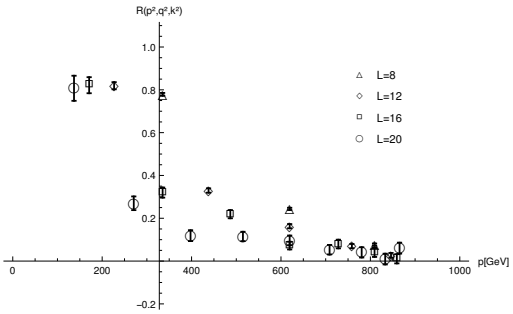

FIGURE D.101: Plot of the ratio for parameter set B and all lattice sizes. Equal momentum configuration (2.20). Composite particle.

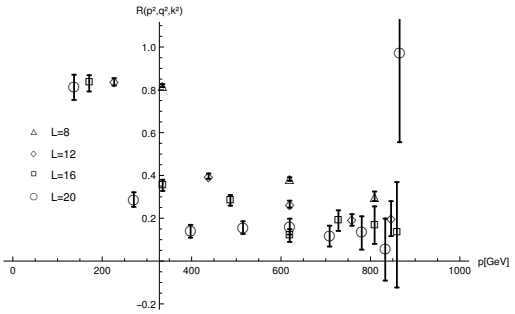

FIGURE D.102: Plot of the ratio for parameter set B and all lattice sizeswith improvement (5.7). Equal momentum configuration (2.20). Composite particle.

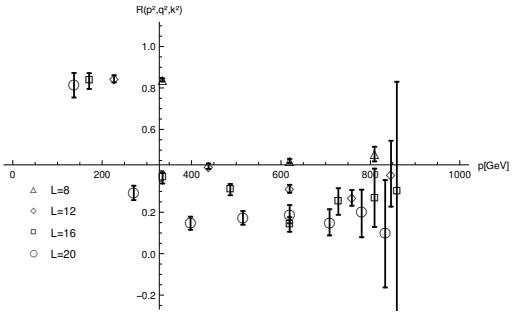

FIGURE D.103: Plot of the ratio for parameter set B and all lattice sizes with improvement (5.8). Equal momentum configuration (2.20). Composite particle.

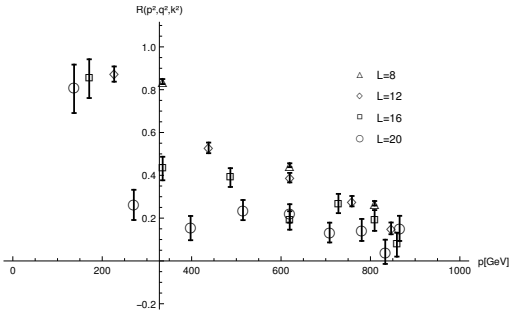

FIGURE D.104: Plot of the ratio for parameter set B and all lattice sizes. Transverse-only configuration (2.21). Composite particle.

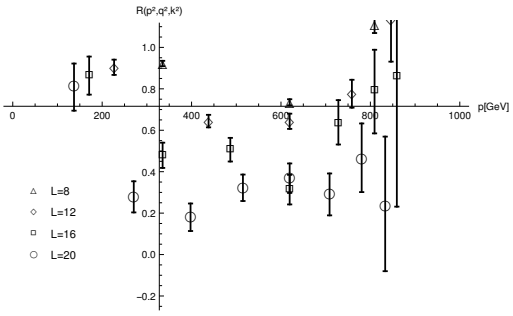

FIGURE D.105: Plot of the ratio for parameter set B and all lattice sizes with improvement (5.7). Transverse-only configuration (2.21). Composite particle.

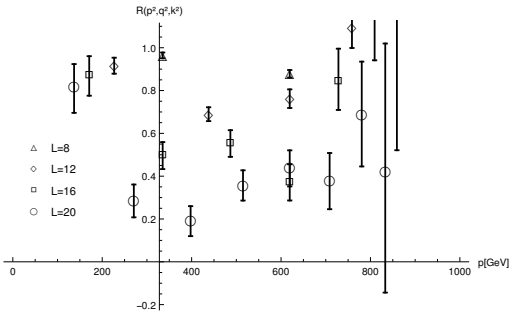

FIGURE D.106: Plot of the ratio for parameter set B and all lattice sizes with improvement (5.8). Transverse-only configuration (2.21). Composite particle.

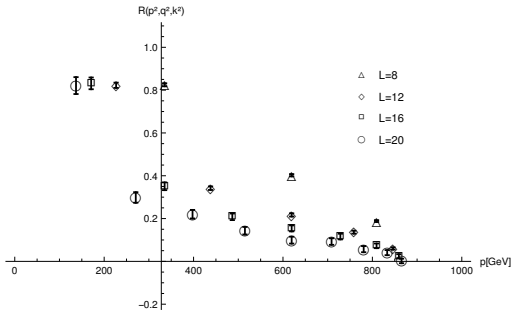

FIGURE D.107: Plot of the ratio for parameter set B and all lattice sizes. One momentum vanishing (2.22). Composite particle.

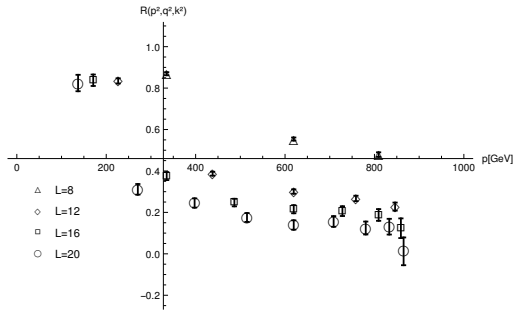

FIGURE D.108: Plot of the ratio for parameter set B and all lattice sizes with improvement (5.5). One momentum vanishing (2.22). Composite particle.

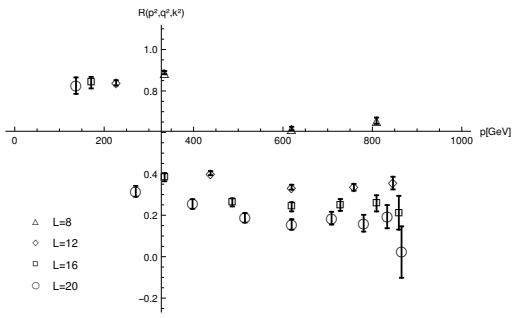

FIGURE D.109: Plot of the ratio for parameter set B and all lattice sizes with improvement (5.6). One momentum vanishing (2.22). Composite particle.

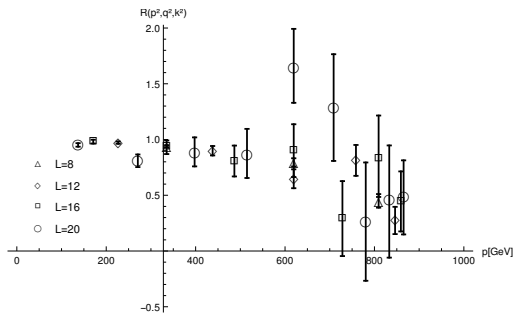

FIGURE D.110: Plot of the ratio for parameter set B and all lattice sizes. Equal momentum configuration (2.21). Elementary fields.

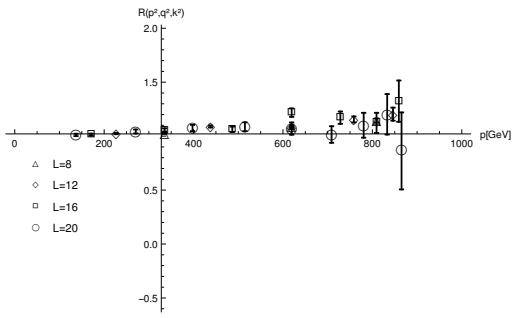

FIGURE D.111: Plot of the ratio for parameter set B and all lattice sizes with improvement. One momentum vanishing (2.22). Elementary fields.

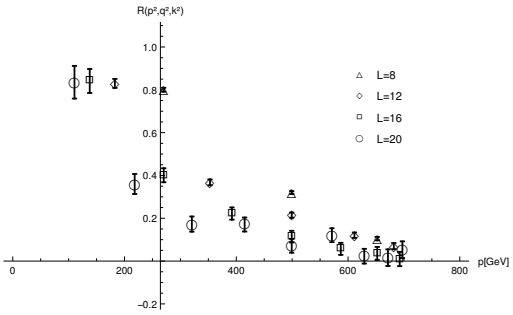

FIGURE D.112: Plot of the ratio for parameter set C and all lattice sizes. Equal momentum configuration (2.20). Composite particle.

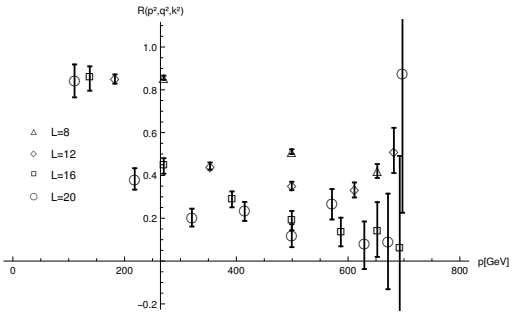

FIGURE D.113: Plot of the ratio for parameter set C and all lattice sizeswith improvement (5.7). Equal momentum configuration (2.20). Composite particle.

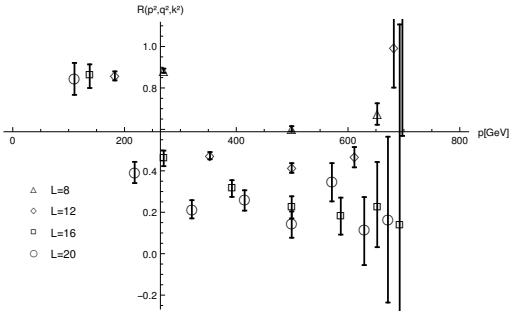

FIGURE D.114: Plot of the ratio for parameter set C and all lattice sizes with improvement (5.8). Equal momentum configuration (2.20). Composite particle.

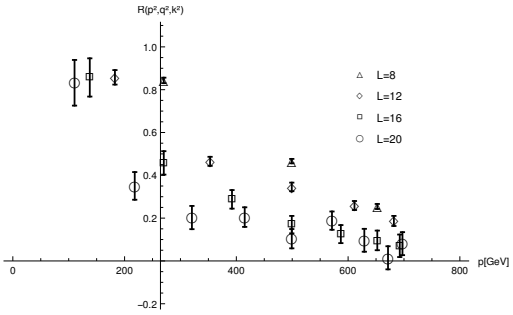

FIGURE D.115: Plot of the ratio for parameter set C and all lattice sizes. Transverse-only configuration (2.21). Composite particle.

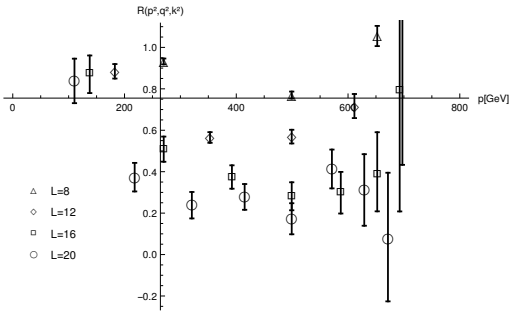

FIGURE D.116: Plot of the ratio for parameter set C and all lattice sizes with improvement (5.7). Transverse-only configuration (2.21). Composite particle.

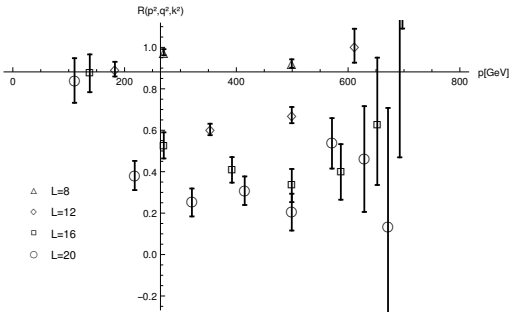

FIGURE D.117: Plot of the ratio for parameter set C and all lattice sizes with improvement (5.8). Transverse-only configuration (2.21). Composite particle.

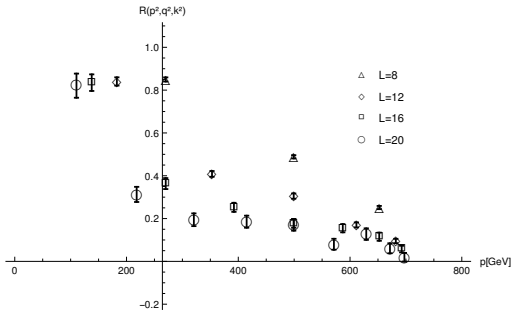

FIGURE D.118: Plot of the ratio for parameter set C and all lattice sizes. One momentum vanishing (2.22). Composite particle.

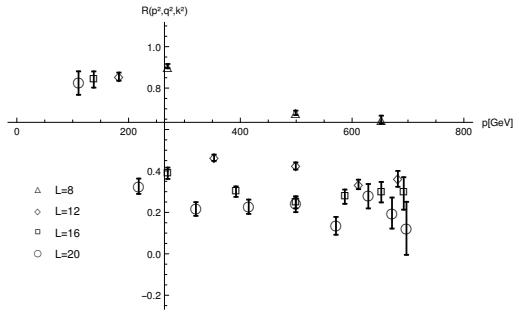

FIGURE D.119: Plot of the ratio for parameter set C and all lattice sizes with improvement (5.5). One momentum vanishing (2.22). Composite particle.

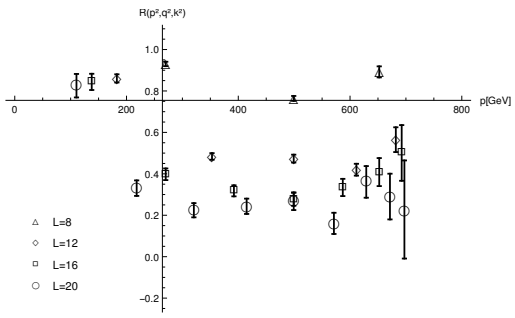

FIGURE D.120: Plot of the ratio for parameter set C and all lattice sizes with improvement (5.6). One momentum vanishing (2.22). Composite particle.

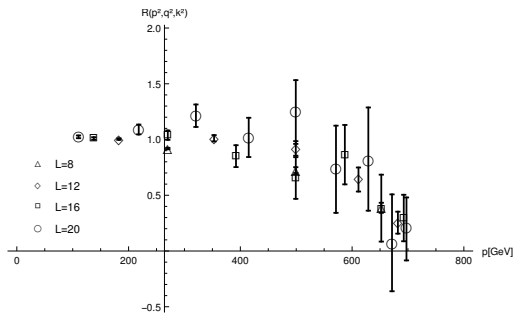

FIGURE D.121: Plot of the ratio for parameter set C and all lattice sizes. Equal momentum configuration (2.21). Elementary fields.

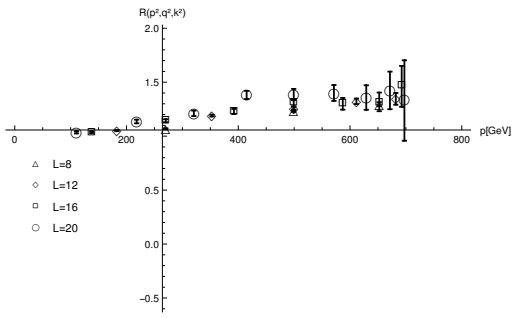

FIGURE D.122: Plot of the ratio for parameter set C and all lattice sizes with improvement. One momentum vanishing (2.22). Elementary fields.

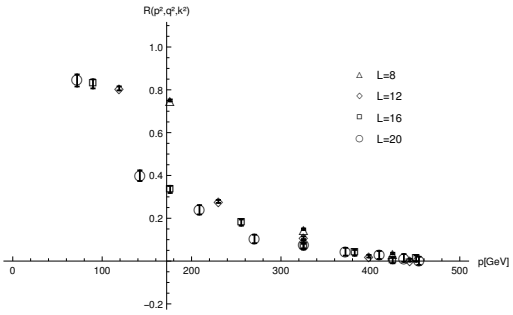

FIGURE D.123: Plot of the ratio for parameter set D and all lattice sizes. Equal momentum configuration (2.20). Composite particle.

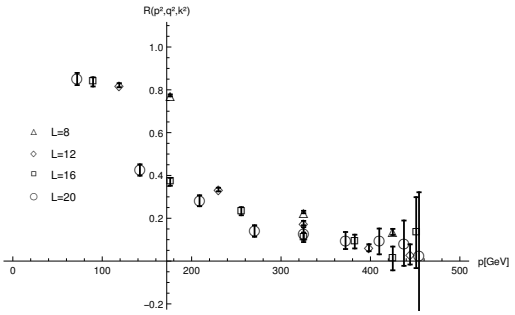

FIGURE D.124: Plot of the ratio for parameter set D and all lattice sizeswith improvement (5.7). Equal momentum configuration (2.20). Composite particle.

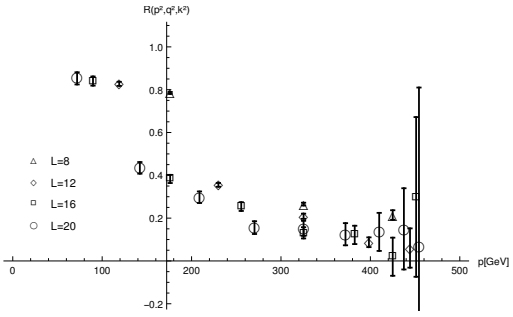

FIGURE D.125: Plot of the ratio for parameter set D and all lattice sizes with improvement (5.8). Equal momentum configuration (2.20). Composite particle.

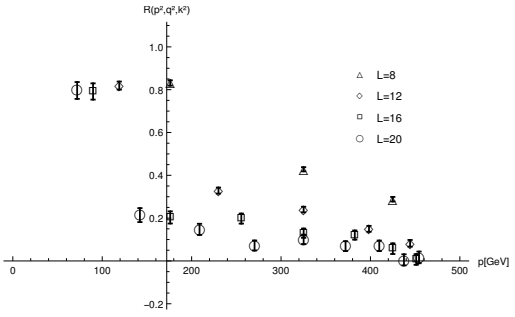

FIGURE D.126: Plot of the ratio for parameter set D and all lattice sizes. Transverse-only configuration (2.21). Composite particle.

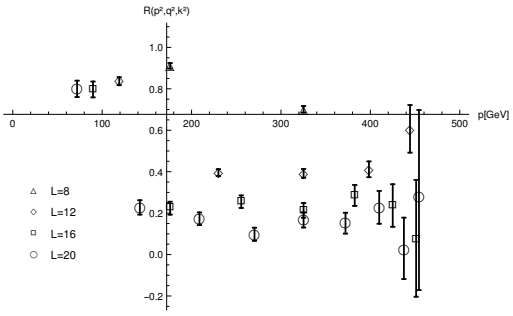

FIGURE D.127: Plot of the ratio for parameter set D and all lattice sizes with improvement (5.7). Transverse-only configuration (2.21). Composite particle.

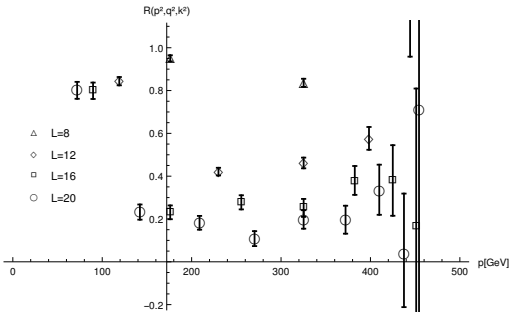

FIGURE D.128: Plot of the ratio for parameter set D and all lattice sizes with improvement (5.8). Transverse-only configuration (2.21). Composite particle.

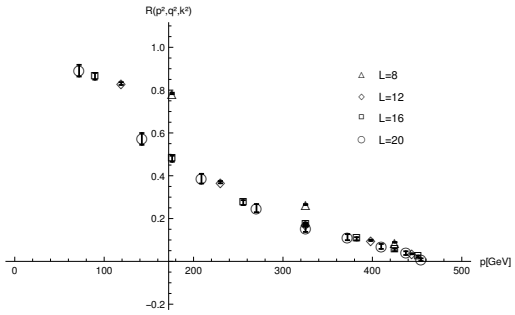

FIGURE D.129: Plot of the ratio for parameter set D and all lattice sizes. One momentum vanishing (2.22). Composite particle.

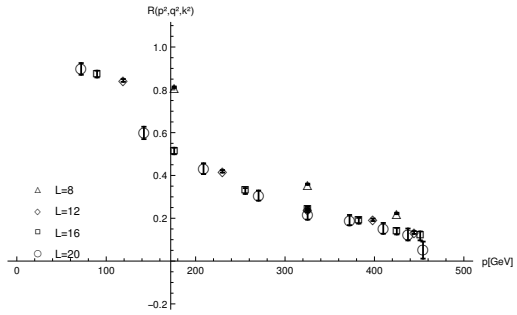

FIGURE D.130: Plot of the ratio for parameter set D and all lattice sizes with improvement (5.5). One momentum vanishing (2.22). Composite particle.

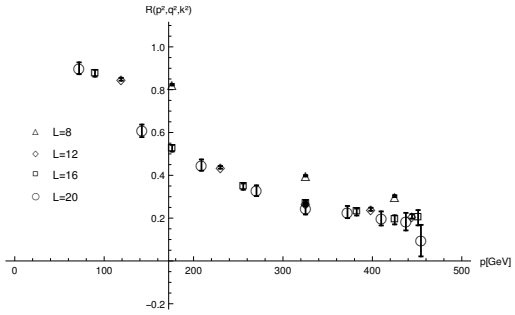

FIGURE D.131: Plot of the ratio for parameter set D and all lattice sizes with improvement (5.6). One momentum vanishing (2.22). Composite particle.

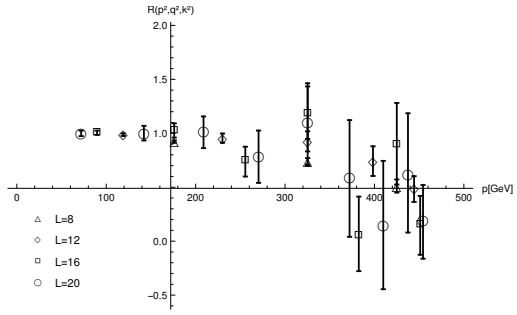

FIGURE D.132: Plot of the ratio for parameter set D and all lattice sizes. Equal momentum configuration (2.21). Elementary fields.

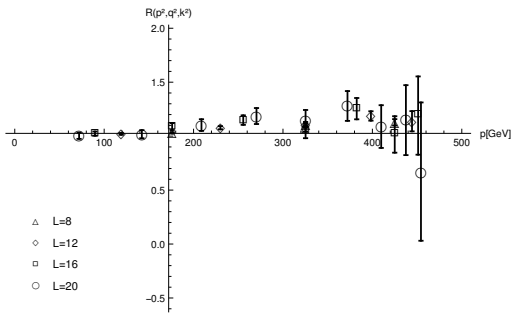

FIGURE D.133: Plot of the ratio for parameter set D and all lattice sizes with improvement. One momentum vanishing (2.22). Elementary fields.

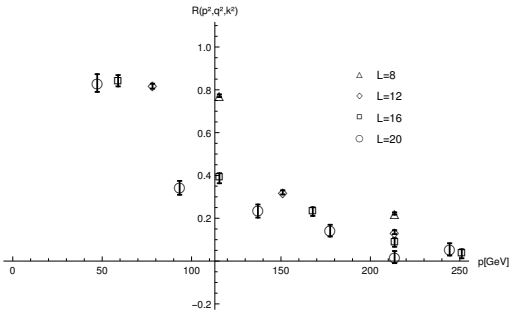

FIGURE D.134: Plot of the ratio for parameter set E and all lattice sizes. Equal momentum configuration (2.20). Composite particle.

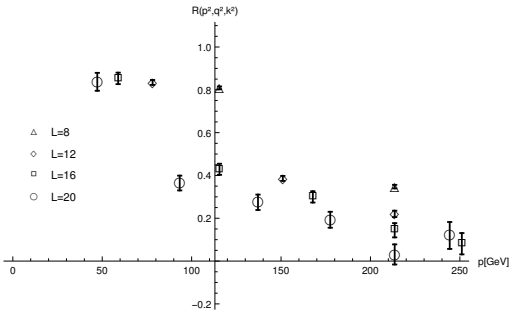

FIGURE D.135: Plot of the ratio for parameter set E and all lattice sizeswith improvement (5.7). Equal momentum configuration (2.20). Composite particle.

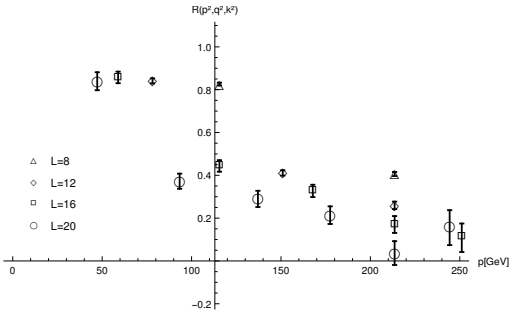

FIGURE D.136: Plot of the ratio for parameter set E and all lattice sizes with improvement (5.8). Equal momentum configuration (2.20). Composite particle.

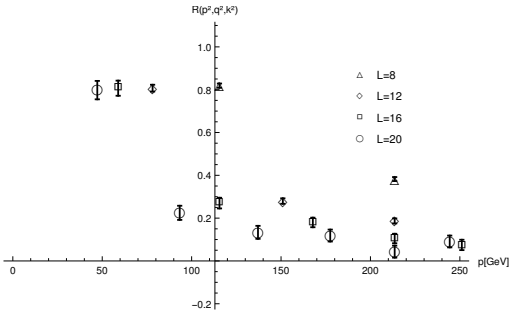

FIGURE D.137: Plot of the ratio for parameter set E and all lattice sizes. Transverse-only configuration (2.21). Composite particle.

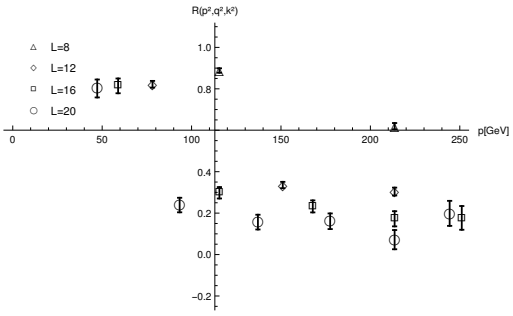

FIGURE D.138: Plot of the ratio for parameter set E and all lattice sizes with improvement (5.7). Transverse-only configuration (2.21). Composite particle.

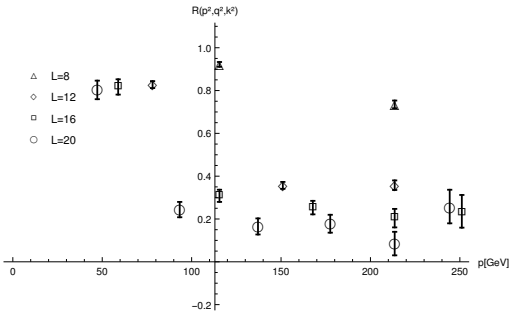

FIGURE D.139: Plot of the ratio for parameter set E and all lattice sizes with improvement (5.8). Transverse-only configuration (2.21). Composite particle.

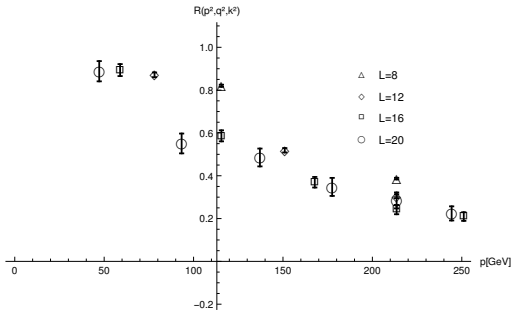

FIGURE D.140: Plot of the ratio for parameter set E and all lattice sizes. One momentum vanishing (2.22). Composite particle.

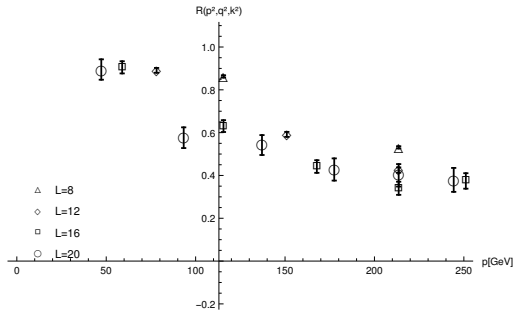

FIGURE D.141: Plot of the ratio for parameter set E and all lattice sizes with improvement (5.5). One momentum vanishing (2.22). Composite particle.

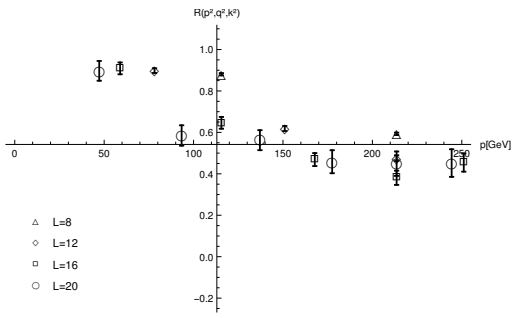

FIGURE D.142: Plot of the ratio for parameter set E and all lattice sizes with improvement (5.6). One momentum vanishing (2.22). Composite particle.

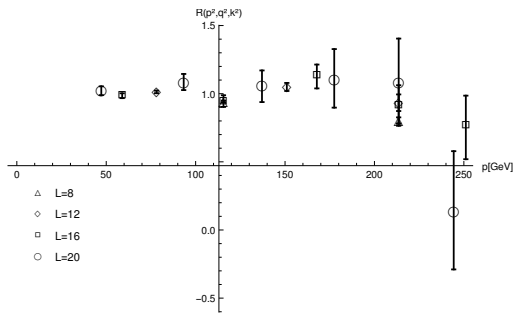

FIGURE D.143: Plot of the ratio for parameter set E and all lattice sizes. Equal momentum configuration (2.21). Elementary fields.

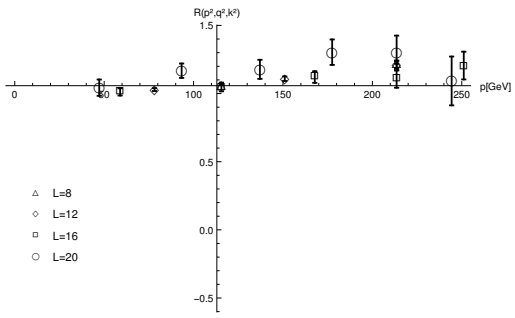

FIGURE D.144: Plot of the ratio for parameter set E and all lattice sizes with improvement. One momentum vanishing (2.22). Elementary fields.

Appendix E

Radii tables

TABLE E.1: Table containing the radii for all lattice sizes and all sets of parameters for the equal momentum configuration (2.20), with improvement 5.7. Composite particle

Lattice Size	A value [fm]	A Errors[fm]	B value[fm]	B Errors[fm]	C value[fm]	C Errors[fm]	D value[fm]	D Errors[fm]	E value[fm]	E Errors[fm]
8	0.0023	+0.0001/-0.0001	0.00311	+0.00005/-0.00005	0.0034	+0.00001/-0.00001	0.00661	+0.00006/-0.00006	0.0093	+0.0002/-0.0001
12	0.0034	+0.0003/-0.0003	0.0043	+0.0001/-0.0002	0.0052	-0.0002/-0.0002	0.0087	+0.0002/-0.0002	0.0127	+0.0003/-0.0003
16	0.0048	+0.0009/-0.0008	0.0059	+0.0004/-0.0004	0.0068	+0.0007/-0.0008	0.011	+0.0005/-0.0005	0.016	+0.001/-0.0009
20	0.007	+0.002/-0.002	0.0076	+0.0006/-0.0007	+0.009	+0.001/-0.001	0.013	+0.0008/-0.0009	0.021	+0.002/-0.002

TABLE E.2: Table containing the radii for all lattice sizes and all sets of parameters for the equal momentum configuration (2.20), with improvement 5.8. Composite particle

Lattice Size	A value [fm]	A Errors[fm]	B value[fm]	B Errors[fm]	C value[fm]	C Errors[fm]	D value[fm]	D Errors[fm]	E value[fm]	E Errors[fm]
8	0.001	+0.0001/-0.0001	0.00294	+0.00006/-0.00006	0.0031	+0.0001/-0.0001	0.00645	+0.00007/-0.00007	0.0088	+0.0002/-0.0002
12	0.0033	+0.0003/-0.0003	0.0043	+0.0001/-0.0002	0.005	-0.0002/-0.0003	0.0086	+0.0002/-0.0002	0.0124	+0.0003/-0.0004
16	0.0047	+0.0009/-0.0008	0.0058	+0.0004/-0.0004	0.0067	+0.0008/-0.0008	0.0109	+0.0005/-0.0005	0.016	+0.001/-0.001
20	0.006	+0.001/-0.002	0.0076	+0.0006/-0.0007	0.009	+0.001/-0.001	0.0129	+0.0008/-0.0009	0.021	+0.002/-0.002

TABLE E.3: Table containing the radii for all lattice sizes and all sets of parameters for the transverse-only momentum configuration (2.21), with improvement 5.7. Composite particle

Lattice Size	A value [fm]	A Errors[fm]	B value[fm]	B Errors[fm]	C value[fm]	C Errors[fm]	D value[fm]	D Errors[fm]	E value[fm]	E Errors[fm]
8	0.0019	+0.0001/-0.0002	0.002	+0.0001/-0.0002	0.0024	+0.0002/-0.0002	0.0041	+0.0003/-0.0003	0.0071	+0.0003/-0.0003
12	0.0032	+0.0004/-0.0004	0.0033	+0.0004/-0.0004	0.0046	-0.0004/-0.0004	0.0082	+0.0003/-0.0003	0.0132	+0.0004/-0.0004
16	0.005	+0.001/-0.001	0.005	+0.001/-0.001	0.006	+0.001/-0.001	0.0123	+0.0007/-0.0007	0.017	+0.001/-0.001
20	0.007	+0.002/-0.002	0.008	+0.001/-0.001	0.009	+0.002/-0.002	0.015	+0.001/-0.001	0.023	+0.002/-0.002

TABLE E.4: Table containing the radii for all lattice sizes and all sets of parameters for the transverse-only momentum configuration (2.21), with improvement 5.8. Composite particle

Lattice Size	A value [fm]	A Errors[fm]	B value[fm]	B Errors[fm]	C value[fm]	C Errors[fm]	D value[fm]	D Errors[fm]	E value[fm]	E Errors[fm]
8	0.0014	+0.0002/-0.0003	0.0014	+0.0002/-0.0002	0.0014	+0.0004/-0.0004	0.003	+0.0004/-0.0005	0.0059	+0.0005/-0.0005
12	0.0031	+0.0004/-0.0005	0.0031	+0.0005/-0.0005	0.0043	-0.0005/-0.0005	0.0081	+0.0003/-0.0003	0.013	+0.0004/-0.0005
16	0.004	+0.001/-0.001	0.005	+0.001/-0.001	0.006	+0.001/-0.001	0.012	+0.0008/-0.0008	0.018	+0.001/-0.001
20	0.007	+0.002/-0.002	0.007	+0.001/-0.001	0.009	+0.002/-0.002	0.015	+0.001/-0.001	0.023	+0.002/-0.002

TABLE E.5: Table containing the radii for all lattice sizes and all sets of parameters for the configuration with one momentum vanishing (2.22), with improvement 5.5. Composite particle

Lattice Size	A value [fm]	A Errors[fm]	B value[fm]	B Errors[fm]	C value[fm]	C Errors[fm]	D value[fm]	D Errors[fm]	E value[fm]	E Errors[fm]
8	0.0015	+0.0002/-0.0002	0.00264	+0.00006/-0.00006	0.0027	+0.0001/-0.0001	0.00603	+0.00004/-0.00004	0.0079	+0.0001/-0.0001
12	0.003	+0.0004/-0.0004	0.0044	+0.0001/-0.0001	0.0051	-0.0002/-0.0002	0.0081	+0.0001/-0.0001	0.0104	+0.0004/-0.0004
16	0.005	+0.0009/-0.001	0.0058	+0.0003/-0.0003	0.0071	+0.0005/-0.0005	0.0097	+0.0004/-0.0004	0.013	+0.001/-0.001
20	0.007	+0.002/-0.002	0.0075	+0.0005/-0.0005	0.0092	+0.0008/-0.0008	0.011	+0.001/-0.001	0.017	+0.003/-0.002

TABLE E.6: Table containing the radii for all lattice sizes and all sets of parameters for the configuration with one momentum vanishing (2.22), with improvement 5.6. Composite particle

Lattice Size	A value [fm]	A Errors[fm]	B value[fm]	B Errors[fm]	C value[fm]	C Errors[fm]	D value[fm]	D Errors[fm]	E value[fm]	E Errors[fm]
8	0.0007	+0.0005/-0.0004	0.00244	+0.00007/-0.00007	0.0024	+0.0002/-0.0002	0.00584	+0.00004/-0.00005	0.0073	+0.0001/-0.0001
12	0.0029	+0.0005/-0.0005	0.0043	+0.0001/-0.0001	0.005	-0.0002/-0.0002	0.008	+0.0001/-0.0001	0.01	+0.0004/-0.0004
16	0.005	+0.001/-0.001	0.0057	+0.0003/-0.0003	0.007	+0.0005/-0.0005	0.0096	+0.0004/-0.0004	0.013	+0.001/-0.001
20	0.007	+0.002/-0.002	0.0075	+0.0005/-0.0005	0.0092	+0.0008/-0.0009	0.011	+0.001/-0.001	0.017	+0.003/-0.003

Bibliography

[1] Observation of a new particle in the search for the standard model higgs boson with the atlas detector at the lhc. *arXiv:*, 1207.7214 [hep-ex], 2012.

[2] C. Patrignani *et al.* Particle Data Group Collaboration. Review of particle physics. *Chin. Phys.*, C40 no.10, 2016.

[3] A.Gurtu M.W Grünewald. The mass and width of the w boson. *Particle Data Group*, 2017.

[4] G. Morchio J. Fröhlich and F. Strocchi. Higgs phenomenon without a symmetry breaking order parameter. *Phys.Lett.*, B87, 1980.

[5] G. Morchio J. Fröhlich and F. Strocchi. Higgs phenomenon without a symmetry breaking order parameter. *Nucl.Phys.*, B190, 1981.

[6] Pascal Törek. *The physical spectrum of theories with a Brout-Englert-Higgs effect.* 2018.

[7] A. Maas. Brout-englert-higgs physics: From foundations to phenomenology. *arXiv:*, 1712.04721 [hep-ph], 2017.

[8] Tajdar Mufti Axel Maas. A spectroscopical analysis of the phase diagram of yang-mills-higgs theory. *arXiv:*, 1412.6440 [hep-lat], 2014.

[9] Axel Maas Attilio Cucchieri and Tereza Mendes. Exploratory study of three-point green's functions in landau-gauge yang-mills theory. *arXiv:*, 0605.011 [hep-lat], 2006.

[10] W.S.C. Williams. *Nuclear and Particle Physics.* Clarendon Press, 1991.

[11] R. Alkofer M. Vujinovic G. Eichmann, R. Williams. The three-gluon vertex in landau gauge. *arXiv:*, 1402.1365 [hep-ph], 2014.

[12] H. J. Rothe. *Lattice gauge theories: An Introduction.* World Scientific Pub Co Inc., 2012.

[13] C.B. Lang C. Gattringer. *Quantum chromodynamics on the lattice: An Introductory Presentation.* Lect. Notes Phys., Springer, Berlin Heidelberg, 2010.

[14] Tajdar Mufti Axel Maas. Two- and three-point functions in landau gauge yang-mills-higgs theory. *arXiv:*, 1312.4873 [hep-lat], 2013.

[15] A. Maas. Accessing directly the properties of fundamental scalars in the confinement and higgs phase. *arXiv:*, 1007.0729 [hep-lat], 2010.

[16] Axel Maas. *Data from Axel Maas.* 2018.

[17] A. Maas. Gauge bosons at zero and finite temperature. *arXiv:*, 1106.3942 [hep-ph], 2013.

[18] Joos Böhm, Denner. *Gauge Theories of the Strong and Electroweak Interaction.* Teubner, 2001.